UNIVERSITY OF NAVARRA

TECHNOLOGICAL CAMPUS, TECNUN

DONOSTIA - SAN SEBASTIÁN

tecnun
Universidad
de Navarra

NEW MASS-BASED POPULATION BALANCE MODEL INCLUDING SHEAR RATE EFFECTS: APPLICATION TO STRUVITE RECOVERY

THESIS SUBMITTED
to obtain the doctor degree (PhD)
presented by

BEÑAT ELDUAYEN ECHAVE

under the supervision of

Paloma Grau Gumbau and
Gorka Sánchez Larraona

Donostia – San Sebastián, November 2020

Itxekuei

¿Para qué sirve la utopía?

La utopía está en el horizonte. Camino dos pasos, ella se aleja dos pasos. Camino diez pasos y el horizonte se corre diez pasos más allá.

¿Entonces, para qué sirve la utopía?

Para eso sirve, para caminar.

Fernando Birri

ACKNOWLEDGEMENTS

Parte de esta tesis se ha escrito durante el confinamiento provocado por el Covid-19. El bicho nos ha llevado a una situación inesperada e imprevisible a la que nos vamos adaptando como buenamente podemos. A pesar de lo duro de la situación, si algo nos ha podido enseñar el poner el mundo en pausa es a valorar lo que es realmente importante para cada uno de nosotros. De todo ello, me quedo sin duda con la gente que durante estos años me ha acompañado. Gente muy especial en mi caso y a la que me gustaría dedicar unas palabras de agradecimiento en las siguientes líneas, a algunos por sus aportaciones a la tesis y a todos por estar ahí cuando lo he necesitado.

En primer lugar, me gustaría agradecer a mi directora de tesis, Paloma Grau, la enorme confianza depositada en mí desde que llegué al Ceit y el esfuerzo realizado para que esta tesis salga adelante. Tengo claro que, sin tu apoyo y resolución a la hora de empezar la tesis, yo jamás habría tomado el camino de la investigación que hoy tanto disfruto y que, desde luego, hoy no estaría escribiendo estos agradecimientos. A mi codirector Gorka Sánchez, muchísimas gracias por tu cercanía y paciencia a la hora de trabajar conmigo en todo lo relacionado con el CFD. A pesar de que la tesis no integre finalmente el trabajo realizado en este campo, creo que la utilización del CFD en aguas residuales acabará siendo habitual en el futuro y que lo aprendido me será muy útil. Gracias a los dos por trabajar con tanta honestidad y rigor y por encontrar el equilibrio de hacerlo de una manera tan humana.

Bereziki Izaro eskertu nahiko nuke, tesiari egindako ekarpen ikaragarriagatik, liburuan idatzita geratzen diren eta ez direnengatik. Benetan baloratzekoa da gauza txiki eta handietan egin duzun lan guztia, eta nola beti lagundu izan didazun inoiz ere aurpegi txarrik jarri gabe. Mila esker tesi hau aurrera eraman ahal izaten horrenbeste laguntzeagatik.

I would like to thank my supervisor in Australia, Phil Schneider, for accepting me in Murdoch University as a visitor PhD student. Both your advice and friendship are

truly appreciated. I would also like to thank Laynard, all the staff from Murdoch University and all the people I met in Australia. You all made it a great experience.

Al centro tecnológico Ceit-BRTA y a la Universidad de Navarra por haberme dado la oportunidad de realizar esta tesis y permitirme colaborar como ayudante en varias asignaturas. Al Gobierno Vasco por financiar parte de la investigación con las becas Predoc y Predoc de Movilidad (Egonlabur) y a Caixabank por su Beca de Movilidad.

Quisiera agradecer a mis compañeros de Ceit por haber hecho que estos ¡¡seis!! años pasen volando. A Enrique, director de la División de Agua y Salud por apoyar mi continuidad en el centro y permitir así que siga aprendiendo en esta nueva etapa. A Eduardo por la gran ayuda que ha supuesto para sacar adelante los artículos y de paso estructurar parte del contenido de la tesis. También, por la cercanía mostrada desde el día en que entré en Ceit para hacer la entrevista. A Luis Sancho, es un placer trabajar con alguien que siempre está dispuesto a enfocar las cosas con positividad y que favorece de tal forma el buen funcionamiento del grupo. A Tamara por ayudarme cada vez que he necesitado algo de West y por todo lo que me aporta en el día a día. A Luis Larrea, Ion Irizar, Sergio, Myriam y Garbiñe por prestarme ayuda cada vez que lo he necesitado. A Mikel Azcona y su entusiasmo, gracias por todo el trabajo realizado durante los primeros años, que nos permitió entender mejor el proceso de precipitación. A los investigadores de la División de Materiales por facilitarme el uso de sus equipos y ayudarme desinteresadamente cada vez que lo he requerido. A Alain y Jaime, por ser unos auténticos fueras de serie y solucionar todos y cada uno de los problemas informáticos y experimentales que me han surgido a lo largo del proceso de realizar la tesis.

A Yaiza y a Jon por su amistad y compañía durante este viaje como doctorandos. Ha sido un camino largo, pero vamos acabándolo. Al resto de compañeros que han ido pasando estos años: Maider, Juan, Leire, Clemens, Elli, Luismi, Jesús y Andreu. A los alumnos que han estado en el departamento haciendo prácticas y PFGs. Al triangulo del mal, lo conformen quienes lo conformen.

A un nivel más personal me gustaría agradecer a mi cuadrilla Kondarrak, a mis amigos de la uni y a mis amigos de Madrid, por todo lo vivido con ellos durante estos años.

Por último, quisiera agradecer a mi familia el cariño y apoyo que me ha proporcionado siempre. A mis aitonas Ramón y Angelines, me da mucha pena no poder compartir el día de la presentación de la tesis con vosotros. No os preocupéis, la cabeza está encima de los hombros. Hondarribiko familia denari, attona eta amona, osaba-izebak eta lehengusuak, behar baino gutxiago ikusi arren oso presente zaituztet. Y por supuesto, a los de casa. Iñaki eta Ramon eta ama eta atta. Mila esker nigatik egiten duzuen denagatik ez da hitzik eskertzeko egunero ematen didazuten dena.

Eskerrik asko denei

Beñat

ABSTRACT

Struvite ($MgNH_4PO_4 \cdot 6H_2O$) precipitation is a promising solution for phosphorus recovery in wastewater treatment plants. Controlled struvite precipitation can help to reduce eutrophication in the receiving waterways, fight global phosphorus scarcity and reduce operational problems generated by the uncontrolled precipitation of the mineral in the pipes. Due to the generated interest, the description of the precipitation process has been already included in existing wastewater treatment modelling libraries.

However, following the classic wastewater treatment modelling approach, the process has been generally included as a one-step kinetic model. This one-step model type is limited for technological design and optimization purposes, as it does not include information about the mechanisms by which the precipitation occurs, nor the particle size distribution, a key variable for the performance of struvite as an effective fertilizer.

Therefore, the aim of this thesis has been to upgrade existing one-step kinetic models by developing a mathematical model that could describe in detail the mechanisms occurring in struvite precipitation in order to be able to predict the resulting particle size distribution. This model is a population balance model in which hydrodynamic effects have been considered.

The population balance model has been constructed according to Ceit's plant wide model methodology, guaranteeing mass and charge balance. Therefore, it can be combined with the simulation of other unit processes used to describe wastewater treatment plants in a systematic and straightforward way. A sensitivity and collinearity analysis performed in the thesis, demonstrated that the model is coherent in its structure and valid to represent struvite precipitation processes.

In order to incorporate the hydrodynamic effects to the model, results obtained in an experimental campaign where struvite precipitation was analysed under different mixing and saturation conditions in two different experimental set-ups, were used. Obtained results showed that a higher mixing intensity could be linked with a faster pH decay, an increasing particle density and lower particle size. These effects were included in the population balance model using a calibration procedure based on Bayesian Monte Carlo techniques. From the calibration procedure, new kinetic laws were proposed for struvite nucleation and growth, where the effect of the hydrodynamics had been decoupled by explicitly including the shear rate as a process variable.

RESUMEN

La precipitación de estruvita ($MgNH_4PO_4 \cdot 6H_2O$) es una solución prometedora para la recuperación de fósforo en estaciones depuradoras de aguas residuales. La precipitación controlada de estruvita puede ayudar a reducir la eutrofización provocada por los vertidos de la depuradora, combatir la escasez global de fósforo y reducir los problemas operacionales generados por la precipitación incontrolada del mineral en las tuberías. Debido al interés generado, la descripción del proceso de precipitación ya se ha incluido en las librerías de modelado de tratamiento de aguas residuales existentes.

Sin embargo, siguiendo el enfoque clásico de modelado de tratamiento de aguas residuales, el proceso se ha incluido generalmente con una cinética de un solo paso. Este hecho limita el uso del modelo matemático para fines de diseño y optimización de tecnologías, ya que no se consideran ni los mecanismos de precipitación ni la distribución del tamaño de partícula, siendo ésta una variable clave en el desempeño de la estruvita como fertilizante.

Por lo tanto, el objetivo de esta tesis ha sido mejorar los modelos cinéticos de un paso existentes mediante el desarrollo de un modelo matemático que describe en detalle los mecanismos que ocurren en la precipitación de estruvita para poder predecir la distribución del tamaño de partícula resultante. Este modelo es un modelo de balance poblacional en el que se han considerado efectos hidrodinámicos.

El modelo de balance poblacional se ha construido siguiendo la metodología de modelado integral de planta (‘Plant Wide Model’) de Ceit, garantizando el balance de masa y carga. Por lo tanto, se puede combinar con la simulación de otros procesos que ocurren en las estaciones depuradoras de aguas residuales de una manera sistemática y sencilla. Un análisis de sensibilidad y colinealidad realizado en la tesis, demostró que el modelo es coherente en su estructura y válido para representar procesos de precipitación de estruvita.

Para incorporar los efectos hidrodinámicos al modelo, se utilizaron los resultados obtenidos en una campaña experimental donde se analizó la precipitación de estruvita bajo diferentes intensidades de agitación y grado de saturación. Los resultados obtenidos mostraron que una mayor intensidad de agitación podría estar relacionada con una caída más rápida del pH, un aumento del número de partículas y un menor tamaño medio de las partículas obtenidas. Estos efectos se incluyeron en el modelo de balance de población utilizando una metodología de calibración basada en inferencia bayesiana. A partir de la metodología de calibración, se propusieron nuevas leyes cinéticas para la nucleación y el crecimiento de la estruvita, donde el efecto de la hidrodinámica está desacoplado al incluir explícitamente la cizalladura como una variable de proceso.

LABURPENA

Estrubitaren ($MgNH_4PO_4 \cdot 6H_2O$) hauspeaketa aukera erakargarria da araztegietako hondakin-urek dakarten fosforoa berreskuratzeko. Estrubitaren kontrolpeko hauspeaketak hondakin-urak jasotzen dituzten ibai eta lakuetan eutrofizazioa murrizteko, fosforoaren urritasun globalari aurre egiteko eta araztegiko hodietan mineralaren kontrolik gabeko hauspeaketak sortzen dituen arazoak murrizteko lagun dezake. Sortutako interesa dela eta, hauspeaketa prozesuaren deskribapena aurretik sortutako eredu matematikoetan sartu izan da dagoeneko.

Hala ere, hondakin-uren tratamenduak deskribatzeko erabiltzen diren eredu matematikoen ikuspegi klasikoa jarraituz, prozesua orokorrean urrats bakarreko eredu zinetiko gisa deskribatu da. Urrats bakarreko eredu mota hauek teknologien diseinu eta optimizaziorako mugatuak dira, ez baitute kontuan hartzen hauspeaketaren mekanismoen inguruko informaziorik, ezta partikulen tamaina ere, azken hau funtsezko aldagaia izanik estrubita ongarri bezala erabiltzerakoan.

Hori dela eta, tesi honen xedea urrats bakarreko eredu zinetikoak hobetzea izan da, estrubitaren hauspeaketan gertatzen diren mekanismoak zehatz-mehatz deskribatu eta mekanismo hauen ondorioz sortutako partikula tamainak aurreikusteko gai den eredu matematikoa garatuz. Eredu hau efektu hidrodinamikoak kontuan hartu dituen populazio eredu matematikoa da.

Populazio eredu matematikoa Ceiten araztegi eredu integral (plant wide model) metodologiaren arabera eraiki da, masa eta karga oreka bermatuz. Hori dela eta, hondakin uren araztegietan erabilitako beste prozesuen simulazioarekin konbinatu daiteke era sistematiko eta zuzenean. Tesian egindako sentsibilitate eta kolinearitate analisiak frogatu du eredua koherentea dela bere egituran eta estrubitaren hauspeaketa prozesuak irudikatzeko balio duela.

Efektu hidrodinamikoak ereduan txertatzeko, kanpaina esperimental batean lortutako emaitzak erabili ziren, non estrubitaren hauspeaketa nahasketa eta saturazio baldintza desberdinetan aztertu zen, bi multzo esperimental desberdinetan. Lortutako emaitzek erakutsi zuten nahasketa intentsitate handiagoak pH-aren jetsiera azkarragoa, partikula dentsitate handiagoa eta partikula tamaina txikiagoa dakartzala. Efektu horiek populazio eredu matematikoan sartu ziren, Bayesian-Monte Carlo tekniketan oinarritutako kalibrazio prozedura erabiliz. Kalibrazio prozeduratik, lege zinetiko berriak proposatu ziren estrubitaren nukleazio eta hazkuntzarako. Lege berri hauetan hidrodinamikaren eragina kontuan hartu da ebakidura-tasa esplizituki aldagai gisa sartuz.

TABLE OF CONTENTS

LIST OF FIGURES

LIST OF TABLES

NOTATION AND ABBREVIATIONS

Abbreviations

a_i (mol/l)	Activity of ion i
a_{Seed}	Initial specific area of surface per gram of seed
A	Surface area of the crystals
ADM	Anaerobic Digestion Model
AE	Algebraic equation
A_i (m^2)	Total area of the crystals of size i
A_i' (m^2)	Effective area of the crystals of size i
ASM	Activated Sludge Model
A_{S0}	Activation term for the initial mass of seed
A_{SN}	Activation term for the case when there is not seed material
A_{TSS}	Activation term for the suspended solids
A_1	Constant for power number calculation in unbaffled vessels
A_2	Constant for power number calculation in unbaffled vessels
A_3	Constant for power number calculation in unbaffled vessels
b (m)	Stir bar diameter
B	Birth Function
B_C	Constant for nucleation kinetic expression
B-HSI	High Saturation Index in Block B
B-LSI	Low Saturation Index in Block B
B-MSI	Medium Saturation Index in Block B

B_0 (nuclei/day)	Nucleation Rate
c	Concentration
c_e	Solubility/Equilibrium concentration
c_i	Concentration of element i
c^*	Concentration in the particle-solution interface
CFD	Computational Fluid Dynamics
CSTR	Continuously Stirred Tank Reactor
Cw_i (g/m^3)	Concentration of i sized crystals
Cw_{TSS} (g/m^3)	Concentration of total suspended solids
d_p (m)	Particle diameter
D	Death Function
D_i	Impeller diameter (m)
DPBM	Discretized Population Balance Model
D_T (m)	Tank diameter
e_K	Difference between the observed k^{th} measured and simulated variable
g (m/s^2)	Gravity constant
G (mm/d)	Linear Growth Rate
f_i	Variation in the parameter
h (m)	Height
HSI	High Saturation Index
Hγ	High shear rate
I	Ionic strength
IAP $(mol/l)^3$	Ion Activity Product
IWA	International Water Association
$k_{B,T}$	Temperature dependent nucleation coefficient
k_{Bol}	Boltzmann constant
k_d	Mass transfer coefficient by diffusion
$k_{D,T}$	Temperature dependent dissolution rate coefficient
$k_{G,T}$	Temperature dependent growth rate coefficient
k_T	Kinetic precipitation/redissolution coefficient
k_s	Rate constant for surface integration
K_A (l/d)	Kinetic constant of aggregation
K_B ($nuclei/d \cdot m^3$)	Kinetic constant of nucleation

K_B' (nuclei·$s^{n_{BS}}$/d·m^3)	Kinetic constant of nucleation independent of the average shear rate
$K_{B,i,z\gamma}$ (nuclei/d·m^3)	Kinetic constant of nucleation for the i^{th} group of exponents and z condition of shear rate
K_G (mm/d)	Kinetic constant of growth
K_G' (mm^{α}·$s^{n_{BS}}$/d)	Kinetic constant of growth independent of the average shear rate
$K_{G,i,z\gamma}$ (mm^{α}/d)	Kinetic constant of growth for the i^{th} group of exponents and z condition of shear rate
K_r	Generic kinetic constant
K_{sp} $(mol/l)^3$	Solubility Product Constant
K_1	Constant low numeric value for numeric stability
K_2	Constant low numeric value for numeric stability
K_3	Constant low numeric value for numeric stability
L (mm)	Crystal Length
LH	Latin Hypercube
LH-OAT	Latin Hypercube-One Factor at a Time
L_i (mm)	Characteristic Length of i size
LSI	Low Saturation Index
$L\gamma$	Low shear rate
m	Total number of variables
$mesf_i$ (g)	Mass of a single sphere of size i
M(·)	Sum of the square of the normalized differences for all the observed variables
Mg	Magnesium
M_O	Model Outputs
M_{seed}	Time dependent mass of seed
MSI	Medium Saturation Index
MW_i (g/mol)	Molecular Weight of compound i
$M\gamma$	Medium shear rate
n	Total number of parameters
n_A	Aggregation Kinetic Exponent
n_B	Nucleation Kinetic Exponent
n_{BS}	Exponent of the shear rate effect in the nucleation
$n_{B,i}$	Nucleation Kinetic Exponent in the i^{th} parameter set

n_d	Population Density
n_G	Growth Kinetic Exponent
n_{GS}	Exponent of the shear rate effect in the growth
$n_{G,i}$	Growth Kinetic Exponent in the i^{th} parameter set
$n_{G,C}$	Exponent for size dependent growth
n_i	Number of particles in the i^{th} bin
n_j	Number of particles in the j^{th} bin
n_r	Kinetic Exponent
N	Nitrogen
N_D	Number of Particles per volume unit
N_K	Number of the bin of the biggest crystal size
N_M	Adjustable parameter in the calculation of the likelihood function
N_{OBS}	Number of observed variables
N_P	Power Number
N_{Part}	Number of particles of the fertilizer
NRM	Nutrient Recovery Model
N_S (s^{-1})	Stirrer Speed
OAT	One Factor at a Time
p	Number of sampled parameter set
p(y)	Probability of having the observed data
$p(y\|\theta)$	Likelihood function
$p(\theta)$	Prior knowledge of the parameters
$p(\theta\|y)$	Posterior probability density function
P	Phosphorus
PBM	Population Balance Model
PBT	Pitched 4-bladed impeller
PC-PWM	Physico-Chemical Plant Wide model
P_i (W)	Power input
PSD	Particle Size Distribution
PWM	Plant Wide Model
r (mm)	Radius
Re	Reynolds Number
$s_{i,j,k}$	Sensibility caused in i^{th} variable, by a change in j^{th} parameter in k^{th} point

s_0	Dimensionless parameter representing initial seed surface
S	Sensitivity Matrix
S_a	Absolute Supersaturation
SI	Saturation Index
SIM_{ij}	Simulation output for the k^{th} parameter pair and i^{th} group
$\tilde{S}_k$	Normalized Sensitivity Matrix of k parameters
S_r	Supersaturation Ratio
S-HSI	Simulation case study of High Saturation Index
S-LSI	Simulation case study of Low Saturation Index
S-MSI	Simulation case study of Medium Saturation Index
t_{ind} (s^{-1})	Induction time
T	Temperature
Total M (·)	Sum of the normalized differences obtained with each best parameter set for each shear rate.
v	Volume of the smallest sphere
V (m^3)	Reactor Volume
V_l (l)	Reactor Volume in litre units
V_{fert}	Volume of the recovered fertilizer
WRRF	Water Resource Recovery Facility
WWTP	Wastewater Treatment Plant
X_i (g)	Total mass of the i sized bin
y	Observed data
z_i	Valence of the ion i

Greek symbols

α	Area Exponent
α,i	Area Exponent in the i^{th} parameter set
$\alpha_{G,C}$	Constant for size dependent growth
β (l/d)	Aggregation Rate
β_C	Vector of coefficients
γ (s^{-1})	Average shear rate
γ_B	Parameter to describe the error model
γ_i	Activity coefficient of ion i
γ_k	Collinearity Index of the k parameter set
$\delta_{k,j}$	Total influence of the parameter in each point

Δc (mol/l)	Concentration driving force
ΔG_{hom}^{crit}	Free enthalpy of activation
θ	Parameter set
θ_{An} (°)	Angle between the agitator and the horizontal surface
θ_i	i^{th} parameter
λ_k	Smallest Eigenvalue of the Matrix
μ (kg/m·s)	Dynamic Viscosity
ν	Number of moles of ions per mole of electrolyte
ρ_s (g/m^3)	Density of the solid
ρ_L (kg/m^3)	Liquid density
ρ_k	Importance Index
ρ_R	Kinetic rate
σ	Relative supersaturation
τ	Shear stress
Φ	Shape factor

CHAPTER 1

INTRODUCTION

1.1 BACKGROUND

Circular economy is an economic framework that looks beyond the current take-make-waste linear economic model and aims to redefine economic growth, following the next three principles (The Ellen MacArthur Foundation, 2020):

- Design out waste and pollution.
- Keep products and materials in use.
- Regenerate natural systems.

Consequently, circular economy promotes cross-sector collaboration to recycle and re-use the by-products of industrial or human activity. This collaboration holds benefits for both, the environment and the economy (European Commision, 2015).

The general interest for using resources in a more sensitive way matches with a recent change in wastewater vision. Over the years, the biggest wastewater related concern has been the elimination of contaminants to fulfil existing legislation. Therefore, the development of technologies followed that objective. Despite reduction of contaminants is still the primary objective for wastewater industry, recently numerous case studies have shown that the role that wastewater plays could start to change: due to the global scarcity of some materials, wastewater perception is shifting from being considered a polluted source with contaminants to be eliminated, to a source of interesting elements to be recovered. Therefore, wastewater treatment

plants (WWTPs) have been started to be conceived as water resource recovery facilities (WRRFs). Nowadays, organic and inorganic matter, nutrients, energy or water itself can be recovered in WRRFs (Guest *et al.*, 2009). Accordingly, challenges for investigation and development in WRRFs are oriented to design and optimization of new and existing element recovery technologies.

One of the elements that can be recovered in WRRFs is phosphorus (P). Traditionally, P has been considered a pollutant in wastewater. Main challenges associated with its management are the operational problems caused by its uncontrolled precipitation (Buck, 2012; Mudragada *et al.*, 2014) and eutrophication, an environmental problem in the receiving waterways, generated by the combined release of nitrogen (N) and P. Therefore, habitual efforts in P-rich wastewater streams focused on the removal of that element. However, in light of its recent consideration as a critical raw material (European Commission, 2018) and the expected peak in its net production in the 21st century (Cordell and White, 2011; Sverdrup and Ragnarsdottir, 2011), P recovery from wastewater has become an emerging concern (Peng *et al.*, 2018). Municipal wastewater has the potential to substitute a significant portion of the increasing global demand of P (Amann *et al.*, 2018), as in Europe alone about 227 kt P/year ends up in communal sewage sludge and extra 74 kt P/year is lost in the effluents of urban and decentralized WWTPs (van Dijk *et al.*, 2016). Due to the recovery potential of P and its importance, over 30 processes now exist (at varying developmental stages) by which P can be recovered in WRRFs (Cieślik and Konieczka, 2017).

Among the available options to recover P in WRRFs, controlled precipitation of mineral phosphates, most notably struvite (magnesium ammonium phosphate hexahydrate, $MgNH_4PO_4{\cdot}6H_2O$), has gained interest in recent years (Peng *et al.*, 2018; Robles *et al.*, 2020). Struvite is a salt, equimolar in P, N and magnesium (Mg), which may be used as an effective fertilizer (i.e. Crystal Green ® obtained from Pearl™ and BioSTRU ® from NuReSys™ are certified fertilizers in US/UK and Belgium, respectively) (Desmidt *et al.*, 2015). The overall stoichiometry governing the precipitation process is:

$$Mg^{2+} + NH_4^+ + PO_4^{3-} + 6H_2O \rightleftarrows MgNH_4PO_4 \cdot 6H_2O \downarrow \quad \textbf{1.1}$$

Main advantages of recovering struvite are: (1) it reduces operational costs in WRRFs associated with the maintenance of reactors and pipes due to blockage of P

salts, (2) it fights global P scarcity and (3) it reduces eutrophication problems in receiving waterways. Following this interest, some technologies have been recently developed that demonstrate the feasibility of the full-scale process (Egle *et al*., 2016) and around 100 full scale struvite recovery units are available worldwide (European Sustainable Phosphorus Platform, 2020). Most of the recovery units are located in North America, Japan and Europe (mainly Belgium, Netherlands, Germany and Austria) (Desmidt *et al*., 2015) and the biggest installation is located in the Chicago Stickney WRRF, producing around 9,000 t/year of struvite (European Sustainable Phosphorus Platform, 2020). Therefore, full scale struvite recovery is technically feasible, while the economic feasibility is influenced by the great variability of cost of the available technologies (Desmidt *et al*., 2015) and the price of the recovered product (Yetilmezsoy *et al*., 2017).

Therefore, struvite is a well-known fertilizer that can be obtained in WRRFs by precipitation (Le Corre *et al*., 2009). Precipitation is a physico-chemical process in which a sparingly soluble solid phase is relatively rapidly formed from a liquid phase. This process is widely employed in the industry for separation and purification of materials (Myerson, 2001; Nagy *et al*., 2013) and its relevance is increasing in wastewater treatment.

Considering the current and future importance of precipitation process in sustainable wastewater treatment, precipitation of struvite (and other materials) has already been included in mathematical modelling and simulation libraries for WRRFs (Ikumi *et al*., 2014a; Lizarralde *et al*., 2015; Solon *et al*., 2017). Therefore, existing libraries can predict the amount of obtained solid in a recovery reactor, based on the kinetic of precipitation and thermodynamics. In addition, these modelling and simulation libraries often combine information from the biological, chemical and physico-chemical processes in the WRRF with its economic performance. This is a necessary information to assess the suitability of installing a recovery technology by evaluating its effect on the global WRRF behaviour. The opportunity of considering such effects while minimizing experimental needs can explain why mathematical modelling and simulation tools have been widely used over the last decades to design, operate and optimize wastewater treatment technologies (Fernández-Arévalo *et al*., 2017a, 2017b; Lizarralde *et al*., 2019). However, existing modelling libraries present some limitations for the optimum design and operation of the technologies.

It is known that struvite performance as a fertilizer depends on the obtained particle size distribution (PSD) (Tarragó *et al*., 2016). This PSD will be conditioned by the inner mechanisms of the precipitation: primary nucleation (homogeneous and heterogeneous), secondary nucleation, growth, aggregation, attrition and breakage of particles. The weight of each mechanism in the obtained product is determined by the experimental conditions in the reactor, namely pH, supersaturation level, mixing energy, temperature and the presence of foreign ions in the precipitating solution (Le Corre *et al*., 2009). These experimental conditions vary in the existing technologies, as they show significant differences on the operation (continuous versus batch, different hydraulic retention times, etc.) and obtained product (Tarragó *et al*., 2016). Neither the information on the PSD nor the inner mechanisms of the process are rigorously included in previously named WRRF modelling approaches, where precipitation is defined as a one-step process. As considering the PSD and inner mechanisms is essential for the correct design, operation and optimization of element recovery reactors, one-step precipitation models have to be upgraded with new modelling frameworks for wastewater treatment modelling as the population balance model (PBM).

In order to illustrate the increasing interest of some of the aforementioned research areas, Figure 1.1 includes the evolution in the number of publications in Scopus for the terms (A) wastewater + struvite + recovery (B) wastewater + circular + economy (C) wastewater + precipitation (D) population + balance + model.

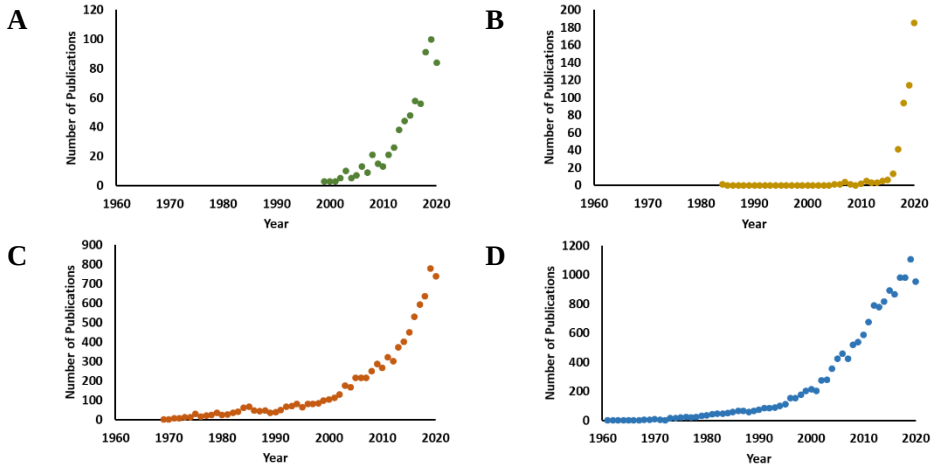

Figure 1.1: Evolution in the number of publications in Scopus for: (A) wastewater + struvite + recovery (B) wastewater + circular + economy (C) wastewater + precipitation (D) population + balance + model.

1.2 PROBLEM IDENTIFICATION

The PBM can successfully describe the evolution in time and space of the distribution of properties of a group of discrete entities (particles, bubbles, cells, etc.) dispersed in a continuous phase. It typically considers an additional internal coordinate, which is some measure of the particles' size. It includes explicitly inner mechanisms of the precipitation process and is able to predict the evolution of a PSD in a reactor. The PBM is a widely accepted tool for precipitation process modelling in industrial crystallization, however, only recently has been used to represent WRRF unit processes (Nopens *et al*., 2015). PBM has already been proved to be successful to track changes in the PSD in the struvite precipitation (Galbraith *et al*., 2014; Hanhoun *et al*., 2013; Triger *et al*., 2012). This evidences the great potential of the PBM for the correct prediction of the process' outcome and its optimization. However, in order to be fully accepted for design and optimization of resource recovery technologies from wastewater, there are three main aspects that have to be addressed.

Firstly, PBMs have generally been defined using number of particles as the dependent variable of the process, which is coherent with the model purposes, but, can lead to mass discontinuities (Hounslow *et al*., 1988). Although partially solved (Galbraith *et al*., 2014), this problem would make them incompatible with conventional models used in the wastewater treatment framework, which are mainly constructed on the basis of mass balances around the unit to be described as in the International Water Association (IWA) models: Activated Sludge Model (ASM) and Anaerobic Digestion Model (ADM) (Batstone *et al*., 2002; Henze *et al*., 2000). For a successful implementation of PBM in wastewater treatment industry, mass discontinuity must be avoided first. Using mass as internal coordinate automatically satisfies the mass balance (Scarlett, 2002). In addition, it allows to represent the PBM as a dynamic mass balance explicitly affected by the mechanisms of precipitation, as it is usually done in standardized methodology for wastewater treatment modelling.

Secondly, calibrated parameter values for the parameters defining inner mechanisms of the precipitation of struvite are very variable in the literature (Galbraith *et al*., 2014; Hanhoun *et al*., 2013; Mehta and Batstone, 2013). The same happens for other compounds, too (Chen *et al*., 2002; Ruan *et al*., 2016). Mechanisms occur simultaneously and obtaining meaningful experimental data to attribute to each mechanism its real effect on the precipitation is difficult, making calibration a very

challenging issue. Using mathematical analysis tools to evaluate the possibility of obtaining trustworthy parameter values will increase the confidence in the modelling framework.

Thirdly, while most of the experimental variables affecting the process have been considered in existing PBMs representing struvite precipitation (Galbraith *et al*., 2014; Hanhoun *et al*., 2013; Triger *et al*., 2012), there is a clear gap in the literature regarding inclusion of the mixing effects in the PBMs. PBMs have been mainly modelled and simulated in virtual continuously stirred tank reactors (CSTR), what limits their capacity for design and optimization of technologies. In this regard, taking into account mixing effects in the model construction would be a step forward in the understanding of precipitation processes and the natural step towards a more descriptive modelling. To this effect, some efforts have been already done for other compounds by including explicitly the shear rate, an operational variable related with the local velocity of the flow in each point (Ilievski *et al*., 2001), in the aggregation rate expressions (Hounslow *et al*., 2013). However, the effect of mixing in the mechanisms is still poorly understood and it should be further studied for its modelling. In addition, ignoring mixing effects could also be related with the shifting parameter values found in the literature, as they could be influenced by the mixing intensity for which they were obtained.

Therefore, this thesis is focused on the three previously identified issues and intends to answer them by constructing a PBM that ensures mass continuity, where the identifiability of the parameters is analysed and which is capable to reproduce experimentally observed mixing effects.

1.3 OBJECTIVE OF THE THESIS

The aim of this thesis is to develop a mathematical model that can describe in detail the mechanisms occurring in a precipitation process for struvite recovery. Due to the process characteristics and specifications of new precipitation technologies, two novel approaches have been implemented: a mass-based PBM that guarantees mass continuity and the consideration of hydraulic effects in the precipitation mechanisms.

In order to achieve this aim, the following objectives are established:

- A PBM for modelling struvite nucleation, growth and aggregation has to be designed, constructed and implemented.

  - Based on existing approaches, a new mass-balance-based PBM for describing struvite precipitation needs to be developed. This model has to be constructed according to Ceit's plant wide model (PWM) methodology, guaranteeing mass and charge balance. Thus, its integration in a simulation of a WRRF with other unit processes will be systematic and straightforward.
  - The theoretical parameter identifiability of the constructed model has to be evaluated using model analysis tools as sensitivity analysis and collinearity analysis in order to increase the trustworthiness in the modelling framework.

- The effect of the saturation index (SI) and local mixing intensity (related to the shear rate), on struvite nucleation and growth has to be experimentally identified.
  - Experimental campaigns where the effect of SI and local mixing intensity are analysed have to be done in small size batch experiments.
  - The necessary data for model calibration purposes has to be collected.
- The shear rate has to be considered as a process variable in the previously constructed mass-based PBM.
  - A methodology has to be followed where the experimentally observed effects are evaluated for its inclusion in the kinetic rates of the mechanisms.
  - Based on the previous evaluation of the effect of the shear rate and SI, new expressions for the kinetic rates of the PBM where these operational variables are explicitly included, have to be proposed.

1.4 CONTENTS OF THE THESIS

This thesis is distributed in six chapters, which include the following information.

Chapter 1 (Introduction) includes the context in which the research done for this thesis has been carried out. It also includes the general objectives and the summary of the contents of the thesis.

Chapter 2 (State of the art) includes general information necessary to understand the nature of the research done. This information covers the fundaments of the

precipitation process, the modelling of precipitation process in conventional wastewater treatment modelling and the PBM.

Chapter 3 (A new mass-based discretized population balance model for precipitation processes: application to struvite precipitation) includes the general description and equations of a PBM based on mass and charge continuity. In addition, a sensitivity and a collinearity analysis are performed to evaluate the identifiability of the parameters.

Chapter 4 (Effect of the shear rate and supersaturation on the nucleation and growth of struvite in batch stirred tank reactors) includes an experimental study where the effect of the SI and the shear rate in the pH evolution and resulting PSD have been analysed in several struvite precipitation tests.

Chapter 5 (Inclusion of shear rate effects in the kinetic rates of a discretized population balance model: application to struvite precipitation) includes the analysis performed regarding the necessity of including the shear rate as a process variable in the kinetic rates of nucleation and growth. For this issue the mass-based PBM presented in Chapter 3 and the experimental data gathered in Chapter 4 are used. Chapter 5 also includes new expressions where the effect of the shear rate is decoupled from the kinetic constants of the mentioned mechanisms. A comparison between the experimental results and simulation outputs is also provided for different mixing intensities and initial SI.

Finally, **Chapter 6** (Conclusions and future research lines) summarises the main conclusions of the thesis and proposes further research lines.

CHAPTER 2

STATE OF THE ART

This chapter covers classic and up to date information, necessary to understand the nature of the research done. The chapter is divided in four sections: first, the fundaments of precipitation are briefly described. Second, a short description of the main modelling frameworks that have been used in wastewater sector to represent precipitation are included. Third, the PBM framework is described. Finally, the information provided in the chapter is summarized. Some of the aspects covered in this chapter will be repeated or further assessed in the Background section of chapters 3, 4 and 5 in order to better understand the nature and need of the work done in each chapter.

2.1 PRECIPITATION PROCESS: FUNDAMENTALS

Crystallization is a phase change phenomena in which a solid phase is obtained from compounds dissolved in a solution. This phase change occurs due to an instability generated in the solution, often by cooling the solution, evaporating the solvent or by increasing the solute concentration (Pastor, 2008). On the other hand, in the precipitation process, also known as reactive crystallization, the instability is not generated by a physical change in the solution but due to the chemical reaction of two soluble compounds that result in a non-soluble product (Myerson, 2001).

Main aspects of chemical equilibrium and the mechanisms by which precipitation occurs have been studied for years. These concepts are briefly described in this

section. For a fuller explanation, the interested reader is referred to the existing literature (Jones, 2002; Le Corre *et al.*, 2009; Mullin, 2001; Myerson, 2001).

2.1.1. Chemical equilibrium definitions

2.1.1.1. Solubility

The solubility, c_e, is the amount of solute required to make a saturated solution under certain conditions (Myerson, 2001). In other words, it is the maximum quantity of a solute that can be dissolved in a certain amount of liquid under specific conditions of temperature and pressure (Pastor, 2008). Its units are usually g/l or mol/l (Le Corre *et al.*, 2009).

Usually, the solubility of a solute increases with the temperature, but there are some exceptions to this general trend (Mullin, 2001). A diagram representing generic dependence of the solubility of a chemical compound with respect to the temperature is included in Figure 2.1. For the specific case of struvite, the solubility has been reported to increase with temperature (Crutchik and Garrido, 2016; Le Corre *et al.*, 2009). However, some authors have found a maximum in its solubility between 25 ºC and 35 ºC and a decrease at higher temperatures (Borgerding, 1972; Hanhoun *et al.*, 2011). In any case, the effect of the temperature is not critical on struvite precipitation (Le Corre *et al.*, 2009).

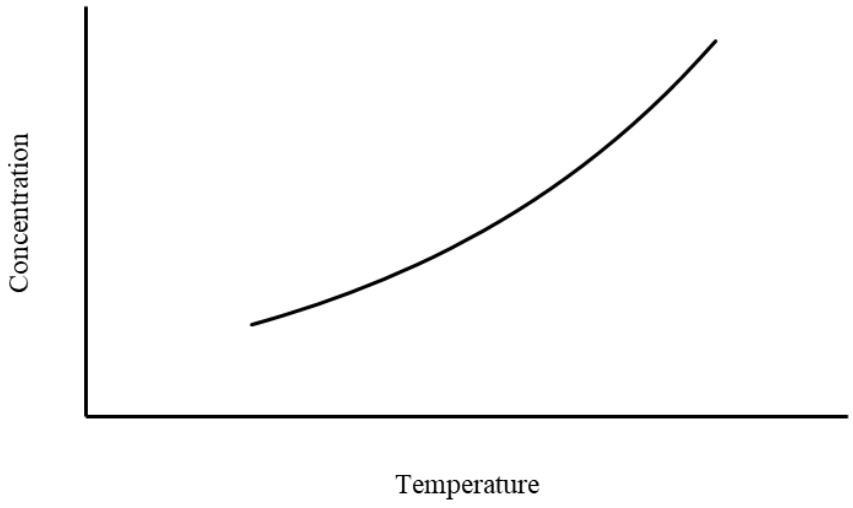

Figure 2.1: Solubility curve, adapted from (Pastor, 2008).

The effect of pressure is generally negligible in the precipitation systems (Mullin, 2001) and its effect is not usually reported in struvite precipitation studies.

2.1.1.2. Saturation

Saturation describes the potential of forming a precipitate in a solution by comparing the solute concentration with its solubility. This is a good starting point to understand why precipitation occurs and how it can be produced (Jones, 2002). For a particular solution three main possible states are usually defined (Pastor, 2008):

1. Stable (undersaturated): The solute concentration is smaller than the solubility. When this occurs, if there is any crystal in the solution it will tend to dissolve.
2. Metastable (supersaturated): It is a supersaturated solution in which crystals can grow but there is not spontaneous nucleation.
3. Labile or instable (supersaturated): It is more saturated than the metastable zone. Both particle growth and nucleation can occur.

For a compound where the solubility increases with the temperature, these states are included in a general diagram phase (see Figure 2.2).

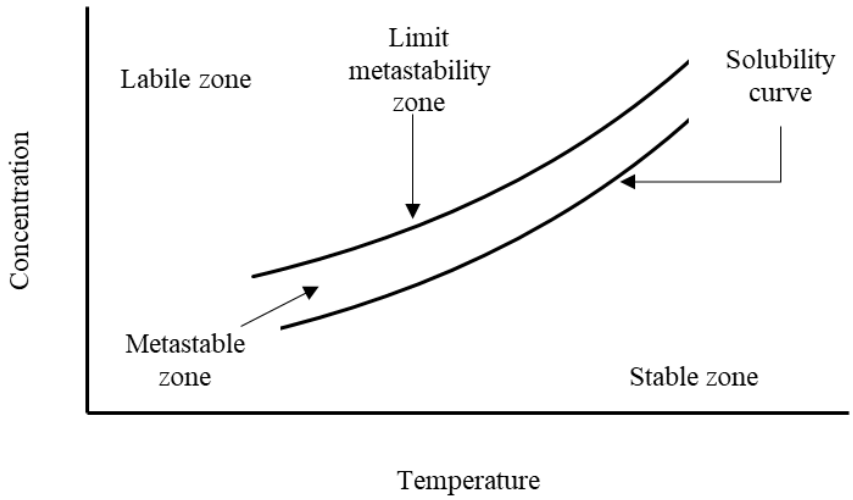

Figure 2.2: Saturation diagram, adapted from (Pastor, 2008).

Thus, supersaturation is a deviation from the equilibrium situation and the necessary condition for precipitation to happen. It is the key variable in any precipitation system as nucleation and growth of crystals are affected by it. There are different mathematical expressions to quantify supersaturation in a system. Some of the most common are (Mullin, 2001):

- Concentration driving force: $\Delta c = c - c_e$
- Supersaturation ratio: $S_r = \frac{c}{c_e}$
- Relative supersaturation: $\sigma = \frac{c - c_e}{c_e} = S_r - 1$

where c is the concentration of the compound being evaluated. As it can be seen in the equations, the units of the concentration driving force will be concentration units (usually mol/l or g/l), while the supersaturation ratio and relative supersaturation do not have units.

2.1.1.3. Solubility product

When precipitation of sparingly soluble electrolytes is being analysed, supersaturation is expressed in terms of the solubility product (Mullin, 2001). The solubility product (K_{sp}) is the product of the concentration of the ions forming a salt in the equilibrium. Considering the generic salt $A_zB_{y(s)}$, the ions dissolved from it are:

$$A_zB_{y(s)} \leftrightarrow zA^{y+} + yB^{z-} \quad \textbf{2.1}$$

where z and y are the stoichiometric coefficients of A and B elements, which form ions with y+ and z- valences respectively.

The solubility of these ions would be:

$$c_e = \frac{[A^{y+}]_e}{z} = \frac{[B^{z-}]_e}{y} \quad \textbf{2.2}$$

Being $[A^{y+}]_e$ and $[B^{z-}]_e$ the concentrations of $A^{y+}$and B^{z-} ions in equilibrium.

The solubility product is:

$$K_{sp} = [A^{y+}]_e \cdot [B^{z-}]_e \quad \textbf{2.3}$$

Thus, for sparingly soluble electrolytes, supersaturation expressions previously used can change as follows:

- Absolute supersaturation: $S_a = ([A^{y+}] \cdot [B^{z-}])^{1/\nu} - \left(K_{sp}\right)^{1/\nu}$
- Supersaturation ratio: $S_r = \frac{c}{c_e} \rightarrow \left(\frac{[A^{y+}] \cdot [B^{z-}]}{K_{sp}}\right)^{1/\nu}$
- Relative supersaturation: $\sigma = \frac{c - c_e}{c_e} \rightarrow \left(\frac{[A^{y+}] \cdot [B^{z-}]}{K_{sp}}\right)^{1/\nu} - 1$

where ν is the mole of ions generated from a mole of electrolyte.

Another common mathematical expression used to represent supersaturation is the saturation index (SI):

$$SI = \log\left(\frac{[A^{y+}] \cdot [B^{z-}]}{K_{sp}}\right) \quad \textbf{2.4}$$

However, the application of these (or other similar) expressions based on the product of ion concentrations and the solubility product is only valid for very diluted and simple systems. When quantifying the precipitation potential in a more complex system, as wastewater, where the interactions with other ions need to be accounted, the activity of the ions has to be considered (Solon *et al*., 2015).

Therefore, in wastewater treatment modelling the aforementioned expressions based on the product of the ion concentration should be improved by using the ion activity product (IAP). The IAP defined for a generic salt $A_zB_{y(s)}$ is:

$$IAP = a_A \cdot a_B \quad \textbf{2.5}$$

The activity of the i^{th} ion, a_i, is the product of the activity coefficient, γ_i (-), and the concentration of the i^{th} ion, c_i (mol/l):

$$a_i = \gamma_i \cdot c_i \quad \textbf{2.6}$$

The activity coefficient can be calculated by different formulas, being the most common in wastewater treatment the Davies approximation to the Debie-Hückel law:

$$\log \gamma_i = 0.51 \cdot z_i^2 \cdot \left(\frac{\sqrt{I}}{1 + \sqrt{I}} - 0.3I\right) \quad \textbf{2.7}$$

Where z_i is the valence (-) of the i^{th} ion and I is the ionic strength, calculated as:

$$I = \frac{1}{2}\sum c_i \cdot z_i^2 \qquad \textbf{2.8}$$

For the specific case of struvite, the supersaturation has been quantified using the absolute supersaturation (Lizarralde *et al*., 2015), the supersaturation ratio (Hanhoun *et al*., 2013), the relative supersaturation (Mehta and Batstone, 2013; Vaneeckhaute *et al*., 2018) or the saturation index (Burns *et al*., 2021; Galbraith *et al*., 2014).

2.1.2. Mechanisms

Precipitation process is a simple yet very complicated phenomena. On one hand, precipitation could be simply understood as a relatively fast two-step process governed by two mechanisms. In the first step, phase separation occurs when small entities known as nuclei are born from the solution (nucleation mechanism). In the second, this entities increase their size until a stable size is reached by reactants consumption (crystal growth mechanism). On the other hand, these two steps take place simultaneously in the chemical reactor and often they are combined with other mechanisms as aggregation and crystal rupture, complicating the identification of the effect of each independent mechanism in the precipitation process.

In addition, the mechanisms are affected by the change in the experimental variables in different ways. For example, the rate of nucleation and growth increases with an increasing degree of supersaturation in the system, but they depend on it on a different order, nucleation exhibiting a stronger dependence (Jones, 2002; Myerson, 2001). Other variables as the mixing, seeding material, presence of ions or temperature can also affect the mechanisms (Le Corre *et al*., 2009).

Despite the difficulty, identifying the weight of each mechanism in the precipitation process under certain experimental conditions is necessary to construct a mathematical model if it is going to be used for design and optimization purposes. In this section, nucleation, growth and aggregation are described as these are the most relevant mechanisms for struvite precipitation (Ye *et al*., 2016) and, consequently, the mechanisms that are considered in the PBM developed in the thesis.

2.1.2.1. Nucleation

Nucleation is the mechanism by which crystals are born within a liquid phase (Mullin, 2001; Pastor, 2008). This mechanism involves the generation of small entities from the liquid that are in the edge of liquid and solid phase. Depending on the existing conditions, some of them will re-dissolve into the liquid and others will become the starting point of the precipitation. As precipitation occurs mostly under conditions of high supersaturation, where nucleation is favoured, the mechanism plays a major role in the process (Myerson, 2001).

In a precipitation system, nuclei can be formed by different types of nucleation. Primary nucleation occurs in the absence of the crystallizing material, while secondary nucleation occurs due to the presence of this crystallizing material. Some authors believe that secondary nucleation is the main source of nuclei in industrial systems (Agrawal *et al.*, 2017) as it is favoured under lower saturation conditions and when there is presence of particles in the system (Mehta and Batstone, 2013). However, primary nucleation still occurs in the presence of particles, especially when the saturation degree in the system is high (Agrawal *et al.*, 2018). This happens because it is a very rapidly occurring local mechanism, which is not directly affected by the presence of other particles (Myerson, 2001). In addition, if the mixing is not good and high saturation zones are found in the reactor, primary nucleation is of relevance and the cause for obtaining crystals with smaller mean particle sizes (Mersmann, 2001).

Nucleation can be further classified by distinguishing between primary homogeneous and primary heterogeneous nucleation and by dividing the secondary nucleation into different categories, as shown in Figure 2.3.

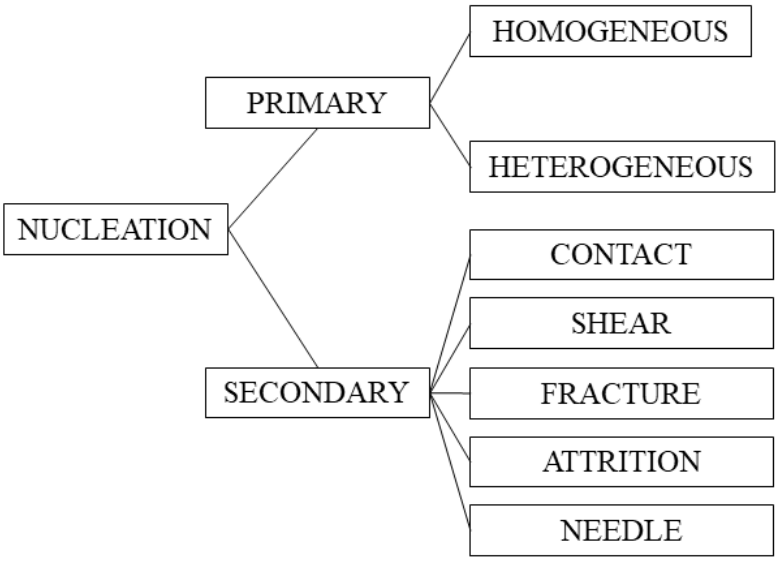

Figure 2.3: Classification of different nucleation types, adapted from (Jones, 2002).

Despite in a real system all nucleation types could happen simultaneously and be of relevance, experimental evidence show that under controlled situations primary nucleation is favoured at high supersaturation and secondary nucleation is favoured at lower saturation (Mehta and Batstone, 2013). As the supersaturation needed for them is different, each of the nucleation types show different metastability limits. The metastability limit for each type of nucleation is schematically represented in the diagram in Figure 2.4.

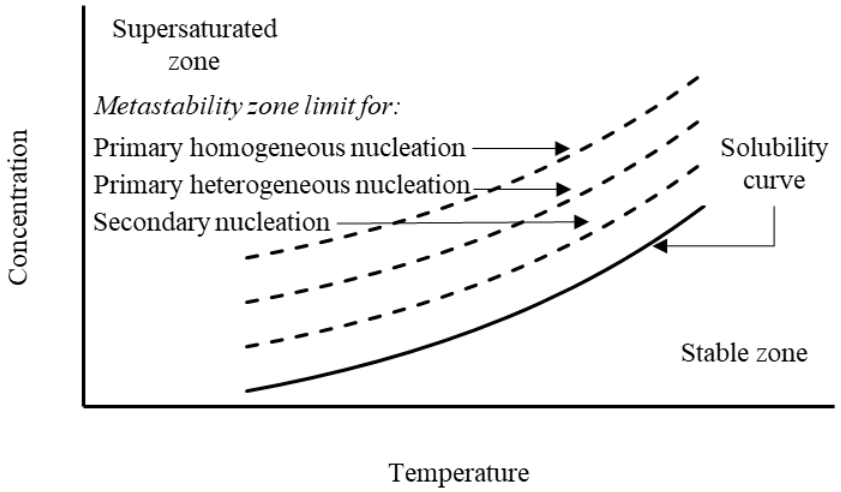

Figure 2.4: Saturation diagram, adapted from (Pastor, 2008).

In this thesis precipitating systems with relatively high saturation degree have been analysed. Therefore, only the effect of primary homogeneous nucleation has been considered in the PBM. However, all nucleation types are briefly described in the upcoming paragraphs.

Primary homogeneous nucleation is the spontaneous creation of small entities from the liquid phase in the absence of other solid bodies. It is uncertain how homogeneous nucleation happens, however, it is usually accepted that a sequence of bimolecular additions is the cause (Mullin, 2001). The number of molecules present in a nucleus is considered to be between ten and several thousand.

Due to the uncertainty associated with the mechanism, it is challenging to experimentally analyse the primary homogeneous nucleation and relating its rate to the effect of the experimental variables. One way of assessing the mechanism is by measuring the induction time. The induction time is considered to be inversely proportional to the nucleation rate (Hanhoun *et al*., 2013). Strictly, the induction time is the time elapsed between the generation of the supersaturation in the system and the appearance of the first nuclei, however, under controlled conditions it can be also related with the time lapse between the first stable pH is obtained and a change on it (Bhuiyan *et al*., 2008b; Mehta and Batstone, 2013). For struvite, the induction time decreases with an increasing saturation degree in the system (Bhuiyan *et al*., 2008a; Hanhoun *et al*., 2013; Mehta and Batstone, 2013; Ohlinger *et al*., 1999) and also with

an increasing shear rate, associated with a higher mixing intensity in stirred tanks (Bhuiyan *et al*., 2008a).

Regarding the kinetic rate of struvite primary homogeneous nucleation, its dependence with supersaturation is often represented with a power-law function where the exponent value varies (Burns *et al*., 2021; Galbraith *et al*., 2014). To the author's best knowledge the effect of mixing in struvite primary homogeneous kinetics has not been explicitly accounted yet. However, some authors have shown that primary homogeneous nucleation rate increases with an increasing shear rate for poly (1-butene) melt (Wolkowicz, 1978) or polypropylene (Tribout *et al*., 1996), which is in line with the decreasing induction times found for increasing shear rates in struvite precipitation systems.

Primary heterogeneous nucleation occurs when the nuclei are generated in the presence of a crystal phase that is not the one being analysed. The PBM developed in this thesis and the experiments performed did not consider the interaction of other crystals in the precipitation kinetics because that would increase the difficulty of identifying the individual effect of the supersaturation or mixing in the mechanisms. However, these interactions are relevant in real systems, where struvite precipitation might not be the only crystalline phase precipitating. In addition, there are commercial struvite recovery technologies as the Crystalactor® that use sand as seed material to precipitate struvite (Ewert *et al*., 2014). Furthermore, in precipitating systems that use alternative solid Mg sources as MgO or MgO by-products to recover struvite (Romero-Güiza *et al*., 2015a, 2015b, 2014; Stolzenburg *et al*., 2014), understanding how these solid Mg sources create the supersaturation in the system and afterwards the nucleation is performed is paramount for the design and operation of the technologies.

Secondary nucleation involves several nuclei generation processes where the crystal phase analysed is involved. Jones distinguished five different types of secondary nucleation (Jones, 2002): contact (with other crystals or the crystallizer parts), shear (due to fluid flow), fracture (due to particle impact), attrition (due to particle impact or fluid flow) and needle (due to particle disruption). Its effect has not been considered in the model presented in this thesis because the experiments performed were mainly unseeded and had a high saturation degree, which, as mentioned, favour primary homogeneous nucleation.

2.1.2.2. Growth

Once the nuclei stabilize, precipitation occurs through particle enlargement processes. Particle growth is the particle enlargement process where particles increase their size by consuming reactants.

It is believed that crystal growth occurs through two sequentially occurring main processes. First, mass transport of reactants happens from the bulk supersaturated solution to the particle-solution interface by diffusion. Second, the reactants are incorporated to the crystal lattice through the surface integration process (also called surface reaction process) (Myerson, 2001). The intensity of each process is proportional to the concentration difference of the reactants between the bulk and the particle-solution interface and between the particle-solution interface and equilibrium concentration respectively (Mullin, 2001). The mass change of each process can be defined as:

$$\frac{dm}{dt} = k_d \cdot A \cdot (c - c^*) \quad \textbf{2.9}$$

$$\frac{dm}{dt} = k_s \cdot A \cdot (c^* - c_e) \quad \textbf{2.10}$$

Where m is the mass of solid deposited in time t, k_d is a coefficient of mass transfer by diffusion, A is the surface area of the crystal, k_s is a rate constant for the surface integration process and c^* is the solute concentration in the particle-solution interface. c and c_e are the concentration of the compound in the bulk and its solubility, as aforementioned.

As the practical use of these equations is very limited due to the difficulty of determining the concentration at the particle-solution interface, the mass transfer from the liquid phase to the solid phase by crystal growth is generally assumed to depend on an 'overall' concentration driving force $(c - c_e)$ (Mullin, 2001) or other supersaturation expression that relates the concentration or activities of the ions in the bulk and equilibrium (see section 2.1.1.3).

The kinetic rate of struvite crystal growth is dependent on the available surface and the supersaturation (Burns *et al*., 2021). The effect of the area has been considered either dynamically (Burns *et al*., 2021) or proportional to the initial seed loading (Mehta and Batstone, 2013; Vaneeckhaute *et al*., 2018). When the growth is proportional to the area of the initial seed loading the kinetic rate usually includes a

ratio of the time dependent crystal mass present in the system to the mass of the initial loading of crystals.

Regarding mixing effects, growth rate dependency on the mixing is thought to be less important than for primary homogeneous nucleation (Tribout *et al.*, 1996; Wolkowicz, 1978). To the author's best knowledge there has not been any attempt to relate struvite growth kinetics with mixing intensity in a reactor. However, some authors have experimentally related the saturation decay in the system with the mixing intensity (Ariyanto *et al.*, 2014) or the obtained particle size with the mixer rotation speed (Fang *et al.*, 2016) or type (Ronteltap *et al.*, 2010).

Figure 2.5 illustrates the crystal growth of particles by showing two photomicrographs taken with a scanning electron microscopy at the beginning and the end of an experiment run for ten days in a fluidised bed reactor where struvite was precipitated.

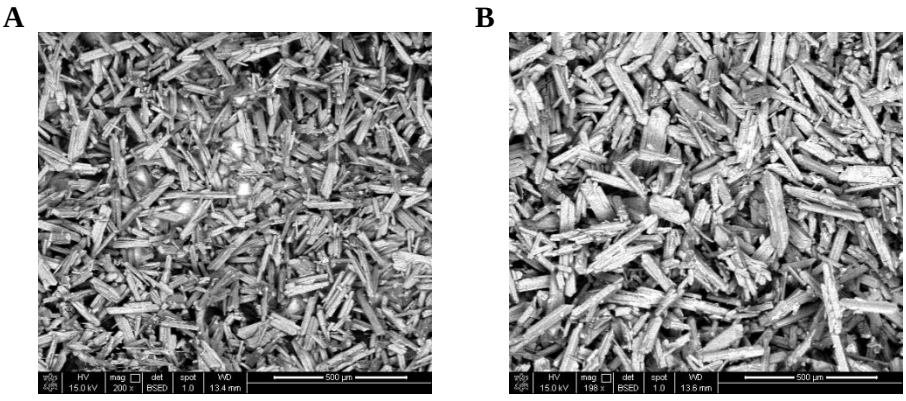

Figure 2.5: Struvite crystals sampled from an experiment conducted for 10 days in a fluidised bed reactor. (A) struvite crystals after 1 day, (B) struvite crystals after 10 days.

2.1.2.3. Aggregation

Aggregation is the particle enlargement process where the effective impact of two small crystals form a bigger one. Aggregation is relevant when a high concentration of small particles exist (Myerson, 2001). This is the case of fluidised bed reactors, where under certain conditions, the small particles generated through nucleation and growth mechanisms are accumulated in the reactor and their union changes the final PSD (Ye *et al.*, 2016). The fluidised bed reactors are relevant as commercial struvite recovery technologies as the Pearl™ technology by Ostara or Phosphogreen™ by

Suez use this type of reactors. Both technologies recover struvite as spherical particles. This spherical shape is a consequence of aggregation between particles and contact between the aggregated entities.

It is thought that some consumption of the dissolved ions is needed to create the bond between two colliding crystals (Liew *et al*., 2003). Therefore, the kinetic rate of aggregation is usually described as proportional to the supersaturation (Galbraith *et al*., 2014; Hounslow *et al*., 1988). Regarding the effect of the hydrodynamics, aggregation rate of calcium oxalate has been related with the energy dissipation rate or shear rate in the reactor (Zauner and Jones, 2000a). According to this contribution, the aggregation rate first increases and then decreases with an increasing energy input. This changing effect could be related with the idea that a higher energy input would favour the impact of the crystals, but when it is too high this impact would not be effective. To the author's best knowledge struvite aggregation rate has not been related with the system hydrodynamics. In relation to the effect of other components in the mechanism, the strength and size of the struvite aggregates can be limited by the presence of impurities (Shih *et al*., 2017).

Figure 2.6 shows how prismatic particles generated by nucleation and growth mechanisms form by aggregation a bigger spherical particle.

A **B**

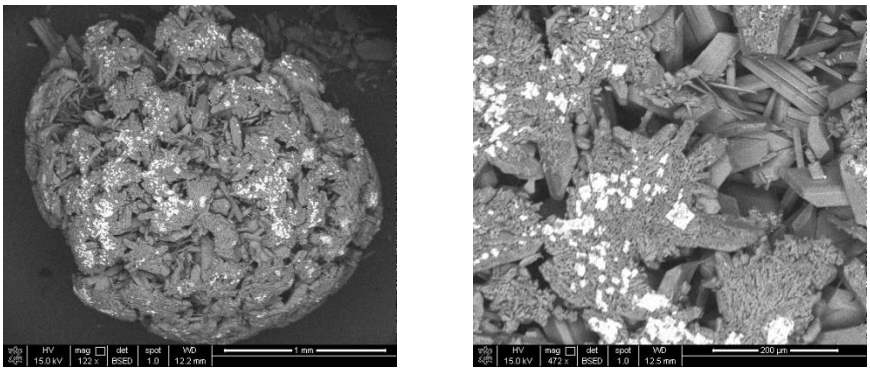

Figure 2.6: Struvite particles sampled from a seeded experiment conducted for 10 days in a fluidised bed reactor. (A) Sphere formed as a consequence of prismatic particle aggregation, (B) zoomed photomicrograph of the sphere.

2.2 PRECIPITATION PROCESS IN CONVENTIONAL WASTEWATER TREATMENT MODELLING

As mentioned in Chapter 1, historically, the main purpose of the wastewater industry has been to reduce the contamination before releasing the treated water to the receiving waterways. Consequently, the developed modelling frameworks have been focused on representing the organic matter and nutrient removal processes. The models developed with this objective are the ASM, comprised by ASM1, ASM2, ASM3 and ASM2d models. These models have been extensively used to describe WWTP unit processes, however, their use is very limited when it comes to precipitation or nutrient recovery description within a WRRF context. The ASM1 and ASM3 do not include precipitation-dissolution processes in the transformations, while the ASM2 model describes chemical phosphorus removal by precipitation with iron. This reaction is described as a one-step process, where the precipitated P is proportional to the concentration of dissolved P. Therefore, it ignores basic precipitation principles as solubility, supersaturation or the mechanisms governing the process. Moreover, ASM models do not allow the integration of nutrient recovery unit processes. This occurs because necessary physico-chemical components and transformations are not included in the model's definition (Vaneeckhaute *et al.*, 2018).

Fortunately, model libraries representing wastewater treatment have been upgraded and physico-chemical components and transformations have been combined with biochemical reactions in the PWM modelling frameworks developed over the last two decades. The PWM approaches are based on the compatible description of the transformations describing different unit processes in the WWTP. Despite they were originally conceived to combine classic water and sludge line models (Ekama *et al.*, 2006; Grau *et al.*, 2007; Jones and Tákacs, 2004; Rosen *et al.*, 2006), basics from which they were conceived (mass and charge continuity) allowed them for the straightforward implementation of chemical and physico-chemical processes. On this sense, based on the work by Koutsoukos *et al.* and Musvoto *et al.*, (Koutsoukos *et al.*, 1980; Musvoto *et al.*, 2000b, 2000a) several libraries have extended the initial approach by including the precipitation kinetics of the salts that can be formed in a WWTP. Some of them are the Biological nutrient removal model 2 (Barat *et al.*, 2013), the PWM developed by the University of Cape Town (Ikumi *et al.*, 2014b, 2014a), the Ceit's Physico-Chemical-PWM (PC-PWM) (Lizarralde *et al.*, 2015) or

the libraries developed by the collaboration of different research groups (Kazadi Mbamba *et al*., 2015a, 2015b; Solon *et al*., 2017, 2015).

These model libraries represent precipitation as a one-step process based on the supersaturation in the system and, in some cases, the crystal area or available growth sites. In addition, the Ceit's PC-PWM describes the precipitation by including some effect of the mechanisms, as the precipitation rate of the salts is proportional to activation terms that represent the growth of crystals under seeded and unseeded conditions (Lizarralde *et al*., 2015). However, the library does not include information about the obtained PSD. This issue has been partially solved in Nutrient recovery model (NRM) library (Vaneeckhaute *et al*., 2018), where the focus of the model is on the obtained fertilizer quality and quantity and an average particle diameter can be obtained in the simulations.

As the model developed in this thesis has been constructed following the equations and guidelines of the Ceit's PC-PWM, in this section, the approach will be described. In addition, the kinetics describing precipitation process in NRM library will be discussed as they include different precipitation mechanisms and the particle diameter of the obtained fertilizer.

2.2.1. Ceit's Physico-Chemical Plant Wide Model (PC-PWM)

Ceit's PWM is organised as a model library, where the user can select the set of transformations required to describe the unit processes constituting the WRRF that has to be simulated. Ceit's PC-PWM includes those transformations describing the solid-liquid and gas-liquid mass transfer phenomena.

Ceit's PWM was originally constructed combining models based on the ASM2d and ADM1 models (Grau *et al*., 2007) and over the years, the library has been extended by including models representing processes for anaerobic and aerobic sludge digestion (de Gracia *et al*., 2009), autothermal thermophilic aerobic digestion (Gomez *et al*., 2007), sludge ozonisation processes (Manterola *et al*., 2007) or recycle flow treatment technologies such as Sharon and Anammox (Grau *et al*., 2007). Furthermore, the dynamic heat transfer in multiphase biochemical reactors (Fernández-Arévalo *et al*., 2014) or the techno-economic assessment of the WRRF using cost models can also be simulated (Fernández-Arévalo *et al*., 2017a).

Due to these extensions, Ceit's PWM, like other PWM approaches gathers the most relevant biochemical, physico-chemical (liquid-gas transfer and precipitation-redissolution) and chemical equilibrium processes (acid-base reactions, ion pairing reactions, etc.) that can occur in a WRRF. These three types of processes are defined in the PC-PWM in two different modules according to their scope, nature of process being described and numerical solution.

The *first module* is constituted by slow processes and these will be described by means of ordinary differential equations (ODEs), defined as proposed in standard IWA models, with stoichiometry and kinetics formulation. This module accounts for biochemical, precipitation-redissolution and stripping-dissolution processes. The *second module* is a set of fast processes (assumed at equilibrium) described using implicit, nonlinear algebraic equations (AEs) that include chemical reactions required for describing the buffer capacity of the aqueous solution and consequently, the correct description of the weak acid-base chemistry (Ikumi *et al.*, 2014a; Lizarralde *et al.*, 2015; Solon *et al.*, 2015). The AEs system is solved at each simulation step using the proton balance approach. Both the mass balance and the proton balance can be described with the Tableau method (see Appendix A).

In the PC-PWM, the kinetic rate ρ_r of the precipitation reactions are defined as follows:

$$\rho_r = k_T \cdot \left(IAP^{1/\nu} - {K_{sp}}^{1/\nu}\right)^n \cdot (A_{SO} + A_{XTSS} + A_{SN}) \qquad \textbf{2.11}$$

where k_T is the kinetic precipitation/dissolution coefficient, A_{SO}, A_{XTSS} and A_{SN} are activator terms that change their value depending on the conditions in the system. A_{SO} and A_{XTSS} are indicators of the growth of crystals when there is material in the solution, while A_{SN} is used to simulate crystal growth when no seed material is added. For a generic salt, they are defined as follows:

$$A_{S0} = s_0 \frac{\left[A_z B_{y(s)}\right]}{\left[A_z B_{y(s)}\right]_0 + K_1} \qquad \textbf{2.12}$$

$$A_{XTSS} = \frac{Cw_{TSS}}{Cw_{TSS} + K_2} \qquad \textbf{2.13}$$

$$A_{SN} = \frac{[A^{y+}] \cdot [B^{z-}]}{[A^{y+}] \cdot [B^{z-}] + K_3} \qquad \textbf{2.14}$$

where s_0 is a dimensionless parameter that represents growth of the available surface assuming a constant size distribution, Cw_{TSS} is the concentration of total suspended solids and K_1, K_2 and K_3 are constants with a very low value to guarantee numerical stability.

If an unseeded experiment is being simulated, precipitation through A_{SN} path will be dominant. However, as crystals start to grow, A_{SO} will become the dominant path. These activation terms help to quantify the effect of nucleation and growth process on the kinetic rate of precipitation. However, for design and optimization purposes the PSD is a key variable and its modelling is not considered in this approach.

Therefore, even if chemical and physico-chemical processes are considered in the PC-PWM developed by Ceit, the model is limited when it comes to accurately represent the precipitation mechanisms. However, the fact that all components are expressed using their elemental mass composition, makes Ceit's PC-PWM a very suitable framework to attempt the incorporation of a PBM within a PWM modelling context. This would allow the model to represent struvite precipitation in a more rigorous way for design and optimization purposes while making it compatible with the modelling of other unit processes needed to simulate the whole WRRF.

2.2.2. Nutrient Recovery Model (NRM) library

Developed by Vaneeckhaute *et al.*, (Vaneeckhaute *et al.*, 2018) it is a model tool focused on the quantity and quality of recovered products in WRRFs. The library includes dynamic physico-chemical three-phase models. In this section, the focus will be on how the liquid-solid mass transfer process is described in the library.

The kinetic rate for liquid-solid mass transfer is described as:

$$\rho_R = k_T \cdot (S_r - 1)^n \qquad \textbf{2.15}$$

Where ρ_R is the kinetic rate of precipitation/dissolution of a component, k_T is the kinetic precipitation/dissolution coefficient, S_r is the saturation ratio, described as $S_r = \left(\frac{IAP}{K_{sp}}\right)^{1/\nu}$ and n is the reaction order.

The value of the supersaturation changes dynamically as precipitation occurs in the system. Additionally, the model chooses the dominant precipitation mechanism occurring in the system depending on the reactor's operational condition. The model

considers four possibilities, depending on the supersaturation, presence of seed material and presence of crystals. Depending on these variables, the model selects a definition of k_T and a value of n to define the precipitation kinetic.

The first condition considers a situation where the system is under supersaturation condition ($S_r > 1$) and there is seed material in the solution. In that case, it is assumed that crystal growth dominates the precipitation and k_T is then described as:

$$k_T = k_{G,T} \cdot a_{seed} \cdot \frac{M_{seed}}{V_{liq}} \qquad \textbf{2.16}$$

Where $k_{G,T}$ is the temperature dependent growth rate coefficient, a_{seed} is the specific area of surface per gram of seed before the seed crystals start to grow and M_{seed} is the time-dependent mass of seed material in the reactor, calculated at every time step. The value of n is 2.

The second condition considers a situation where there is supersaturation in the system ($S_r > 1$) but there is not seed material present in the solution and/or the crystal size is not large enough to have an influence in the process. In this case, it is believed that the system is under nucleation conditions and k_T is then described as $k_T = k_{B,T}$, where $k_{B,T}$ is the nucleation rate and the value of n is bigger than 2 and should be estimated experimentally for each precipitate.

The third condition is an undersaturated ($S_r < 1$) solution with a presence of precipitate in the system. In this case, $k_T = k_{D,T}$ where $k_{D,T}$ is the dissolution rate and n has a different value. The numeric value of the constants is not specified but the model allows the dissolution of the crystal.

The fourth condition is the equilibrium condition ($S_r = 1$). The model considers that under equilibrium conditions, there is no change in the precipitation system. Thus, k_T becomes 0 and both precipitation and re-dissolution are inhibited.

In addition, the model defines aggregation and floc break-up kinetics by considering the effect of mixing and the particle number.

From the crystal mass precipitating and considering each crystal phase density, the model is able to dynamically calculate the average particle size of the precipitated fertilizer, considering that the particles are spherical and that the number of particles is known:

$$d_P = \sqrt[3]{\frac{V_{fert}}{N_{part} \cdot \frac{\pi}{6}}} \quad \textbf{2.17}$$

Where V_{fert} is the fertilizer volume, N_{part} is the particle number and $\frac{\pi}{6}$ is the particle shape factor.

The model presented by Vaneeckhaute *et al.* is an improvement in wastewater treatment because it changes the focus towards the recovered product quality while maintaining an overall view of the WRRF.

However, the model presents some limitations when detailed modelling of the precipitation process is needed, as it does not consider PSD. In addition, even if the model includes different scenarios where the main mechanisms are of relevance, it is not clear how the mass balance is fulfilled when they are combined, as some of them are defined in particle number and others in mass.

Therefore, it is clear that despite the recent improvements towards representing precipitation processes in wastewater treatment industry, still there is a need to upgrade the existing models with new frameworks that account main mechanisms of the precipitation and a dynamic change of the PSD while maintaining the mass and charge balance.

2.3 POPULATION BALANCE MODEL (PBM)

As opposed to the one step precipitation models commonly used in conventional wastewater modelling to represent precipitation process, the PBM explicitly includes the definition of the mechanisms and tracks changes in the PSD of the system.

First formulated in 1964 by Hulburt and Katz (1964), the PBM is a well stablished tool to simulate particulate systems (Costa *et al.*, 2007). Despite it has not been extensively used in wastewater industry, it is an accepted tool in other fields as the industrial crystallization, where it has been used since the 1970s (Nagy *et al.*, 2013). Furthermore, it can be used to describe polymerization, bubble towers, aerosol reactors, biological processes, fermentation or cell culture (Costa *et al.*, 2007).

Due to the topic of this thesis, the focus in this section will be on the use of PBMs to represent struvite precipitation processes. However, the model framework can be applied in other processes occurring in a WRRF, as flocculation (Nopens *et al.*,

2004), bubble dynamics (Climent *et al*., 2019), granulation (Abrahamsson *et al*., 2018) or crystallization (Ye *et al*., 2018), among others (Nopens *et al*., 2015).

The main advantage of the PBM when compared to one step kinetic models often used in the wastewater treatment modelling is that the PBM simulates the distribution of certain properties (e.g. size, composition) within a group of individual entities (e.g. particles, bubbles or cells) (Nopens *et al*., 2015). This is done by explicitly accounting the interaction of these entities with their environment (e.g. particles growing or dissolving) and between them (e.g. aggregation or coalescence) by defining the mechanisms of the process. The consequence is that the PBM can account the difference in the behaviour of the entities in the system based on the distribution of the properties considered. This is a clear improvement when detailed modelling of the process is needed, as the conventional approach used in wastewater modelling only considers non distributed (or 'averaged') scalar properties (e.g. single particle or bubble size). Another advantage is that due to its higher detail, the PBM can help in the understanding of the process under study.

2.3.1. Definition

The main equation of the PBM for a precipitation batch experiment can be expressed as (Galbraith, 2011):

$$\frac{\partial n_D}{\partial t} + G\frac{\partial n_D}{\partial L} = B(L) - D(L) \qquad \textbf{2.18}$$

Where n_D is the population density, L is the characteristic crystal length (the distributed property), G is the size independent linear growth rate, B is the birth function and D the death function.

The population density n_D defines the number of particles per volume unit (N_D) within the size range L→ L + dL:

$$n_D(L) = \frac{dN_D}{dL} \qquad \textbf{2.19}$$

the first term of the left of equation 2.18, $\frac{\partial n_D}{\partial t}$, is an accumulation term. The term $G\frac{\partial n_D}{\partial L}$ accounts for the change in the distribution dynamics of the property (crystal length) by a continuous process (crystal growth), while the birth and death functions

consider the change due to discrete processes (aggregation or breakage) and account the rate at which particles of size L are formed (birth) and are removed (death).

The analytical resolution for the PBM is only possible for the simplest cases, consequently, numerical methods, often involving some kind of discretization or decomposition of the main equation, are used for its resolution (Costa *et al.*, 2007).

2.3.2. Population balance model for struvite recovery

Due to the advantages of the PBM over conventional modelling of precipitation in wastewater, several authors have successfully implemented the PBM framework to simulate struvite precipitation (Burns *et al.*, 2021, 2016; Galbraith *et al.*, 2014; Hanhoun *et al.*, 2013; Triger *et al.*, 2012; Ye *et al.*, 2018). However, as mentioned above, the analytical resolution for the PBM is only possible for the simplest cases. As these simple cases are often far from the conditions of a real reactor, in the available contributions in the literature each author had to make assumptions and solve the PBM following different numerical approaches. For example, in the aforementioned contributions, discretization (Burns *et al.*, 2021, 2016; Galbraith *et al.*, 2014; Triger *et al.*, 2012), the method of moments (Hanhoun *et al.*, 2013) or the quadrature method of moments (Ye *et al.*, 2018) have been used to solve the PBM. The resolution method used and the fact that all the contributions are based on particle populations can hinder the combination of the PBMs with the existing wastewater treatment libraries.

The compatibility of the different modelling approaches is necessary in order to use the PBM within a WRRF context, where the performance of the precipitation reactor depends on the operation of the rest of the plant. The model presented in the Chapter 3 of this thesis overcomes this barrier by defining mass-based components.

2.3.3. Mechanisms of precipitation in the PBM

The mechanisms of precipitation are explicitly included in a PBM. In this section, their definition in the existing contributions to represent struvite precipitation is going to be discussed.

2.3.3.1. Nucleation

Nucleation kinetics are often presented as a function of the supersaturation in the system. The expressions used by some relevant works on the field of struvite simulation using PBM are included in Table 2.1.

Table 2.1: Compilation of nucleation kinetic rate expressions for struvite by authors using the PBM framework. B_0 is the nucleation rate, K_B is the nucleation constant, n_B is the Nucleation exponent, B_C is a constant value, ΔG_{hom}^{crit} is the free enthalpy of activation, k_{Bol} is the Boltzmann constant and T is temperature.

$B_0\left(\frac{\text{nuclei}}{\text{l}\cdot\text{min}}\right)$	$K_B\left(\frac{\text{nuclei}}{\text{l}\cdot\text{min}}\right)$	$n_B(-)$ or $B_C(-)$	Authors
$B_0 = K_B \cdot SI^{n_B}$	$8.509 \cdot 10^7$	$n_B = 1.68$	(Galbraith *et al.*, 2014)
$B_0 = K_B \cdot SI^{n_B}$	$7.509 \cdot 10^7$	$n_B = 1.68$	(Burns *et al.*, 2021)
$B_0 = K_B \cdot \exp\left(\frac{-\Delta G_{hom}^{crit}}{k_{Bol}\cdot T}\right)$	$2.04 - 4.02 \cdot 10^8$	--	(Triger *et al.*, 2012)
$B_0 = K_B \cdot \exp\left(\frac{-B_C}{\ln {S_r}^2}\right)$	$2.39 \cdot 10^{11}$	$B_C = 449$	(Hanhoun *et al.*, 2013)

Galbraith *et al.* (2014) and Burns *et al.* (2021) use a power law function where the primary homogeneous nucleation rate has an exponent of 1.68. The exponent value is relatively low if compared with classic precipitation theories, which state that the exponent of primary homogeneous nucleation is often higher (Myerson, 2001). Despite the regressed kinetic constant K_B value is different, it shows a relatively good agreement between the two contributions. Triger *et al.* (2012) and Hanhoun *et al.* (2013) used different expressions to represent nucleation and also different ways of assessing supersaturation. This increases the difficulty to compare results between different contributions.

2.3.3.2. Growth

All the contributions reviewed used a size independent growth rate defined as a power law function. The exponent and kinetic constant regressed are included in Table 2.2.

Table 2.2: Compilation of growth kinetic rate expressions for struvite by authors using the PBM framework. G is the linear growth rate, K_G is the Growth constant and n_G is the Growth exponent.

$G\ \left(\frac{\mu m}{min}\right)$	$K_G\left(\frac{\mu m}{min}\right)$	n_G (-)	Authors
$G = K_G \cdot SI^{n_G}$	$K_G = 12.49$	$n_G = 5.269$	(Galbraith *et al.*, 2014)
$G = K_G \cdot SI^{n_G}$	$K_G = 16.72$	$n_G = 2$	(Burns *et al.*, 2021)
$G = K_G \cdot SI^{n_G}$	$K_G = 90 - 120$	$n_G = 1.15 - 2$	(Triger *et al.*, 2012)
$G = K_G \cdot {S_a}^{n_G}$	$K_G = 300.7$	$n_G = 1.34$	(Hanhoun *et al.*, 2013)

As it can be seen, the values of the regressed constants and the saturation expressions vary between the different contributions.

Regarding growth kinetic expressions, despite they are not commonly used in struvite precipitation, some authors have proposed kinetics where the crystal growth is not independent of the size of the particles. Nagy and Aamir collected some of these expressions and they are shown in Table 2.3 (Nagy and Aamir, 2012). The expressions use the SI for simplicity, but any other form of supersaturation could be used.

Table 2.3: Growth kinetic expressions, where L is the characteristic length, $\boldsymbol{\alpha_{GC}}$ is the size dependency growth constant and $\boldsymbol{n_{GC}}$ is an exponent (Nagy and Aamir, 2012).

Growth Expression	Validity Condition
$G = K_G \cdot SI^{n_G} \cdot (1 + \alpha_{GC} \cdot L)^{n_{GC}}$	$(\alpha_{GC} \neq 0, n_{GC} \neq 1)$
$G = K_G \cdot SI^{n_G}$	$(\alpha_{GC} = 0, n_{GC} = 1)$
$G = K_G \cdot SI^{n_G} \cdot (1 + \alpha_{GC} \cdot L)$	$(\alpha_{GC} \neq 0, n_{GC} = 1)$
$G = K_G \cdot SI^{n_G} \cdot L^{n_{GC}}$	$(n_{GC} \neq 1)$

2.3.3.3. Aggregation

In the field of struvite precipitation modelling through PBM framework, aggregation is not always considered. Despite Galbraith *et al.* (2014) considered its effect by defining the kinetics of the mechanism proportional to the SI in the system, most of the authors have avoided its inclusion in the PBM framework (Burns *et al.*, 2021;

Hanhoun *et al*., 2013; Triger *et al.*, 2012; Ye *et al*., 2018). This assumption is made because under some experimental conditions, aggregation may not be relevant. In addition, if the method of moments is used for the resolution of the PBM, aggregation cannot be considered. Considering that experimental evidence show that aggregation can affect the PSD in the system, especially in seeded and continuous experiments, which are the most similar conditions to a real reactor, it seems necessary to have the possibility to include this mechanism in the chosen modelling approach.

Galbraith *et al.* (2014) used a size independent aggregation kernel, which is the one that provides best simulation outputs when compared to the experimental data (Bramley *et al.*, 1996). As the resolution method used in Galbraith *et al.* is the discretization, Hounslow's approach is used to model the aggregation process (Hounslow *et al.*, 1988). This approach is explained in the Chapter 3 of the thesis.

2.3.4. Mixing effects consideration in the PBM

In struvite precipitation modelling, mixing is not usually contemplated. According to Pohorecki and Bałdyga (1983), however, the rate of precipitation and the size distribution of the obtained particles depend significantly on the mixing intensity. Therefore, ignoring mixing effects could be one of the reasons behind the shifting parameter values found in the PBMs describing precipitation of struvite, as they could have been obtained for different mixing intensities.

Considering the effect of mixing in precipitation processes is challenging, since it occurs at different process scales: macromixing describes mixing at reactor scale, micromixing considers mixing in the smallest vortices and the ultimate molecular diffusion, while mesomixing lies between micromixing and macromixing (Torbacke and Rasmuson, 2004).

In this regard, it is believed that the rate of mixing could be evaluated by means of micromixing models (Pohorecki and Bałdyga, 1983). As nucleation and growth occur at molecular scale, micromixing impacts directly both mechanisms, while mixing at bigger scales only affects indirectly the process by determining the micromixing environment (Phillips *et al*., 1999). Consequently, interaction between the micromixing and the kinetics of both mechanisms (especially nucleation) have been evaluated in several contributions (Baldyga *et al*., 1995; Baldyga and Bourne, 1992; Marcant and David, 1991; Phillips *et al.*, 1999). In these contributions the

mixing is considered inhomogeneous in the reactor and the precipitation model changes depending on this inhomogeneity.

Micromixing in the aforementioned contributions has been characterized as a function of the energy dissipation rate. In experimental studies, the effect of mixing on the different mechanisms has been often quantified using the shear rate (De Santis *et al*., 2016; Forsyth *et al*., 2016; Mullin and Raven, 1962; Nappo *et al*., 2018). The specific energy dissipation rate and the average shear rate in a stirred tank are related as follows (Sánchez Pérez *et al*., 2006):

$$\frac{P_i}{V} = \tau \cdot \gamma \qquad \textbf{2.20}$$

where P_i is the power input, V is the volume of the liquid in the reactor, τ is the shear stress and γ is the shear rate. For Newtonian fluids, the dynamic viscosity is the ratio of shear stress and shear rate:

$$\mu = \frac{\tau}{\gamma} \qquad \textbf{2.21}$$

therefore, eq 2.20 can be written as:

$$\gamma = \left(\frac{P_i}{V \cdot \mu}\right)^{1/2} \qquad \textbf{2.22}$$

Eq. 2.22 has been often used to quantify the average shear rate in a stirred vessel (Ilievski *et al.*, 2001; Nappo *et al*., 2018; Sánchez Pérez *et al.*, 2006).

The models combining micromixing effect with nucleation and growth kinetics have not been implemented for struvite precipitation. Regarding aggregation, Vaneeckhaute *et al.* propose that the aggregation of crystal fertilizers obtained in WRRFs can depend on the average shear rate, based on a spherical particle model for macroscale flocculation (Vaneeckhaute *et al*., 2018). In addition, the use of other frameworks as CFD to simulate mixing effects in wastewater treatment is increasing. In this regard, Ye *et al.* (2018) coupled the PBM framework with CFD to represent struvite nucleation and growth in a fluidised bed reactor. Nevertheless, the kinetic rates of nucleation and growth used in Ye *et al.* (2018) did not explicitly account the micromixing effect as they were taken from previous contributions by Galbraith *et al.* (2014) and Hanhoun *et al.*(2013).

Regarding growth in other compounds, Samad *et al.* (2011) proposed kinetic rates for size independent and size dependent growth of crystals where the stirring speed was included as a power law function. However, the expression is limited in its application as the stirring speed is not the only factor affecting mixing intensity in a reactor (stirrer type and size and liquid volume in the reactor should be also considered, at least).

For aggregation, similar approaches as the one proposed in Vaneeckhaute *et al.* (2018) have been used before for other compounds (Hounslow *et al*., 2013). In addition, Samad *et al.* proposed a kinetic rate where the aggregation depends on the stirring speed (Samad *et al.*, 2011).

2.4 SUMMARY

Precipitation process depends on supersaturation and occurs through various mechanisms. These mechanisms occur simultaneously in a precipitation reactor and depending on them the PSD in the system evolves differently. Despite precipitation has been used for years for product separation and purification, its interest and application in wastewater industry has been low. Therefore, main modelling frameworks in wastewater industry included precipitation in a very simplistic way. Due to the current interest in product recovery from WRRF, the interest in physico-chemical modelling has increased. A modelling framework that could improve existing modelling is the PBM. The PBM considers the mechanisms of precipitation and tracks the PSD within the reactor. Despite some efforts have been made to represent struvite precipitation using the PBM approach, there is still the need to improve in the compatibility of the PBM with the existing conventional frameworks. In addition, the great variability of the parameter values and the fact that mixing effect in the process is often ignored, encourages the research for rigorous calibration and consideration of such effects.

CHAPTER 3

A NEW MASS-BASED DISCRETIZED POPULATION BALANCE MODEL FOR PRECIPITATION PROCESSES: APPLICATION TO STRUVITE PRECIPITATION

This chapter has been redrafted from:

Elduayen-Echave B., Lizarralde I., Larraona G. S., Ayesa E., Grau P., 2019. A new mass-based discretized Population Balance Model for precipitation processes: application to struvite precipitation. Water Research, 155, 26-41.

3.1 ABSTRACT

Mathematical models describing precipitation processes in one step need to be upgraded. PSD is a crucial variable and its inclusion in the modelling libraries is necessary if the technology wants to be optimized through simulation. With this objective, a mass-based PBM is presented in this chapter. The model has been

constructed using a stoichiometric matrix and a kinetic vector and using mass as the internal coordinate, as it is usually done in wastewater treatment modelling. Identifiability of the parameters of the model was evaluated using a sensitivity and a collinearity analysis for six simulation case studies of struvite precipitation. In addition, the model's predictive capacity to represent experimental data obtained from two batch experiments performed in the laboratory was tested. The results of the analysis showed that the identifiability of the parameters depends on the available experimental data and explored scenarios. Lack of identifiability in the parameters could be the reason behind the shifting parameter values describing mechanisms of precipitation in the literature. This chapter helps to understand the possibilities and limitations that the PBM approach offer.

3.2 BACKGROUND

Available struvite recovery technologies show significant differences in their operation depending on the characteristics of the product to be recovered and the process restrictions (continuous versus batch, different hydraulic retention times, etc.) (Tarragó *et al*., 2016). The operation of the reactor and the weight of each mechanism (primary nucleation and secondary nucleation, growth, aggregation, attrition and breakage of particles) will determine the PSD in the reactor. As the performance of struvite as a fertilizer depends on the obtained PSD (Tarragó *et al.*, 2016), this is a very important aspect of the process.

Mathematical modelling and simulation libraries for WRRFs include main precipitation processes occurring in the recovery facilities (Ikumi *et al*., 2014a; Lizarralde *et al.*, 2015; Solon *et al.*, 2017). These modelling approaches can predict the amount of obtained solid in a recovery reactor, based on the kinetics of precipitation and thermodynamics. In addition, these modelling and simulation libraries often combine information from the biological, chemical and physico-chemical processes in the WRRF with its economic performance. This is a necessary information to assess the suitability of installing a recovery technology by evaluating its effect on the global WRRF behaviour. However, they usually do not include information on the precipitation mechanisms nor the PSD. Therefore, they should be upgraded with new modelling frameworks for wastewater treatment modelling as the PBM if they are going to be used for design and optimization of struvite recovery technologies.

As explained in Chapter 2 (section 2.3.2), the PBM has been proved to be successful to track changes in the PSD in the struvite precipitation already (Galbraith *et al*., 2014; Hanhoun *et al*., 2013; Triger *et al*., 2012). Modelled PSD and reactants consumption show good agreement between the experimental data and model results. This evidences the great potential of the PBM for the correct prediction of the process and its optimization. However, as pointed out in Chapter 1, there are some aspects regarding PBM construction in the existing contributions that should be addressed. In this chapter, two of them are considered.

Firstly, PBM models have generally been defined using number of particles as the dependent variable of the process, which is coherent with the model purposes, but, can lead to mass discontinuities (Hounslow *et al*., 1988). Although partially solved (Galbraith *et al*., 2014), this problem would make them incompatible with conventional models used in the wastewater treatment framework, which are mainly constructed on the basis of mass balances around the unit to be described (IWA ASM-ADM models) (Batstone *et al*., 2002; Henze *et al*., 2000). For a successful implementation of PBMs in wastewater treatment industry, mass discontinuity must be avoided first. Using mass as internal coordinate automatically satisfies the mass balance (Scarlett, 2002). In addition, if the PBM is discretized, the rate of change of mass in the bins of different sizes and the components in the system can be represented as a dynamic mass balance, as it is usually done in standardized methodology for wastewater treatment modelling. The mass-based approach has been used to describe comminution, sintering or granulation processes (Verkoeijen *et al*., 2002). However, those examples did not include the mechanisms of primary homogeneous nucleation and particle growth, which are necessary to describe the mass transfer occurring from the liquid phase to the solid phase. Moreover, the aggregation was defined for constricted-in-space aggregation (Sastry and Fuerstenau, 1970) and a linearly partitioned size domain (Verkoeijen *et al*., 2002). Those considerations are not valid for a precipitation process where the solid concentration is small and a big range of sizes needs to be covered.

The second aspect is that obtained parameter values for the parameters defining inner mechanisms of the precipitation of struvite are very variable in the literature (Galbraith *et al*., 2014; Hanhoun *et al*., 2013; Mehta and Batstone, 2013). The same happens for other compounds, too (Chen *et al*., 2002; Ruan *et al*., 2016). Mechanisms occur simultaneously and obtaining meaningful experimental data to attribute to each mechanism its real effect on the precipitation is difficult, making calibration a very

challenging issue. In addition, each author considers different model assumptions, which has a direct effect on the calibrated parameter values. For example, some authors did not include aggregation in the mechanisms of precipitation (Hanhoun *et al.*, 2013; Triger *et al.*, 2012), leaving growth as the only particle enlargement process in their model. This will inevitably lead to different parameter values comparing to the authors that include aggregation, even for the same experimental conditions and sampling method. In addition, many definitions for the kernels of the mechanisms have been used in the literature, especially for aggregation and breakage (Hill and Ng, 2002), which leads again to different parameter values. Moreover, the considered thermodynamic equilibrium rates, the use of activity coefficients and the way they are obtained are other important reasons for these differences. Election of the constants governing these equilibrium equations has a considerable effect on the predicted precipitation potential (Barnes and Bowers, 2017). Using mathematical analysis tools to evaluate the possibility of obtaining trustworthy parameter values will increase the confidence in the modelling framework.

Therefore, the first objective of this chapter is to present a PBM scheme based on a mass balance approach where the mass is conserved and it is compatible with wastewater treatment models conventionally used. For this issue, the PBM was adapted to a conventional model structure in wastewater treatment modelling, where mass of the crystal entities is used as the internal variable, instead of particle number. The second objective is to evaluate the theoretical parameter identifiability of the constructed model using model analysis tools as sensitivity analysis and a collinearity analysis. This evaluation is helpful to understand the goodness of the modelling framework before any calibration procedure is followed. To conclude the chapter, model parameters were adjusted heuristically to reproduce experimental data obtained in two laboratory tests, as a preliminary illustration of the predictive capacity of the model, which will be further assessed in the fifth chapter of the thesis.

3.3 MATERIALS AND METHODS

In this section, the information is divided in three subsections. In subsection 3.3.1 a description of the presented model is given, in subsection 3.3.2 the methodology followed to implement the analysis tools used to assess the identifiability of the parameters is detailed and in subsection 3.3.3 the experimental procedure followed to show the predicting capacity of the model is described.

3.3.1. Precipitation model

The model presented here describes the precipitation process of struvite. The main reaction for this process is:

$$Mg^{2+} + NH_4^+ + PO_4^{3-} + 6H_2O \rightarrow MgNH_4PO_4 \cdot 6H_2O \downarrow \quad \textbf{3.1}$$

the liquid-solid mass transfer process occurring in the reactor is defined by the PBM approach, described below.

3.3.1.1. Population balance model

As mentioned in section 2.3, the main equation of the PBM for a precipitation batch experiment can be expressed as (Galbraith, 2011):

$$\frac{\partial n_D}{\partial t} + G\frac{\partial n_D}{\partial L} = B(L) - D(L) \quad \textbf{3.2}$$

The mathematical model presented in this chapter is a discretized population balance model (DPBM). In a DPBM, the particle sizes are considered bins defined after the crystal size range is partitioned. For the resolution of the PBM a dynamic balance is applied to each bin.

In this thesis, particle sizes are defined after partitioning the crystal size range in 30 bins. Each of the bins corresponds to spherical particles sized between 0.001 and 0.812 mm of radius. The volume size defined for each bin is twice the previous one, using a 2 geometric progression for the partition of the volume size domain. As a consequence, PSD in the model follows a true discretization where only particles of size v, 2v, 4v, etc. exist, being v the volume of the smallest spherical particle size considered.

The difference between the DPBM presented in this chapter and most of the PBMs available in literature is the way in which particle-particle and particle-liquid interactions are defined. In this thesis mass is used as the internal coordinate, instead of using particle number. Each particle size bin is considered as a component in the model and its interaction with other components (ions in the liquid and/or other solid bins) is described by the precipitation mechanisms and is based on the mass continuity of the components. The ions considered are those employed in urban wastewater treatment models. They have been defined using common wastewater

equilibrium reactions, as ion pairing and acid-base reactions, following guidelines and equations proposed in Lizarralde *et al*. (2015) and showed in Table 3.1.

Table 3.1: Equilibriums and constant values.

Equilibrium	Equilibrium Constant	Constant Value
$H_2PO_4^- \leftrightarrow HPO_4^{2-} + H^+$	$K_{H_2PO_4^-} = \frac{a_{H_2PO_4^-}}{a_{HPO_4^{2-}} \cdot a_{H^+}}$	$10^{-7.198}$
$HPO_4^{2-} \leftrightarrow PO_4^{3-} + H^+$	$K_{HPO_4^{2-}} = \frac{a_{HPO_4^{2-}}}{a_{PO_4^{3-}} \cdot a_{H^+}}$	$10^{-12.375}$
$MgH_2PO_4^+ \leftrightarrow H_2PO_4^- + Mg^{2+}$	$K_{MgH_2PO_4^+} = \frac{a_{MgH_2PO_4^+}}{a_{H_2PO_4^-} \cdot a_{Mg^{2+}}}$	$10^{-40.8291}$
$MgHPO_4 \leftrightarrow HPO_4^{2-} + Mg^{2+}$	$K_{MgHPO_4} = \frac{a_{MgHPO_4}}{a_{HPO_4^{2-}} \cdot a_{Mg^{2+}}}$	$10^{-15.175}$
$MgPO_4^- \leftrightarrow PO_4^{3-} + Mg^{2+}$	$K_{MgPO_4^-} = \frac{a_{MgPO_4^-}}{a_{PO_4^{3-}} \cdot a_{Mg^{2+}}}$	$10^{-4.654}$
$MgOH^+ \leftrightarrow PO_4^{3-} + OH^-$	$K_{MgOH^+} = \frac{a_{MgOH^+}}{a_{Mg^{2+}} \cdot a_{OH^-}}$	$10^{11.397}$
$NH_4^+ \leftrightarrow NH_3 + H^+$	$K_{NH_4^+} = \frac{a_{NH_4^+}}{a_{NH_3} \cdot a_{H^+}}$	$10^{-9.244}$
$H_2O \leftrightarrow OH^- + H^+$	$K_W = a_{OH^-} \cdot a_{H^+}$	$10^{-13.997}$

The mechanisms of precipitation in this contribution (primary homogeneous nucleation, particle growth and aggregation of particles) are defined using a Petersen matrix for the stoichiometry and a vector of kinetics.

The kinetics of mechanisms are defined in a general way as power-law functions dependent on SI and kinetic constants and exponents.

$$\rho_R = K_R SI^{n_R} \qquad \textbf{3.3}$$

where ρ_R is the rate of change of the mechanism, K_R is the kinetic constant of the considered mechanism and n_R is the exponent (-). Units of ρ_R and K_R depend on the mechanism.

The SI is calculated in every time step using the IAP of the species conforming the struvite and the solubility product of the salt.

$$SI = \log\left(\frac{a_{Mg^{2+}} \cdot a_{NH_4^+} \cdot a_{PO_4^{3-}}}{Ksp_{Stru}}\right) \quad \textbf{3.4}$$

where a_i is the activity of ion i (mol/l) and Ksp_{Stru} is the solubility product of the salt. Many values for the solubility product have been reported in the literature (Doyle and Parsons, 2002; Rahaman *et al*., 2006). From the proposed values, Ksp_{Stru}= $7.58 \cdot 10^{-13}$ $(mol/l)^3$ was used for all the simulations in this thesis.

As the PBM is mass-based, the model could be further extended with other reactions as: liquid-gas transfer, other salts precipitation or other chemical reactions in a systematic and simple way in order to simulate struvite or other salt precipitation process in a reactor operated with real wastewater. Mechanisms not considered in the PBM presented in this chapter, such as breakage or secondary nucleation, could be added too. However, this model accounts for the most important mechanisms, maintaining a good compromise between relatively simple implementation and realistic representation of occurring precipitation. In the next subsections how the implementation of each mechanism has been done in the model is described in detail.

3.3.1.2. Nucleation

As explained in Chapter 2, primary homogeneous nucleation is the spontaneous creation of small entities from the liquid phase in the absence of other solid bodies. These entities are in the edge of liquid and solid phase, some of them re-dissolve into liquid and others become the starting point of the precipitation. It is uncertain how primary homogeneous nucleation happens, however, it is usually accepted that a sequence of bimolecular additions is the cause (Mullin, 2001). The number of molecules present in a nucleus is considered to be between ten and several thousand. This size range is considerably smaller than the minimum size measurable with typically available equipment and, as a consequence, the ones considered in the PBMs in the literature. In this thesis, the radius (r) of this smallest size has been arbitrarily chosen as r = 0.001 mm, following the example of Galbraith *et al.* (2014). The nucleation rate should be understood as the appearance rate of particles of the smallest size considered in the model. This appearance is subjected in reality to nucleation and particle enlargement processes. The assumption is considered valid

as particles smaller than r = 0.001 mm have a very small effect on the obtained crystal mass.

The created crystal mass of size r = 0.001 mm is proportional to the reactants consumption as defined in the stoichiometry. This appearance rate is defined as:

$$B_0 = K_B \cdot SI^{n_B} \cdot V \qquad \textbf{3.5}$$

where B_0 is the particle birth rate due to primary homogeneous nucleation (nuclei/day), K_B is the kinetic constant of the primary homogeneous nucleation (nuclei/(day·m^3)), V is the liquid volume in the reactor (m^3) and n_B is the Nucleation Exponent (-).

Mass change in the smallest sized bin due to nucleation is:

$$\frac{\partial X_1}{\partial t} = K_B \cdot SI^{n_B} \cdot V \cdot mesf_1 \qquad \textbf{3.6}$$

where X_1 (g) is the mass of struvite characterized as the smallest size at any time and $mesf_1$ (g) is the mass of struvite in a single sphere of the smallest bin (constant value). Table 3.2 includes the stoichiometry matrix for primary homogeneous nucleation process.

3.3.1.3. Crystal Growth

Once the nuclei stabilize, precipitation occurs through particle enlargement processes: particle growth and aggregation. Particle growth is the particle enlargement process where particles increase their size by consuming reactants. The rate of change in the size of particles is defined as:

$$G = K_G \cdot SI^{n_G} \qquad \textbf{3.7}$$

where G is the particle linear growth rate (mm/day), K_G is the kinetic constant of growth (mm/day) and n_G is the Growth Exponent (-).

In addition to the SI, the mass of a bin X_i (g) disappearing due to the growth rate from the ith to the i+1th size $\left(\frac{\partial X_i}{\partial t}\Big|_{G_{i\rightarrow i+1}}\right)$ will be determined by the available crystal surface of the ith bin:

$$\left.\frac{\partial X_i}{\partial t}\right|_{G_{i\to i+1}} = -\,G \cdot A_i \cdot \rho_s \qquad \textbf{3.8}$$

where A_i (m^2) is the area of the i-sized crystals at any time and ρ_s is the density (g/m^3) of the crystal.

As the area is not a variable included in the model, it has to be converted to a term depending on mass:

$$A_i = \frac{Cw_i \cdot V}{\rho \cdot \frac{(L_i + L_{i+1})}{2}} \qquad \textbf{3.9}$$

where Cw_i (g/m^3) is the concentration of i sized particles at any time and L_i and L_{i+1}, the characteristic lengths of the i^{th} and $i+1^{th}$ bin, are the radius of each bin (mm).

Substituting A_i:

$$\left.\frac{\partial X_i}{\partial t}\right|_{G_{i\to i+1}} = -G \cdot \frac{Cw_i \cdot V}{\frac{(L_i + L_{i+1})}{2}} = -\,K_G \cdot SI^{n_G} \frac{Cw_i \cdot V}{\frac{(L_i + L_{i+1})}{2}} \qquad \textbf{3.10}$$

as $X_i = Cw_i \cdot V$:

$$\left.\frac{\partial X_i}{\partial t}\right|_{G_{i\to i+1}} = -\,K_G \cdot SI^{n_G} \frac{X_i}{\frac{(L_i + L_{i+1})}{2}} \qquad \textbf{3.11}$$

the change in the total mass of the i^{th} sized particles due to the growth mechanism ($\left.\frac{\partial X_i}{\partial t}\right|_G$) will be the difference between the particles that grow from the previous bin to the considered bin and the particles that grow from the considered bin to the next.

$$\left.\frac{\partial X_i}{\partial t}\right|_G = \underbrace{\left.\frac{\partial X_i}{\partial t}\right|_{G_{i-1\to i}}}_{\substack{\text{mass growing from}\\ \text{previous bin}}} - \underbrace{\left.\frac{\partial X_i}{\partial t}\right|_{G_{i\to i+1}}}_{\substack{\text{mass growing to}\\ \text{next bin}}} \qquad \textbf{3.12}$$

The definition of these steps and the interaction with the ions in the reaction is defined in Table 3.2.

Table 3.2: Stoichiometry matrix for nucleation (A) and growth (B) processes.

A

Component→i		X_1	NH_4^+	PO_4^{3-}	Mg^{2+}	H_2O	Process Rate [mass/t]
Process							
Nucleation		1	$-\frac{MW_{NH_4^+}}{MW_{Stru}}$	$-\frac{MW_{PO_4^{3-}}}{MW_{Stru}}$	$-\frac{MW_{Mg^{2+}}}{MW_{Stru}}$	$-\frac{6 \cdot MW_{H_2O}}{MW_{Stru}}$	$K_B \cdot SI^{n_B} \cdot V_R \cdot mesf_1$

B

Component→i	X_{i-1}	X_i	X_{i+1}	NH_4^+	PO_4^{3-}	Mg^{2+}	H_2O	Process Rate [mass/t]
Process								
$Growth_{i-1\to i}$	-1	$\frac{mesf_i}{mesf_{i-1}}$		$-\frac{MW_{NH_4^+}}{MW_{Stru}}$	$-\frac{MW_{PO_4^{3-}}}{MW_{Stru}}$	$-\frac{MW_{Mg^{2+}}}{MW_{Stru}}$	$-\frac{6 \cdot MW_{H_2O}}{MW_{Stru}}$	$K_G \cdot SI^{n_G} \frac{X_{i-1}}{\frac{(L_{i-1}+L_i)}{2}}$
$Growth_{i\to i+1}$		−1	$\frac{mesf_i}{mesf_{i-1}}$	$-\frac{MW_{NH_4^+}}{MW_{Stru}}$	$-\frac{MW_{PO_4^{3-}}}{MW_{Stru}}$	$-\frac{MW_{Mg^{2+}}}{MW_{Stru}}$	$-\frac{6 \cdot MW_{H_2O}}{MW_{Stru}}$	$K_G \cdot SI^{n_G} \frac{X_i}{\frac{(L_i+L_{i+1})}{2}}$

3.3.1.4. Aggregation

Aggregation is the particle enlargement process where the effective impact of two small crystals form a bigger one. It is thought that some consumption of the dissolved ions is needed to create the bond between two colliding crystals (Liew *et al*., 2003). The consumption due to the bond formation is assumed as negligible in the stoichiometry of this model and its effect is taken into account by making the aggregation kinetics proportional to the SI:

$$\beta = K_A \cdot SI^{n_A} \quad \textbf{3.13}$$

K_A (l/d) and n_A (-) are the size independent kinetic constant of aggregation (or kernel) and the Aggregation Exponent respectively and β (l/d) is the Aggregation rate. Size independent aggregation kernels are the simplest and the ones with the best results (Bramley *et al*., 1996). Some studies suggest that the effectiveness of the impact could be related to the competing speed of the bond formation and the shear rate in the reactor (Hounslow *et al*., 2013; Liew *et al*., 2003). The impact of the shear rate in the mechanisms of the PBM is not considered in this chapter and its inclusion will be discussed in Chapter 4 and Chapter 5.

When considering a volume size domain partitioned using a 2 geometric progression for the partition, a problem arises when modelling the collision of two spheres. If the colliding particles have different volumes (as an example, v and 2v) the model cannot represent the birth of the 3v sized sphere, as this size is not defined. To overcome this problem, in the construction of the DPBM, the approach of Hounslow for the discretization of the aggregation process (Hounslow *et al*., 1988) is adapted to a mass-based DPBM. The results of the approach are comparable to the results of other discretization types (Nopens *et al*., 2005) and it has been successfully used to represent struvite aggregation (Galbraith *et al*., 2014). The approach of Hounslow is based on the idea that the entity (of volume 3v) formed experimentally will be fractioned in the model: a fraction is upgraded to the next sized bin (size 4v) and another fraction stays in the biggest size of the colliding particles (size 2v).

The development of the aggregation mechanism starts by defining that the effective collision of particles of two different sizes (i and j, being $j \leq i$) is proportional to the number of entities present in the model divided by the liquid volume V_l (litre):

$$\frac{\beta \cdot n_i \cdot n_j}{V_l} \qquad \textbf{3.14}$$

where n_i and n_j are the number of particles at the i^{th} and j^{th} bin.

For a mass-based model, this means:

$$\frac{\beta \cdot X_j \cdot X_i}{V_l \cdot mesf_j \cdot mesf_i} \qquad \textbf{3.15}$$

where $mesf_j$ (g) and $mesf_i$ (g) are the mass of a j-sized and i-sized sphere respectively.

For the Death term, the mass of j^{th} size bin leaving the j^{th} bin due to collisions with class i will be the number of this effective collisions multiplied by the mass in each j sphere.

$$\frac{dX_j}{dt} = \frac{\beta \cdot X_j \cdot X_i}{V_l \cdot mesf_j \cdot mesf_i} \cdot mesf_j = \frac{\beta \cdot X_j \cdot X_i}{V_l \cdot mesf_i} \qquad \textbf{3.16}$$

analogously, the mass of i sized crystal leaving the i^{th} bin due to collisions with class j will be proportional to the effective collisions multiplied by the mass in each i size sphere. As the sum of the mass of both particles will not be enough to obtain a particle of size i+1, it is consider that a part of the particle of size i passes to the i+1 bin, whilst another part stays in i (Hounslow's approach). To this end, the mass leaving the the i^{th} bin is multiplied by a 2^{j-i} factor:

$$\frac{dX_i}{dt} = \frac{2^{j-i} \cdot \beta \cdot X_j \cdot X_i}{V_l \cdot mesf_j \cdot mesf_i} \cdot mesf_i = \frac{2^{j-i} \cdot \beta \cdot X_j \cdot X_i}{V_l \cdot mesf_j} \qquad \textbf{3.17}$$

this process is described in a diagram in Figure 3.1.

With this assumption, and considering that for the Birth term, the mass of i+1 size formed due to collisions between particles in the i^{th} and the j^{th} class, will be the sum of the mass leaving i and j classes due to collisions, mass of the solids is automatically conserved during aggregation:

$$\frac{dX_{i+1}}{dt} = \left(\frac{dX_i}{dt} + \frac{dX_j}{dt}\right) \qquad \textbf{3.18}$$

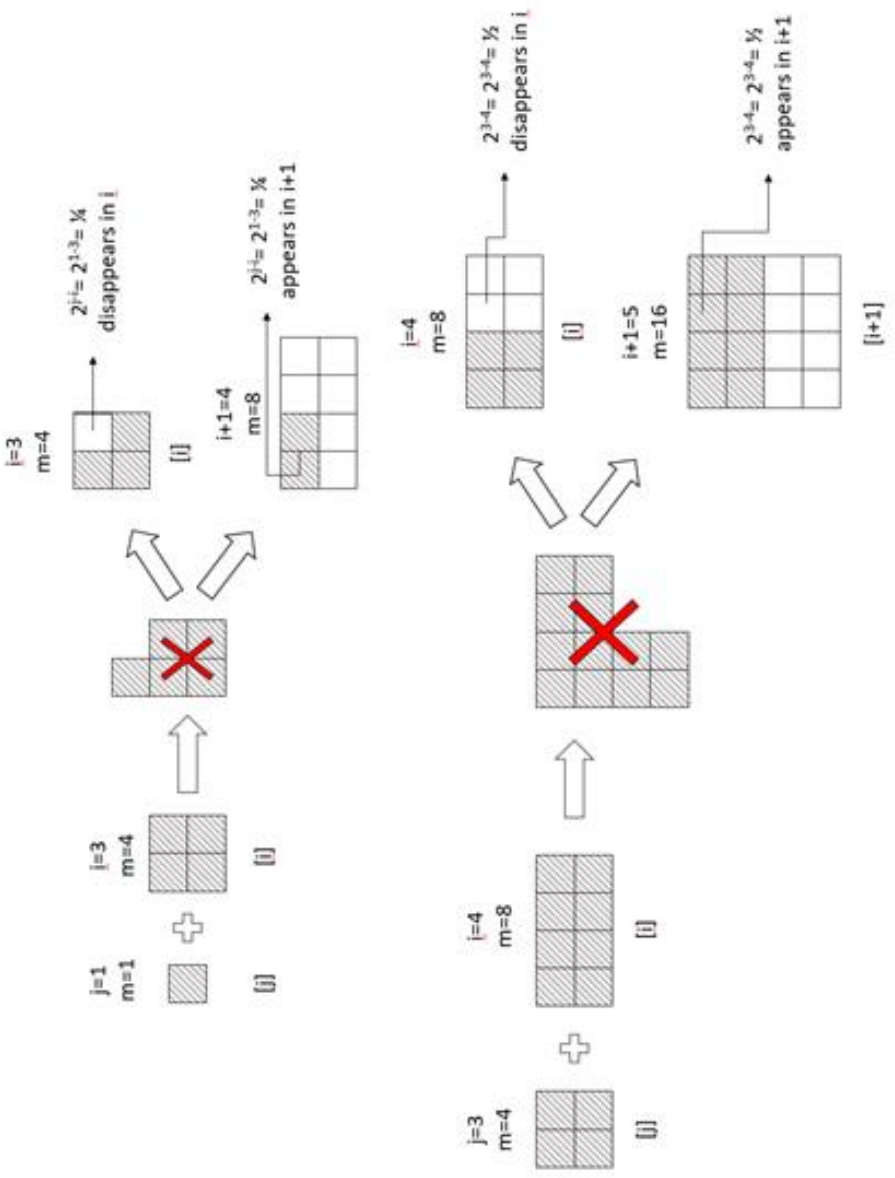

Figure 3.1: Representation of the aggregation process.

Combining equations:

$$\frac{dX_{i+1}}{dt} = \frac{2^{j-i} \cdot \beta \cdot X_j \cdot X_i}{V_l \cdot mesf_j} + \frac{\beta \cdot X_j \cdot X_i}{V_l \cdot mesf_i} = \frac{\beta \cdot X_j \cdot X_i}{V_l} \cdot \left(\frac{2^{j-i}}{mesf_j} + \frac{1}{mesf_i}\right) \quad \textbf{3.19}$$

as $\frac{mesf_j}{mesf_i} = 2^{j-i}$:

$$\begin{aligned} \frac{dX_{i+1}}{dt} &= \frac{\beta \cdot X_j \cdot X_i}{V_l} \cdot \left(\frac{1}{mesf_i} + \frac{1}{mesf_i}\right) \\ &= \frac{\beta \cdot X_j \cdot X_i}{V_l} \cdot \left(\frac{2}{mesf_i}\right) \cdot \frac{2^{j-(i+1)} \cdot mesf_{i+1}}{mesf_j} \\ &= \frac{\beta \cdot X_j \cdot X_i}{V_l} \cdot \left(\frac{2^{j-i} \cdot mesf_{i+1}}{mesf_i \cdot mesf_j}\right) \end{aligned} \quad \textbf{3.20}$$

the stoichiometry matrix for four general equations is shown in Table 3.3. The aggregation process has been modelled analogously for all possible collisions occurring between all the bins defined in the model. Thus, considering all the mechanisms involved, the dynamic mass balance for each i^{th} bin is:

For $i = 1$:

$$\frac{dX_1}{dt} = B_0 \cdot mesf_1 - \frac{G \cdot X_1}{\frac{(L_1 + L_2)}{2}} - \sum_{i=1}^{i=N_{K-1}} \frac{\beta \cdot X_1 \cdot X_i}{V_l \cdot mesf_i} \quad \textbf{3.21}$$

For $i \neq 1, N_K$:

$$\begin{aligned} \frac{dX_i}{dt} = &\frac{\frac{mesf_i}{mesf_{i-1}} \cdot G \cdot X_{i-1}}{\frac{(L_{i-1} + L_i)}{2}} - \frac{G \cdot X_i}{\frac{(L_i + L_{i+1})}{2}} \\ &+ \sum_{j=1}^{j=i-1} \frac{\beta \cdot X_j \cdot X_{i-1}}{V_l} \cdot \left(\frac{2^{j-(i-1)}}{mesf_j} \cdot \frac{mesf_i}{mesf_{i-1}}\right) \\ &- \sum_{j=1}^{j=i} \frac{2^{j-i} \cdot \beta \cdot X_j \cdot X_i}{V_l \cdot mesf_j} - \sum_{j=i+1}^{j=N_K-1} \frac{\beta \cdot X_j \cdot X_i}{V_l \cdot mesf_j} \end{aligned} \quad \textbf{3.22}$$

For $i = N_K$:

$$\frac{dX_{N_K}}{dt} = \sum_{j=1}^{j=N_K-1} \frac{\beta X_j X_{N_K-1}}{V_l} \left(\frac{2^{j-N_K+1}}{mesf_j}\right) + \frac{\frac{mesf_{N_K}}{mesf_{N_{K-1}}} \cdot G \cdot X_{N_{K-1}}}{\frac{(L_{N_{K-1}} + L_{N_K})}{2}} \quad \textbf{3.23}$$

Table 3.3: Stoichiometry matrix for aggregation process.

Component→i Process	X_i	X_{i+1}	X_{i+2}	X_{i+3}	Process Rate [mass/t]
$Aggregation_{i,j\rightarrow i+1}$	$-1-2^{i-i}\frac{mesf_i}{mesf_i}$	$2^{i-i}\frac{mesf_{i+1}}{mesf_i}$			$\frac{K_A SI^{n_A} X_i X_i}{V_l \cdot mesf_i}$
$Aggregation_{i,i+1\rightarrow i+2}$	-1	$-2^{i-(i+1)}\frac{mesf_{i+1}}{mesf_i}$	$2^{i-(i+1)}\frac{mesf_{i+2}}{mesf_i}$		$\frac{K_A SI^{n_A} X_i X_{i+1}}{V_l \cdot mesf_{i+1}}$
$Aggregation_{i,i+2\rightarrow i+3}$	-1		$-2^{i-(i+2)}\frac{mesf_{i+2}}{mesf_i}$	$2^{i-(i+2)}\frac{mesf_{i+3}}{mesf_i}$	$\frac{K_A SI^{n_A} X_i X_{i+2}}{V_l \cdot mesf_{i+2}}$
$Aggregation_{i+1,i+2\rightarrow i+3}$		-1	$-2^{(i+1)-(i+2)}\frac{mesf_{i+2}}{mesf_{i+1}}$	$2^{(i+1)-(i+2)}\frac{mesf_{i+3}}{mesf_{i+1}}$	$\frac{K_A SI^{n_A} X_{i+1} X_{i+2}}{V_l \cdot mesf_{i+2}}$

3.3.2. Parameter identifiability analysis

The use of mass as internal coordinate in PBMs is uncommon and, to the author's knowledge, it has not been used to simulate struvite precipitation until now. An identifiability analysis of the kinetic constants and exponents defining the mechanisms described in subsection 3.3.1 was considered necessary prior to any calibration procedure. This analysis was done in four steps: First, the model was implemented in WEST-DHI simulation platform. Second, six case studies in which all the mechanisms described in the model were expected to have some relevance were defined. Third, a quantification of the effect of each parameter on the model's outputs was done integrating a local sensitivity method into a global sampling method. Finally, a collinearity analysis of the model was done so as to observe possible correlation effects between the parameters.

3.3.2.1. Case studies

For the simulations performed in this chapter, six different simulation case studies were defined in WEST-DHI. Case studies A, B and C were operated in batch mode, with very high SI and no seed material. In contrast, case studies D, E and F corresponded to a continuous operation of a precipitation reactor with an initial seed loading. All the simulations considered the reactors as CSTR. All the SI provided correspond to the equilibrium value of the SI that would be obtained if no reaction occurred in the reactors.

Each of case studies A, B and C was a CSTR of 1 l capacity with an initial volume of 500 ml of a solution containing KH_2PO_4 and NH_4Cl on it. Starting at simulation time t = 0 s, 150 ml of a solution containing $MgCl_2 \cdot 6H_2O$ were added in the first 10 seconds. After that, no more external perturbation was introduced in the system. The difference among these scenarios were the initial concentrations of the species, as included in Table 3.4.

Table 3.4: Case Studies A, B and C defined for the simulations. The listed component concentrations are those corresponding to the initial experimental conditions, prior to any precipitation reaction. pH N-P is the pH of the solution containing KH_2PO_4 and NH_4Cl. pH Mg is the pH of the solution containing $MgCl_2 \cdot 6H_2O$.

Case Study	Temperature (ºC)	Mg (mol/l)	N (mol/l)	P (mol/l)	pH N-P	pH Mg	SI
A	30.00	0.15	0.19	0.10	7.99	8.06	3.91
B	23.1	0.09	0.12	0.06	8.06	6.97	3.64
C	25	0.015	0.02	0.01	8.00	8.00	1.86

For case studies D, E and F a reactor of 11.4 L of capacity was used. Temperature was 21 °C. Precipitation process started with the reactor full of a solution containing 0.228 mol/l NH_4Cl and 0.114 mol/l KH_2PO_4 and 640 g of struvite seed material of average diameter of 185 μm. Starting at simulation time t = 0 s, 3 solutions entered the reactor with constant flows and continuously for 24 h. The first solution was formed by KH_2PO_4 and NH_4Cl, the second one by $MgCl_2 \cdot 6H_2O$ and the third one by NaOH. For the three case studies, the same flow of the solution formed by KH_2PO_4 and NH_4Cl (0.3168 m^3/day) and the solution formed by $MgCl_2 \cdot 6H_2O$ (0.0253 m^3/day) were used. The difference in the conditions of the simulations was achieved by changing the NaOH dosing quantity (0.0265 m^3/day, 0.0132 m^3/day and 0.0106 m^3/day for cases D, E and F, respectively), which affected the SI in the reactor. Details can be found in Table 3.5. The SI in the reactor for cases D, E and F were 2.04, 1.19 and 0.65 respectively. The precipitated solid was retained in the reactor during the process.

Table 3.5: Description of Case Studies D, E and F defined for the simulations.

Concentration (mol/l) and component	Flow (m^3/day) in Case Study D	Flow (m^3/day) in Case Study E	Flow (m^3/day) in Case Study F
0.005 KH_2PO_4 and 0.01 NH_4Cl	0.3168	0.3168	0.3168
0.07 $MgCl_2 \cdot 6H_2O$	0.0253	0.0253	0.0253
0.008 NaOH	0.0265	0.0132	0.0106

3.3.2.2. Sensitivity analysis

The objective of running a sensitivity analysis is to verify how important each parameter is for the performance of the model. Usually, it is employed to simplify overparametrised models. In this chapter, it is used to verify that in the parameter range chosen, all the parameters and, consequently, the mechanisms, play a role in the outputs, as a previous step to the model calibration. Evaluated parameters and their ranges are included in Table 3.6. Choosing meaningful parameter values for the analysis is not straightforward, as the variability in the kernels and values for them is big in the literature. The ranges in this chapter were chosen to cover zones that included values observed in the literature review (Galbraith *et al.*, 2014; Mullin, 2001; Myerson, 2001; Triger *et al.*, 2012) and also based on previous simulations performed by the authors.

Table 3.6: Model parameters and the selected ranges.

Name	Symbol	Description	Unit	Minimum Value	Maximum Value
Kr Nucleation	K_B	Kinetic constant of nucleation	Nuclei/day·m^3	$0.5 \cdot 10^{12}$	$9.9 \cdot 10^{13}$
Nucleation Exponent	n_B	Kinetic exponent of nucleation	--	0.5	6
Kr Growth	K_G	Kinetic constant of growth	mm/day	1.0	100
Growth Exponent	n_G	Kinetic exponent of growth	--	0.7	6
Kr Aggregation	K_A	Kinetic constant of aggregation	l/day	$0.5 \cdot 10^{-5}$	$9.9 \cdot 10^{-5}$
Aggregation Exponent	n_A	Kinetic exponent of aggregation	--	0.5	6

The sensitivity analysis can be done following a global sampling technique or a local analysis technique. Global sampling methods pick parameter sets in the previously defined hyperspace in order to run the simulation with them. When enough simulations are done, an idea of how the results of the simulation change depending on the values of the parameters can be obtained (van Griensven *et al*., 2006). On the other hand, local analysis techniques evaluate the impact of changing slightly the value of the parameters at a previously defined point in the parameter hyperspace. This is especially useful when parameter values are known with some security (Brun *et al*., 2001).

Considering the big uncertainty in the values of the kinetic parameters, and in order to explore a large zone in the parameter hyperspace, the sensitivity analysis was performed integrating a local analysis technique into a global sampling method. This integration consists on repeating the local analysis in many randomly or systematically sampled points. In this chapter, the Latin Hypercube-One factor At a Time (LH-OAT) method proposed by van Griensven *et al*. (2006) was used: points were sampled using the LH scheme and local sensitivities were calculated using the OAT method.

For the quantification of the effect of each parameter, a little variation was introduced in the parameter of interest while the rest were maintained constant. The difference on the outputs for the simulations with and without this variation were computed. The result was the univocal variation on the model's outputs for the change in each parameter:

$$s_{i,j,k} = \left| \frac{100 * \left(M_O(\theta_1, \dots, \theta_j * (1 \pm f_i), \dots, \theta_n - M_O(\theta_1, \dots, \theta_j, \dots, \theta_n)\right)}{\frac{\left[M_O\left(\theta_1, \dots, \theta_j * (1 \pm f_i), \dots, \theta_n\right) + M_O\left(\theta_1, \dots, \theta_j, \dots, \theta_n\right)\right]}{2}} \right| \qquad \textbf{3.24}$$

where $s_{i,j,k}$ is the partial effect of the j^{th} parameter on each i^{th} output in the k^{th} point, f_i is the small variation in the parameter and $M_O(\cdot)$ refers to the model outputs. Note that the variation in the parameters is a fraction of the parameter value at the selected point. The obtained value of the sensitivity is already normalized.

The operation was repeated for all the parameters being analysed in each sampled point for the six different case studies: $p \cdot (n+1)$ simulations of each case study were performed, where $p = 300$ was the total number of points of the hyperspace selected

by the LH and n = 6, the number of parameters. Therefore, the influence of the six kinetic parameters used in the model was quantified using a total of 2100 runs for each of the six simulation case studies.

The result of this iterative operation is a three-dimensional matrix: a bi-dimensional matrix for each p sampled point with m (number of outputs) rows and n (number of parameters) columns. The elements in these bi-dimensional matrixes are the partial effect of each parameter on each output, $s_{i,j,k}$. The outputs used for the sensitivity analysis were pH and PSD evolution during the simulated experiment. For the A, B and C case studies they were recorded every 10 seconds for the first 2 minutes of experiment because that was the most critical period and every minute for the next 18 minutes, where little change is observed in the simulations. For the D, E and F case studies they were recorded every 10 minutes for the first two hours and every hour for the next 22 hours.

Total influence of the parameter in each point ($\delta_{k,j}$) was calculated averaging the effect for all the sampled outputs on a certain point:

$$\delta_{k,j} = \sqrt{\frac{1}{m}\sum_{i=1}^{m} s_{i,j,k}^2} \qquad \textbf{3.25}$$

the averaged results formed a bidimensional matrix **S**, named sensitivity matrix, where each element was the averaged effect of the change of each parameter on each point ($\mathbf{S} = \{\delta_{k,j}\}$).

3.3.2.3. Collinearity analysis

A set of parameters in a model is identifiable if it fulfils two conditions: First, the individual change in the parameters has to affect the model outputs. Second, the change in one of the parameters cannot be compensated with an adequate change in another parameter (Brun *et al.*, 2001). From the sensitivity analysis, it can be concluded which of the parameters have the biggest effect on the simulation outputs for the considered parameter bounds. However, it does not give any information on a possible correlation effect within the parameter set. In order to assess possible compensation effects on the parameters, a collinearity analysis was performed.

In the collinearity analysis, parameters are usually organized in subsets. These subsets have k parameters, being $k \leq n$, the total number of parameters in the model.

The Collinearity index (γ_k) of the parameters under study was calculated as proposed in Brun *et al*. (2001):

$$\gamma_k = \frac{1}{\min_{\|\boldsymbol{\beta}_C\|=1} \left\|\tilde{\mathbf{S}}_k \boldsymbol{\beta}_C\right\|} = \frac{1}{\sqrt{\lambda_k}} \quad \textbf{3.26}$$

being $\tilde{\mathbf{S}}_k$ the normalized matrix with the k parameters forming the subset under study, $\boldsymbol{\beta}_C$ is a vector of coefficients of length k and norm = 1 and λ_k the smallest eigenvalue of the matrix $\tilde{\mathbf{S}}_k^T \tilde{\mathbf{S}}_k$. Parameter identifiability problems are found within the set under study when the limit in the Collinearity index exceeds 15 (Brun *et al*., 2002) or 20 (Soetaert and Petzoldt, 2010). As the identifiability of a parameter set depends on both the impact on the output of the change in the parameters and the linear independency of the subset, an additional index was calculated. The Importance index, ρ_k, considers both effects and it is calculated as (Brun *et al*., 2001):

$$\rho_k = (\det[\mathbf{S}^T \mathbf{S}])^{1/2k} \quad \textbf{3.27}$$

a high sensitivity and a low collinearity will result in a high ρ_k value for the subset, which means a high identifiability.

The collinearity analysis was performed for all the points sampled with the LH for two types of parameter sets. First, all the parameters were analysed in pairs to see if there were direct compensation effects between parameters in certain zones of the chosen range. Second, the Collinearity index and the Importance index were calculated for the six parameters, to find zones of the parameter range where all the parameters in the model are identifiable for the case studies used.

The parameter identifiability study was done combining Matlab and WEST-DHI. The LH scheme was implemented in Matlab and the values of the parameters picked for each run. Once these values were chosen, the information was sent to the WEST simulation platform and the six case studies were reproduced. The information about the outputs of the model was recorded from the WEST-DHI simulation and translated to Matlab. Afterwards a perturbation of 1% was introduced in the first parameter and the simulations in WEST-DHI were repeated with the perturbed parameter set. This operation was repeated for all the parameters under study. The information of the outputs was used to calculate the sensitivities, the Collinearity index and the Importance index. Figure 3.2 explains the steps followed.

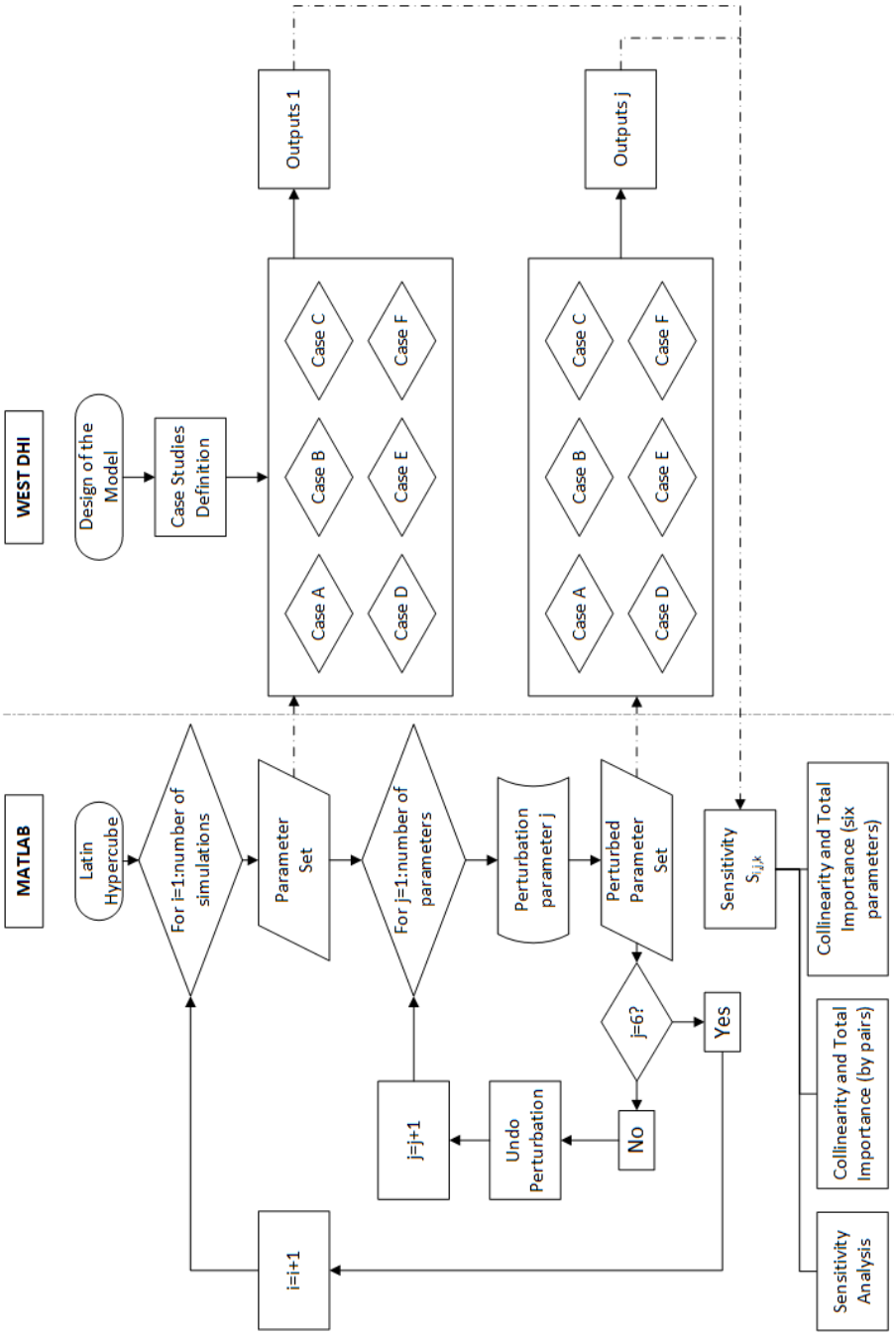

Figure 3.2: Procedure to calculate sensitivities and collinearity in this contribution.

3.3.3. Experimental set-up

Experimental data for the determination of the parameter values was obtained from precipitation batch tests run in the laboratory. The batch test were performed in a magnetically stirred cylindrical vessel. The magnetic stirrer rotated at 300 rpm in all cases, to ensure similar hydrodynamics in all runs. 2 experimental conditions (corresponding to simulation case studies A and B) were used. Each of the conditions was run twice. The objective was to analyse the effect of different initial SI on the pH evolution and on the final PSD.

In all the cases, 500 ml of a dissolution prepared with a determined quantity of KH_2PO_4 and NH_4Cl were left in a 1-L capacity vessel. After that, 150 ml of a $MgCl_2 \cdot 6H_2O$ solution were added in ten seconds. Initial values of temperature, pH, concentrations and supersaturation (calculated in WEST-DHI) are included in Table 3.4. As can be observed, initial concentration of species is significantly higher than those found in real WRRFs. This approach was followed for two reasons: in order to obtain enough solid mass in the precipitation for the PSD measurements and to experimentally analyse processes where the primary homogeneous nucleation is important.

Each of the precipitation process was run for 20 min. The pH evolution and the final PSD were used for the determination of the kinetic constants and exponents. pH was measured every half second for the 20 min that the experiment lasted. After the 20 min, the experiment was stopped. The precipitated solid was filtered and dried at 40º C for 96 h. Total mass of obtained solid was weighted and, after that, final PSD was obtained measuring the dried solid in air suspension by laser diffraction using a SYMPATEC H820.

3.4 RESULTS AND DISCUSSION

The model presented in section 3.3.1 was assessed from an identifiability and predictive capacity point of view. For this issue, first, the model was implemented in WEST-DHI. Second, different simulation scenarios were run to obtain meaningful results from the numeric analysis. Finally, a parameter set was found that could represent well the data from experiments performed in the laboratory. Results from those activities are included in this section.

3.4.1. Parameter identifiability module

3.4.1.1. Sensitivity analysis

Results from the sensitivity analysis showed that all the parameters had some effect on the outputs. The limit for considering a parameter non identifiable due to its low effect on the outputs is 1/1000 compared with the parameter with the biggest effect (Gábor *et al*., 2017). This is a substantially smaller value than the result obtained in this study. Therefore, all parameters were considered to play a role in the outputs. The total effect of each parameter on the total output for all the points sampled, $\delta_{k,j}$, was included in Figure 3.3.

As observed in Figure 3.3, the parameters had different distribution of their sensitivity within the pre-selected ranges. It should be reminded that this sensitivity calculation only informed about the zone of the parameter range where each parameter affected the outputs, not where it could represent experimental data with more accuracy. In addition, as the results of the sensitivity analysis could be biased by the values of the rest of the parameters, more meaningful conclusions were obtained when the effect of the collinearity was considered. However, before that, there were some tendencies that should be indicated.

Attending the nucleation rate, Kr Nucleation had a constant and relatively low effect on the outputs for all the range. This result agreed with other studies, where even for larger ranges of the parameter value, the change in the nucleation constant had a little total effect (Hanhoun *et al*., 2013). The sensitivity of the Nucleation Exponent was relatively high and increased with its value. This could be explained by the fact that the case studies A, B and C used in the simulations had high initial SI and no seed material, which are the experimental conditions where primary homogeneous nucleation is most favoured. As there is not initial crystal mass in the solution, the primary homogeneous nucleation is the mechanism that triggers the precipitation. This will inevitably affect the evolution of the whole PSD and not only the smallest size. How fast particles are created will limit the consequent growth and aggregation of bigger particles, as it will limit the available concentration of them. Therefore, it will be an important mechanism for the evolution of the pH and PSD. On the other hand, case studies D, E and F had an initial seed loading and had relatively low SI (especially case study D). In these conditions, particle enlargement mechanisms

should be dominant, however, formation of fines can still occur (Agrawal *et al.*, 2018).

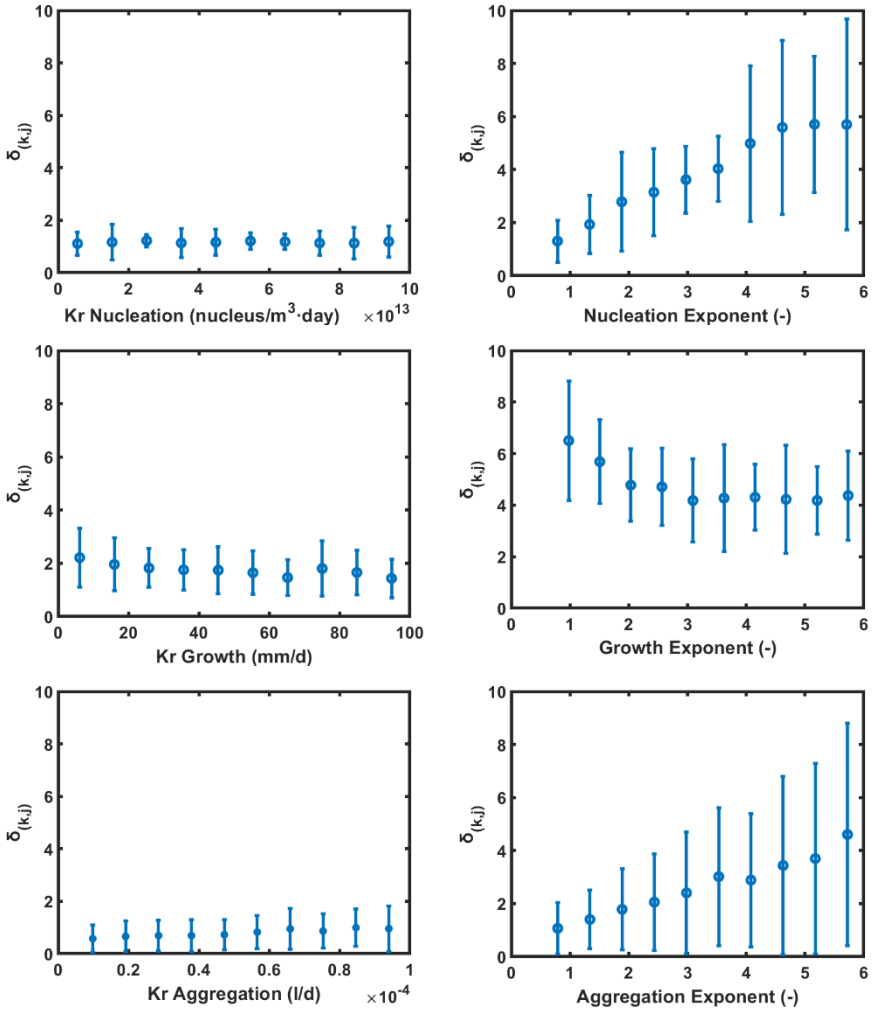

Figure 3.3: After linearly partitioning each parameter range in ten bins, representation of the averaged, maximum and minimum values of total sensitivities of the parameters within the points sampled inside each bin for (a) Kr Nucleation, (b) Nucleation Exponent, (c) Kr Growth, (d) Growth Exponent, (e) Kr Aggregation and (f) Aggregation Exponent.

Kr Growth and Growth Exponent showed different tendencies. The sensitivity of the Kr Growth is relatively constant for the whole range. Its value is nearly twice the value of the Kr Nucleation, but it is significantly smaller than the sensitivities of the three exponents. Sensitivity of the Growth Exponent reached the highest sensitivity of the six parameters for its lowest values. This highlighted the relevance of the process: Growth process is an important mechanism for different experimental conditions as it has a big effect on reactants consumption and, consequently, in the PSD. Sensitivity of the Growth Exponent decreased when its value increased, but it maintained a high sensitivity for the whole range.

Considering the parameters that define aggregation, Kr Aggregation had a low and constant effect for all the parameter range. On the other hand, Aggregation Exponent presented higher average sensitivities as it increased. However, the dispersion of the values of the sensitivity was bigger than it was for other parameters, having some of the high values of the Aggregation Exponent a big effect on the outputs and others a very small one. This phenomenon needed further study and for that issue the effect of the Aggregation Exponent was analysed for each case study individually and the results recorded in Figure 3.4.

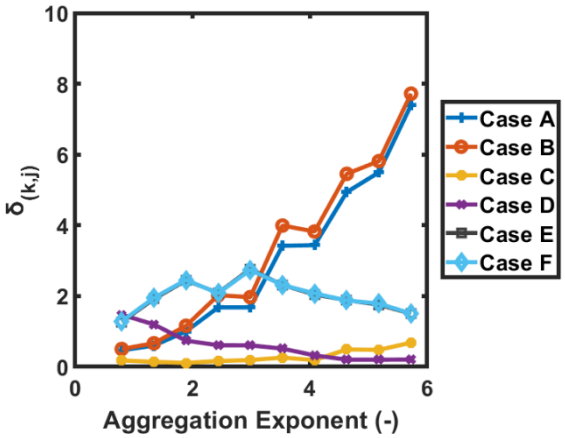

Figure 3.4: Averaged value of for each bin of the linearly partitioned range of the Aggregation Exponent for the six case studies.

From this analysis some ideas were obtained. Firstly, there was a clear increase of the effect of the Aggregation Exponent as its value incremented for the case studies

A and B. This effect could be explained in the model because a higher value of the Aggregation Exponent would mean a higher rate of aggregation for high SI for the same concentration of particles. Therefore, particles would get bigger faster at the initial steps of the precipitation (without reactants consumption), reducing the available surface area. Less surface area would mean less possibility to grow, which would mean a slower precipitation. A slower precipitation would maintain the SI high for more time, making the aggregation mechanism important for a longer period of time. However, experimental evidence from the literature show that when reactors are operated unseeded and with high SI, formation of fines governs the precipitation process rather than aggregation (Agrawal *et al.*, 2018). Moreover, aggregation is important when the reactor is seeded and works in continuous mode (Shih *et al.*, 2017). These favourable experimental conditions for aggregation are far from case studies A and B and are more similar to case studies D, E and F, where the trend of the sensitivity of the Aggregation Exponent is different (it is bigger for low values).

From the analysis of the parameters of the aggregation, two conclusions could be obtained: the first one was that the effect of the Aggregation Exponent for the highest values seemed not to be able to represent correctly the mechanism, as it gained relevance in case studies where it should not be important. The second one was that for certain experimental conditions (case studies D, E and F), the effect of the Aggregation Exponent can be important, and therefore, aggregation should always be considered when modelling precipitation processes.

3.4.1.2. Identifiability analysis

The identifiability analysis finds possible correlations amongst the parameters under study. As the objective of this analysis was to evaluate the possible interactions in the model, all the parameters were considered. However, when the number of parameters increases it is difficult to see their real effect on the Collinearity index. Therefore, looking for direct compensation effects, the Collinearity index and the Importance index were calculated first for each point sampled with the LH for every pair of the parameters. Afterwards, the operation was repeated for the whole set of six parameters that describe the model.

3.4.1.2.1.Identifiability analysis for parameter pairs

Results of the maximum value of the Collinearity index, the maximum Importance index and the minimum Importance index for the analysis for parameter pairs were included in Table 3.7.

Collinearity index values between 15 and 20 have been given as critical for parameter identifiability in the literature (Brun *et al.*, 2002; Soetaert and Petzoldt, 2010). In the analysis performed, there is a pair of parameters (Kr Aggregation and Aggregation Exponent) with its value above 15. The distribution of the Collinearity index for that pair of parameters was included in Figure 3.5.

Kr Aggregation and Aggregation Exponent had collinearity problems for big values of the exponent for any value of the Kr Aggregation. This agreed well with the sensitivity of Kr Aggregation, which was low and constant for the whole range (see Figure 3.3,e) and with the big variability of the sensitivity of the Aggregation Exponent for big values (see Figure 3.3,f). In addition, it showed that Aggregation Exponent is at least biased by other parameter. This means that depending on the considered experimental conditions chosen for the calibration its estimation could not be possible.

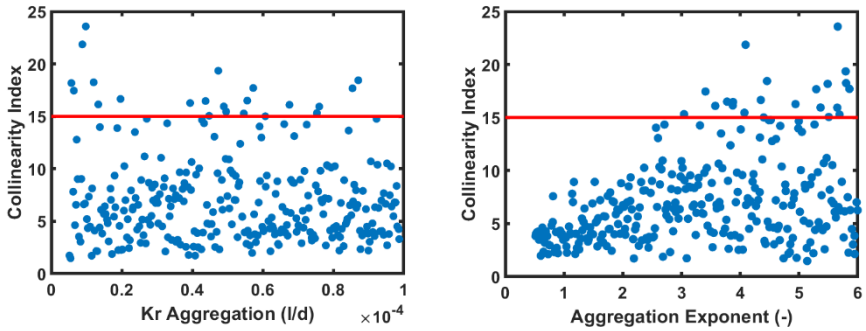

Figure 3.5: Collinearity Index calculated in pairs for Kr Aggregation and Aggregation Exponent vs. (a) sampled values of Kr Aggregation and (b) sampled values of Aggregation Exponent.

Table 3.7: Results of the identifiability analysis performed in pairs of parameters. The grey shaded value correspond to the pair of parameters with a maximum Collinearity index above 15 in the 'Max. Collin' column and to the pairs of parameters with the highest Identifiability index in the 'Max. Ident' column.

Number of Pair	Parameter 1	Parameter 2	Max. Collin	Max Ident	Min. Ident
1	Kr Nucleation	Nucleation Exponent	4.67	250.35	37.73
2	Kr Nucleation	Kr Growth	5.32	170.49	48.06
3	Kr Nucleation	Growth Exponent	4.31	256.26	98.21
4	Kr Nucleation	Kr Aggregation	2.72	90.02	18.44
5	Kr Nucleation	Aggregation Exponent	2.45	216.31	20.72
6	Nucleation Exponent	Kr Growth	2.91	**463.84**	53.53
7	Nucleation Exponent	Growth Exponent	7.81	**508.07**	85.63
8	Nucleation Exponent	Kr Aggregation	3.03	293.45	17.58
9	Nucleation Exponent	Aggregation Exponent	2.83	**630.79**	16.38
10	Kr Growth	Growth Exponent	6.68	**463.46**	73.14
11	Kr Growth	Kr Aggregation	2.97	203.30	22.12
12	Kr Growth	Aggregation Exponent	2.17	396.42	26.41
13	Growth Exponent	Kr Aggregation	3.42	296.24	38.32
14	Growth Exponent	Aggregation Exponent	3.87	**637.14**	40.62
15	Kr Aggregation	Aggregation Exponent	**23.57**	244.79	5.35

More generally, pair of parameters sharing mechanism (pairs 1 and 10) or pair of parameters with the same relationship with SI (pairs 2 and 7) could have direct compensation problems if less simulation scenarios or data was used for the identifiability analysis. For instance, if only the information of the case studies A, B and C was used, the effect on the outputs could be compensated (being the value of the Collinearity index equal to 31) for Growth Exponent and Nucleation Exponent when both had big values, especially Growth Exponent. These two parameters determine the relationship of nucleation and growth with the SI. High values of Nucleation Exponent would lead to high values of concentration of the first bin very fast, which would at the same time accelerate the growth from the first bin to the second, the second to the third and so on. High values of Growth Exponent would accelerate growth at high SI, too. Therefore, for certain experimental conditions (in this case, case studies A, B and C) these parameters could be correlated, even for a big amount of considered data. In the analysis carried out in this chapter, a total of six case studies were considered. Therefore, this correlation was not a problem, as the case studies represented experimental conditions where the different effect of the parameters in the simulation could be distinguished.

Results from the Importance index for the parameter pairs (see Table 3.7), indicated that the pairs of parameters with the highest maximum Importance index were the ones combining the three exponents and the Kr Growth. This result agreed well with the values of the sensitivities, which were lower for the other two parameters (Kr Nucleation and Kr Aggregation). Big differences were found between the maximum and minimum value, which remarks that the parameter identifiability largely depended on the parameter values.

3.4.1.2.2.Identifiability analysis for the six parameters

Results of the collinearity analysis of the whole parameter set, stated that from the 300 sampled parameter combinations, 251 had a Collinearity index below the threshold of 15. As the six parameters can be involved in combinations with high Collinearity index (almost 15 or more), finding a zone graphically with no collinearity issues that include the effect of all the parameters is not straightforward. Therefore, the effect of the collinearity is included in the representation of the Importance index.

The Importance index combines information from the sensitivity and collinearity of the parameters. Figure 3.6 represented the Importance index of the six parameters in two plots for the four parameters that led to parameter pairs with highest Importance index. The graphs clearly showed that low values of the Growth Exponent and the Kr Growth, combined with high Nucleation Exponents led to parameter sets with a better identifiability (Figure 3.6,a). Effect of the Aggregation Exponent was not as clear (Figure 3.6,b). This was a logical result, as the Aggregation Exponent showed little average sensitivity for values below 2 (Figure 3.3,f) and a high collinearity with the Kr Aggregation for high values (Figure 3.5,b).

From the obtained results it could be concluded that there were zones of parameter values with theoretical identifiability problems. This could be even more problematic if less data or experimental scenarios were used, as it is the usual case for PBM calibration. The identifiability problem could explain the differences in the values of the parameters found in literature for calibrated PBMs, more than small changes in the structures of the PBM or the used solving method. Considering this, a calibrated PBM should clearly indicate the limits of its application, as it is possible that the parameters chosen are not general values, but compensated among them for the case studies and/or parameter values chosen. In addition, when using the models, it should be considered that the parameter values can be good enough to represent a certain amount of data, but it is not correct to consider the processes or parameters individually, as they might be biased by the value of the rest of the parameters of the model.

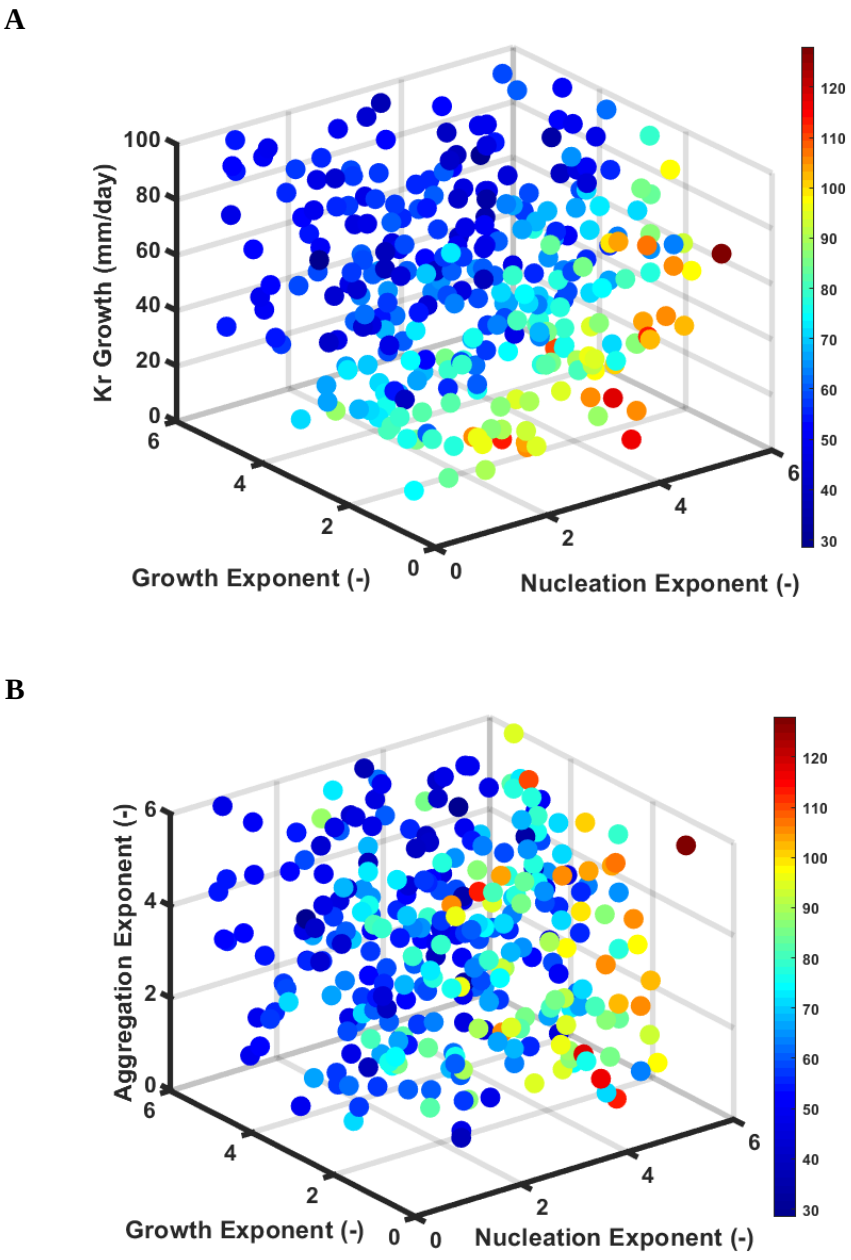

Figure 3.6: Importance index for the most important parameters: (a) Nucleation Exponent, Growth Exponent and Kr Growth and (b) Nucleation Exponent, Growth Exponent and Aggregation Exponent.

On the other hand, there were zones where the identifiability was possible for the data and case studies used. Some of the zones of the parameters with high identifiability (mainly for the exponents) were reasonable values, according to classic precipitation theories. This is important, as enforces the idea that the PBM can explain the precipitation in a realistic way, by including the main mechanisms in an explicit way.

3.4.2. Fitting the model to the experimental data

Based on the information obtained in the mathematical analysis conducted previously, the parameters under study were adjusted to reproduce the data obtained from the experiments undertaken in the laboratory and explained in subsection 3.3.3. Experimental results showed a sharp decay of the pH when the solutions contacted. This is something expected due to the high SI chosen for the experiments. The obtained solid size was small, as it tends to occur for high SI (Fang *et al*., 2016). Figure 3.7 shows the average of the evolution of the pH and the final PSD in the experiments. Obtained struvite mass was 7.6445 g for case A and 4.6601 g for case B.

For the adjustment, values were chosen from the zone of the highest identifiability for those parameters that obtained a high value of the Importance index in the previously conducted analysis (exponents and Kr Growth). Kr Nucleation and Kr Aggregation were parameters with lower identifiability and their effect is not as important on the outputs as that of the rest of the parameters. Once the most important parameters were fixed, they were manipulated within the analysed range in order to obtain a value that led to a reasonable similarity between the experimental data and the results from the simulations.

The Nucleation Exponent was fixed at 5. This value agrees with other contributions where it is stated that the exponent for secondary nucleation is often above 2 and the exponent for homogeneous nucleation is typically much higher (Myerson, 2001).

Growth Exponent was fixed at 2. Growth Exponent presented a high identifiability for zones in which its value was low. In addition, classic growth theories state that the value of the Growth Exponent is usually between 1 and 2 (Mullin, 2001). Moreover, its value has been chosen between 1 and 3 for different definitions of the growth rate (Li *et al*., 2003).

Regarding Aggregation Exponent, as mentioned in subsection 3.4.1, the high sensitivity found for its high values corresponded to unseeded, very high SI and batch simulation cases. On the contrary, the continuous case studies showed higher values of the sensitivity for lower values of the parameter. In addition, high values of Aggregation Exponent led to collinearity problems. Therefore, it was decided to choose a value of 2 for the Aggregation Exponent, out of the zone with collinearity problems. This value is in consonance with the observations made by Wócjik and Jones (1997), that found a linear increase of the agglomeration kernel with the growth rate.

Kr Growth was selected in this contribution at 12 mm/d, slightly lower than the value of 18 mm/d obtained in Galbraith *et al.* (2014) for the growth rate of struvite.

As explained above, the parameters with the lowest impact in the outputs were adjusted at the end: Kr Nucleation was fixed at 10^{13} nuclei/m^3·day. This value is lower than the values obtained in Galbraith *et al.* (2014) and in Triger *et al.* (2012). However, those values in the literature were obtained for significantly lower values of the Nucleation Exponent in Galbraith *et al.* (2014) or a different kernel in Triger *et al.* (2012). On the other hand, Kr Aggregation was fixed at 10^{-5} l/d, lower value than the value obtained in Galbraith *et al.* (2014). However, the exponent of the aggregation was calibrated at 5.259 in Galbraith *et al.* (2014), whereas here it is fixed at 2. The fact that other contributions, reported different exponent and kinetic constant values while maintaining a good agreement between the simulated and the experimental values highlighted that correlation may exist when calibrating a PBM and emphasized the idea that it is very difficult to compare parameter values between contributions.

Values obtained for the parameters are recorded in Table 3.8. It should be noted that the presented parameter values do not claim to be a perfect parameter set to describe the struvite precipitation process in every experimental condition, as this is not an objective of this chapter. However, the values recorded in Table 3.8 are considered a promising first step before a more rigorous calibration is done in Chapter 5.

Table 3.8: Parameter set chosen to predict experimental data.

Parameter	Value	Units
Kr Nucleation	10^{13}	Nuclei/(day·m^3)
Nucleation Exponent	5.0	---
Kr Growth	12.0	mm/d
Growth Exponent	2.0	---
Kr Aggregation	10^{-5}	l/d
Aggregation Exponent	2.0	---

Figure 3.7 confronted the simulated pH evolution and final PSD with the experimental values. There was a small difference in the steady state for the pH value, this difference is related with the chosen Ksp. The difference was in concordance when the obtained solid was compared in the experiments and the simulations: 7.6445 g in the experiment and 7.7512 g in the simulation for Case A and 4.6601 g in the experiment and 4.8868 g in the simulation for Case B. Discrepancies in the PSD between the experimental and simulated results were related with the low accuracy of the laser diffraction method to measure non-spherical particles (Hanhoun *et al*., 2013). In addition, as the measurements were done with dry solid it is possible that some post-drying agglomeration occurred, resulting in bigger particles measured than the ones existing before the filtration.

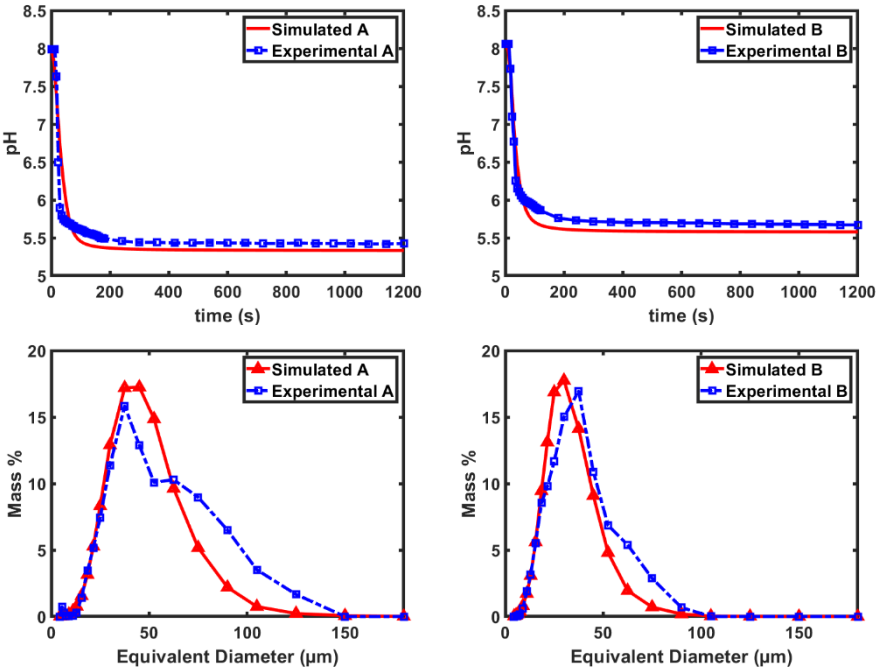

Figure 3.7: Simulated and experimental pH evolution for case study A (a) and case study B (b) and simulated and experimental final PSD for case study A (c) and case study B (d).

3.5 SUMMARY

For the optimum design and operation of material recovery technologies based on precipitation, conventional models used in the wastewater treatment industry should be updated, for example considering PSD and the effect of some operational variables. Developments done in the chapter have been focused on two main aspects:

1) A new mass-based PBM has been developed, coherent in its structure with conventional wastewater treatment models and compatible with them. The model has been described using the usual notation in wastewater treatment modelling (stoichiometric matrix and kinetic vector), state variables are mass of components instead of number of particles, which guarantees mass continuity. The model proposed in this study included main precipitation mechanisms and common wastewater equilibrium reactions, as ion pairing and acid-base reactions. Moreover, other reactions related to liquid-gas

transfers, used in some precipitation technologies, or even biological reactions could be easily incorporated if required. The model constructed has been implemented successfully in WEST-DHI simulation platform.

2) The results obtained from the sensitivity and collinearity analysis demonstrate that all the parameters have some weight in the outputs and that there are large zones of the parameter values where the identifiability is possible. Therefore, the structure of the model is considered valid. However, zones where correlation exists between the parameters were identified. Correlation effects could explain the variability in the parameter values found in the literature, where less data is available for calibration than the one generated synthetically. Correlation effects of the parameters should be considered before calibrating a PBM.

Finally, the model has been experimentally verified and it demonstrated its capacity to reproduce some experiments performed in the laboratory with reasonable values of the parameters. A more rigorous calibration using more experimental data was performed in the fifth chapter of this thesis.

CHAPTER 4

EFFECT OF THE SHEAR RATE AND SUPERSATURATION ON THE NUCLEATION AND GROWTH OF STRUVITE IN BATCH STIRRED TANK REACTORS

This chapter has been redrafted from:

B. Elduayen-Echave, M. Azcona, P. Grau, P.A. Schneider, Effect of the shear rate and supersaturation on the nucleation and growth of struvite in batch stirred tank reactors, J. Water Process Eng. 38 (2020). doi:10.1016/j.jwpe.2020.101657.

4.1 ABSTRACT

Controlled struvite precipitation is a promising solution for P recovery in WRRFs. PSD of recovered struvite affects its efficacy as a fertilizer, so should be considered in the design and operation of struvite recovery reactors. This chapter analyses the effect of varying the average shear rate (between 150 s^{-1} and 876 s^{-1}) and SI (between

0.76 and 2.96) in two different experimental set-ups. Solution pH and particle number and size measurements using an electric zone sensing method are used to monitor the process. In addition, photomicrographs are used to observe the shape of the precipitated particles. Interestingly, for identical thermochemical conditions, a higher mixing intensity, associated with the shear rate, leads to shorter induction times, faster precipitation and a greater particle density. On the other hand, for similar mixing conditions, a higher SI is also linked with shorter induction times, faster precipitation and a greater particle density. From the experimental data it is concluded that the effect of the fluid shear rate cannot be ignored and should be further studied in the precipitation process.

4.2 BACKGROUND

Municipal wastewater has the potential to substitute a significant portion of the increasing global demand of P (Amann *et al*., 2018). Consequently, recovery of P from wastewater has become an emerging concern (Peng *et al*., 2018). Among the available options to recover P, controlled precipitation of mineral phosphates, most notably struvite, has gained interest in recent years as a candidate for P recovery in WRRFs (Peng *et al*., 2018; Robles *et al*., 2020). Struvite is a well-known fertilizer and its use has been approved in some jurisdictions (i.e. Crystal Green ® obtained from Pearl™ and BioSTRU ® from NuReSys™ are certified fertilizers in US/UK and Belgium, respectively (Desmidt *et al*., 2015)), while other countries, mainly central and northern European, are implementing laws that will transition towards closing the P cycle (Günther *et al*., 2018). The support of European public policies to recover P in WRRFs, instead of simply eliminating it (Huygens and Saveyn, 2018) is important to the development of a stable market for the recovered struvite that would encourage a more generalized implementation of nutrient recovery technologies.

In parallel to the development of new legal frameworks, a better understanding of the process will assist in the design and implementation of struvite recovery technologies. Due to the interest generated, several studies have been performed analysing struvite precipitation's main technical aspects, summarized in recently published reviews (Desmidt *et al*., 2015; Peng *et al*., 2018; Robles *et al*., 2020; Yetilmezsoy *et al*., 2017). The precipitation of struvite depends on the process thermochemistry, including pH, saturation level, temperature, presence of other

ions/complexes, as well as mixing energy and the presence of seed material (Le Corre *et al*., 2009). Many experimental studies have elucidated the influence of key variables, most notably struvite SI, on the precipitation rate of struvite (Agrawal *et al*., 2018; Crutchik and Garrido, 2016; Mehta and Batstone, 2013). However, to commercialize the recovery process, the purity and PSD of the precipitant must be considered as they vary with each technology and affect to the techno-economic performance of proposed technologies (Desmidt *et al*., 2015), the efficiency of the resultant fertilizer (Li *et al*., 2019) and the separation of the recovered product from the liquid phase (Wilsenach *et al*., 2007).

The PSD in the reactor evolves as a consequence of simultaneously occurring precipitation mechanisms, including nucleation, growth and aggregation, all of which are affected by the hydrodynamics at varying mixing scales (macromixing, mesomixing and micromixing). While recent publications have analysed the effect on the PSD of changing the upflow velocity within the reactor (Tarragó *et al*., 2016; Ye *et al*., 2016) or changing the stirrer type in a stirred reactor (Ronteltap *et al*., 2010), the effect of hydrodynamics remains uncertain (Ariyanto *et al*., 2014) and must be further studied (Ronteltap *et al*., 2010; Wilsenach *et al*., 2007). For example, another recent contribution suggests that smaller particles of struvite can be obtained with increased agitation (Fang *et al*., 2016), while the opposite trend was found for struvite-K formed in synthetic urine using a stirred reactor (Zhang *et al*., 2018). Finding conflicting results in the literature for the relationship between the mean crystal size and the mixing intensity occurs for other substances (Torbacke and Rasmuson, 2001). The absence of a validated methodology that considers the effect of different mixing intensities is a problem in predicting the PSD (Zauner and Jones, 2000b) and likely explains at least some of these discrepancies. In addition, mixing in these contributions is defined by changing a particular operational variable in each system, which modifies the system operation at different mixing scales and makes the obtained results hard to extrapolate to other precipitation systems.

Experimental data obtained in small-scale reactors that limit the impact of macromixing could help to better understand the fundamentals of micromixing in each mechanism and subsequently use this knowledge for the design, operation and optimization of larger systems. Assessing the impact of micromixing is important as it is the mixing scale that directly impacts the mechanisms (Phillips *et al.*, 1999). Therefore, its effect, characterised as a varying shear rate or energy dissipation rate, has been studied in precipitation systems from an experimental (Tribout *et al*., 1996;

Wolkowicz, 1978) and modelling perspective (Baldyga *et al*., 1995; Hounslow *et al*., 2013; Phillips *et al*., 1999). Hence, the objectives of this chapter are to identify the effect of the SI and local mixing intensity, characterised as the average shear rate on struvite nucleation and growth and to obtain relevant data for calibration purposes. The SI and the shear rate are operational variables ideally independent of the technology or experimental conditions of the study. Therefore, they were related with the induction times and the evolution of the precipitation process in two different experimental set-ups. In addition, in one of the experimental set-ups the evolution of the PSD was recorded. These data could be of help to understand the complex effect of mixing at local scale and use it to improve the P management and recovery. Furthermore, the data gathered in this chapter will be used in the Chapter 5 for the calibration of the PBM presented in Chapter 3.

4.3 MATERIALS AND METHODS

The initial concentration of all species and the pH (related to the SI) and the mixing intensity (related to the shear rate) were varied for two different experimental set-ups, referred to as Experiment A and Experiment B. In all experiments the time evolution of solution pH was monitored, since pH decay can be associated with the extent of precipitation in a batch experiment (Hanhoun *et al*., 2013). In Experiment B the evolution of the PSD was measured for samples periodically removed from the reactor.

4.3.1. Operational variables

4.3.1.1. Saturation Index (SI)

The SI is calculated in WEST-DHI wastewater treatment simulation platform, using typical equations and guidelines (Lizarralde *et al*., 2015) and the $Ksp_{Stru}=7.58\cdot10^{-13}$ value used throughout the thesis, as the model reproduced well the pH equilibrium values and obtained mass quantity in the results of Chapter 3.

4.3.1.2. Mixing intensity

The mixing intensity was changed in Experiments A and B by varying the rotational speed of the stirrer. The stirrer speed was varied from 300 rpm to 800 rpm in Experiment A and from 200 rpm to 400 rpm in Experiment B. As the stirrer speed is

not a variable that can be directly related between different systems, its effect was related to the average shear rate. The average shear rate can be related to the specific energy dissipation rate as shown in section 2.3. The average shear rate in the reactor (eq. 4.1) was calculated as follows (Ilievski *et al*., 2001):

$$\gamma = \left[\frac{P_i}{\mu \cdot V}\right]^{1/2} \quad \textbf{4.1}$$

where γ is the average shear rate (s^{-1}) in the fluid volume, P_i is the power input to the reactor (W), μ is the dynamic viscosity (kg/m·s) and V is the volume of liquid in the reactor (m^3).

The power input (eq. 4.2) was calculated as follows (Wodołażski, 2017):

$$P_i = N_P \cdot \rho_L \cdot {N_S}^3 \cdot {D_i}^5 \quad \textbf{4.2}$$

where N_P is the power number (-), ρ_L is the density of the liquid (kg/m^3), N_S is the stirring speed (s^{-1}) and D_i is the diameter of the impeller (m).

Experiment A was mixed with a magnetic stirrer and N_P was calculated in eq. 4.3 based on the correlation proposed for unbaffled vessels by (Nagata, 1975), as in (Liu and Rasmuson, 2013):

$$N_P = \frac{A_1}{Re} + A_2 \cdot \left(\frac{10^3 + 1.2 \cdot Re^{0.66}}{10^3 + 3.2 \cdot Re^{0.66}}\right)^{A_3} \cdot \left(\frac{h}{D_T}\right)^{\left(0.35+\frac{b}{D_T}\right)} \cdot (\sin\theta_{An})^{1.2} \quad \textbf{4.3}$$

where A_1, $A_2$and A_3 depend on system geometry, D_T is the inner diameter of the tank (m), h is the height of the liquid (m), b is the diameter of the stir bar (m), θ_{An} is the angle between agitator blade surface and horizontal surface, considered 90° (Liu and Rasmuson, 2013), and Re is the Reynolds number, defined in eq. 4.4 as:

$$Re = \frac{N_S \cdot {D_i}^2 \cdot \rho_L}{\mu} \quad \textbf{4.4}$$

with these considerations, N_P value is between 1.21 and 1.24 in the Experiment A. Experiment B was mixed with a 5-cm diameter pitched 4-bladed impeller (PBT). The power number of this stirrer is considered to be 1.3 (Asiri, 2012; Ayranci and Kresta, 2011).

4.3.2. Experimental set-up

4.3.2.1. Experiment A

Experiment A was executed in a 250-mL reaction vessel of inner diameter 56.3 mm, mixed with a magnetic stirrer (IKA® RCT basic IKAMAG™ safety Control, IKA-Werke, Germany). The bar had a length of 30.5 mm and diameter of 6 mm.

In these experiments 100 mL of a solution containing KH_2PO_4 (0.01 M) and NH_4Cl (0.02 M) were placed in the reactor at pH = 7. This was stirred and, once the pH had stabilized, 10 mL of Mg solution, prepared with $MgCl_2 \cdot 6H_2O$, were added with a pipette. Two molarities of Mg were used, 0.01 M and 0.015 M, resulting in two different initial SI values: 0.76 (Block A1) and 0.92 (Block A2), respectively. The mixing intensity was varied from 300 to 800 rpm in 100-rpm increments. In total 12 experimental conditions were evaluated. Each experiment was executed three times. The results included in this chapter are the average of these repetitions, the results with the standard deviations are included in Appendix B. Based on the aforementioned equations, the relationship between the stirring speed and the average shear rate is included in Table 4.1.

Table 4.1: Relationship between the stirring speed and the average shear rate in Experiment A.

Stirring speed (rpm)	Average shear rate (s^{-1})
300	204
400	313
500	436
600	571
700	719
800	876

4.3.2.2. Experiment B

For Experiment B, a 1000-mL stirred reactor was used. Its inner diameter was 100 mm, with rounded corners at the base of the reactor. The PBT stirrer was situated 1 cm above the bottom of the reactor. The reactor was stirred between 200 and 400 rpm, leading to calculated average shear rate as shown in Table 4.2.

Table 4.2: Relationship between the stirring speed and the average shear rate in Experiment B.

Stirring speed (rpm)	Average shear rate (s^{-1})
200	150
300	276
400	425

In all the experiments, 500 mL of a solution, prepared from NaH_2PO_4 and NH_4Cl, were charged in the stirred reactor. Once the pH stabilized, 250 mL of a Mg solution, prepared using $MgCl_2 \cdot 6H_2O$, were added over a 15-s duration. All solutions were prepared with ultrapure water.

The impact of SI was analysed by varying the initial concentrations of all species and pH. All experiments employed a 1:1.5:2 molar ratio for P:Mg:N. Two P concentrations were used: 0.03 M and 0.012 M. These P concentrations, while relatively high if compared with conditions encountered in WRRFs, were used to identify the extent of primary homogeneous nucleation in the experiments, following the work done in Chapter 3. In addition, these conditions are similar to real reactors where a high local SI is present, such as near the feed points or in inefficiently mixed regions.

The experimental runs performed are shown in Table 4.3. In order to present average results, they were grouped into three main blocks, corresponding to their average initial SI: Low SI (B-LSI), Medium SI (B-MSI) and High SI (B-HSI), which corresponded to a SI equal to 2.10, 2.57 and 2.96, respectively. In the runs marked with 'NaOH addition', once equilibrium had been reached, the pH and thus the SI were increased by the addition of a known volume of a NaOH solution. This elicited a subsequent positive supersaturation in the solution, resulting in a new pH decay and change in the PSD under situations where crystals were already suspended in solution (i.e. seeded experiments).

4.3.3. Measurements

The following measurements were taken in the experimental runs.

- pH evolution and induction time.
- PSD measurements in Experiment B.
- Photomicrographs.

4.3.3.1. pH evolution and induction time

From the measurement of the pH evolution, the induction time was estimated. The pH was monitored using an InPro® 3030/120 (InPro® 3030/120, Mettler-Toledo GmbH, Switzerland) in Experiment A and an Orion™ 8175BNWP ROSS™ Sure-Flow™ pH Electrode (Orion™ 8175BNWP ROSS™ Sure-Flow™ pH Electrode, Thermo Fischer Scientific, USA) and an Orion™ 8156BNUWP ROSS Ultra™ pH Electrode (Orion™ 8156BNUWP ROSS Ultra™ pH Electrode, Thermo Fischer Scientific, USA) in Experiment B. The induction time is considered to be inversely proportional to the nucleation rate (Hanhoun *et al*., 2013). In the experiments here described, the induction time was calculated as the time elapsed between the first stable pH obtained and a decrease of 0.05 units of pH (Mehta and Batstone, 2013).

4.3.3.2. PSD measurements in Experiment B

PSD was measured periodically during the experimental runs of Experiment B, using a Multisizer 4 Coulter Counter (Multisizer 4 Coulter Counter, Beckman Coulter, USA). A 1000-µm aperture tube was chosen for the measurements, which could size and count particles between 20-600 µm of spherical volume equivalent diameter. Measurements were done by sampling 5 mL of suspension with a Pasteur pipette from the precipitation reactor. Unless indicated otherwise, all samples were taken in the same point, 4.5 cm from the bottom of the reactor. The sample was transferred to the measuring vessel of the Multisizer 4 Coulter Counter, already filled with electrolyte eluent. The measurements in the Multisizer 4 Coulter Counter are based on the electric zone sensing method, which requires an electrolytic solution for the measurements.

For this study, the electrolytic solution was prepared with ultrapure water, with 0.9% in mass of NaCl that was saturated in struvite. For the saturation, an excess of

previously crystallized struvite was diluted in a 2-L Schott Duran bottle for at least 4 hours. After saturating, the electrolyte was filtered with 0.45 µm paper.

The control mode in the measurements of the Multisizer 4 Coulter Counter was the measuring time (7 s) and the current and gain were 3200 µA and 1, respectively. All samples were measured in duplicate and the results shown are the average of both measurements.

In order to relate the change in the PSD with the effect of local mixing intensity and the SI and not to other physico-chemical effects, a number of preliminary issues were considered for the PSD measurements in Experiment B:

1. Repeatability of the measurements.
2. Avoiding particle settling at the bottom of the reactor.
3. Homogeneity of the particle distribution within the reactor.
4. Particle behaviour under SI = 0 condition.

Experimental runs performed for this analysis are included in Table 4.3 as Block MQ (measurements quality) and the results are given in Appendix B.

4.3.3.3. Photomicrographs

Photomicrographs of the resultant precipitates were taken for both experiments. In Experiment A, the photomicrographs were taken after filtering and drying the solid at 40 °C using scanning electron microscopy (Philips XL30CP Scanning Electron Microscope, Philips, Netherlands). In Experiment B the photomicrographs were taken of liquid samples with a binocular microscope (Nikon Eclipse E-100 Binocular Microscope, Nikon, Japan).

Table 4.3: Experimental runs in Experiment B, divided into four different blocks: Measurements quality (MQ), Low SI (B-LSI), Medium SI (B-MSI) and High SI (B-HSI).

Block	Run	P Conc (mol/l)	N-P pH	Mg pH	Stirring speed (rpm)	NaOH addition
MQ	1	0.03	8.00		90	
	2	0.03	8.00		90	
	3	0.03	8.00		90	
	4	0.012			140	
	5	0.012			180	
	6	0.012			180	
	7	-	-	-	300	
	8	-	-	-	250	
B-LSI (SI = 2.10)	9	0.012	8.11	7.09	200	
	10	0.012	8.05	7.04	200	
	11	0.012	8.14	7.73	300	
	12	0.012	8.03	6.85	300	
	13	0.012	8.02	7.47	400	
	14	0.012	7.97	7.00	400	
	15	0.012	8.06	5.55	300	
	16	0.012	8.07	5.53	300	
	17	0.012	8.11	5.68	200	X
	18	0.012	8.20	5.56	300	X
	19	0.012	8.06	5.58	400	X
B-MSI (SI = 2.57)	20	0.03	7.79	5.23	300	
	21	0.03	7.85	5.29	200	X
	22	0.03	7.73	5.17	300	X
	23	0.03	7.80	5.31	400	X
	24	0.03	7.73	5.49	200	
	25	0.03	7.74	5.53	300	
	26	0.03	7.75	5.48	200	X
	27	0.03	7.72	5.51	300	X
	28	0.03	7.72	5.50	400	X
B-HSI (SI = 2.96)	29	0.03	8.05	8.25	200	X
	30	0.03	8.05	8.21	300	X
	31	0.03	8.05	7.96	400	X

4.4 RESULTS AND DISCUSSION

4.4.1. Induction time

The induction times were experimentally determined from the pH measurements. Strictly, the induction time is the period between the establishment of the supersaturation and the formation of the first stable nuclei. This is not a straightforward measurement and it strongly depends on the measurement technique (Hanhoun *et al.*, 2013). In this thesis, the induction time was considered as the time taken for the pH to change 0.05 units, as previously done (Mehta and Batstone, 2013). This pH-change approach is a relatively accessible way to assess nucleation, but will inevitably include some particle growth. Despite the fact that nucleation is a stochastic process (Nappo *et al.*, 2018), trends could be observed when analysing the effect of the different SI and mixing intensities in the induction times of the Experiment A and Experiment B.

4.4.1.1. Effect of the SI

Figure 4.1 shows the inverse of the induction time ($1/t_{ind}$) against the SI for each experimental condition (chemical and stirrer speed) in this contribution. When data from the same experiment was compared, the induction time was inversely proportional to the SI. This was expected from classical nucleation theory for homogeneous nucleation (Mullin, 2001). In addition, linear relationship for $\log t_{ind}$ vs. $1/(\log S_r)^2$ (Mehta and Batstone, 2013; Ohlinger *et al.*, 1999), for $\ln t_{ind}$ vs. $1/(\ln S_r)^2$ (Hanhoun *et al.*, 2013) and for $1/SI^2$ (Bhuiyan *et al.*, 2008a) have already been proposed in the literature for struvite.

Since $SI = \log(S_r^{\ 3})$, these linear relationships were included in Figure 4.1 for comparison. Interestingly, Figure 4.1 shows that the data from Experiment A, Experiment B and literature are not comparable. In particular, induction times from B-LSI and A1 were similar, while their supersaturation was very different. This meant that, despite being important, the supersaturation was not the only factor affecting the induction time. This could be expected as other studies confirm that experimental conditions, such as the shear rate (Bhuiyan *et al.*, 2008a; Liu and Rasmuson, 2013; Ohlinger *et al.*, 1999), reactor volume (Steendam *et al.*, 2018), temperature (Liu *et al.*, 2014), agitator type (Liu *et al.*, 2015) or the presence of

baffles in the reactor (Liu *et al.*, 2015), affect the induction time of a nucleation process. In the next section the effect of the shear rate is analysed.

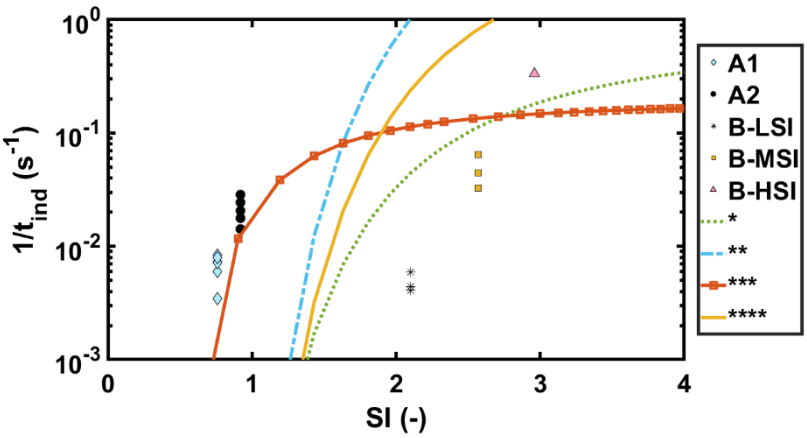

Figure 4.1: Effect on the induction time of the saturation index for the experimental conditions of this contribution and comparison with the results from Mehta and Batstone (Mehta and Batstone, 2013) (*) , Hanhoun *et al.* (Hanhoun *et al.*, 2013) (**), Ohlinger *et al.* (Ohlinger *et al.*, 1999) (***) and Bhuiyan *et al.* (Bhuiyan *et al.*, 2008a) (****).

4.4.1.2. Effect of the shear rate

Results included in Figure 4.2 show that for cases with the same SI, for shear rates under 600 s^{-1}, the increase in the mixer rotation speed, and the consequent increase in the shear rate, meant a shorter induction time for both Experiment A and Experiment B. This result agreed well with the existing literature (Ariyanto *et al.*, 2014; Bhuiyan *et al.*, 2008a; Ohlinger *et al.*, 1999) and was consistent with theory: applying more energy to the system enhances homogeneous nucleation, overcoming the energy barrier and generating stable nuclei. Thus, higher shear rate would promote the generation of stable nuclei and would result in shorter induction times, because of an increased primary homogenous nucleation rate. The same effect of the shear rate in the nucleation rate was observed in the literature in very different experimental conditions (Bhuiyan *et al.*, 2008a; De Santis *et al.*, 2016; Forsyth *et al.*, 2016)

When the shear rate increased over 600 s^{-1} in blocks A1 and A2, the induction time was not further reduced. Bhuiyan *et al.* had similar results, once a determined shear

rate value was reached in their experiment (Bhuiyan *et al*., 2008a). A higher shear rate favours the diffusion of the reactants, accelerating the homogeneous nucleation until some extent, but once a specific value is reached, attrition is favoured, generating counter effects in the nucleation rate (Mullin and Raven, 1962).

Despite the shear rate correlates to the experimental induction times observed, thus partially predicting this phenomenon, the addition of the SI as another potential effect does not fully explain the data from the different experiments. Therefore, more research is needed to fully delineate the struvite nucleation mechanism dependencies.

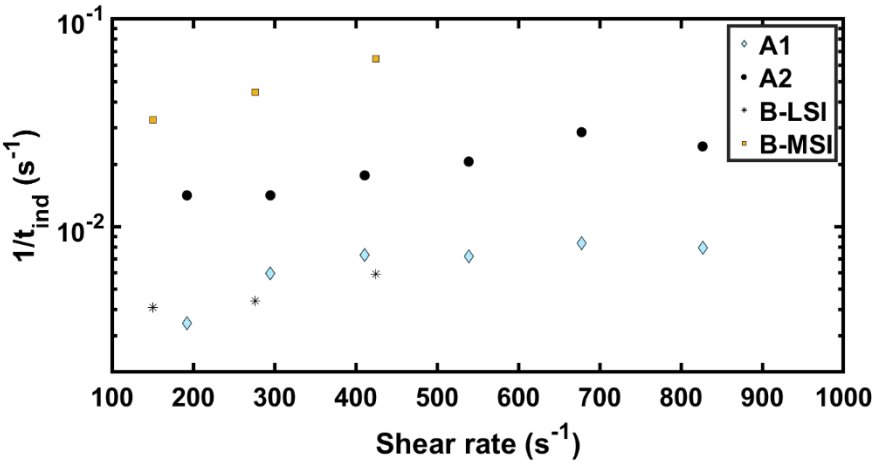

Figure 4.2: Effect of the shear rate on the induction time for the blocks of Experiment A and B.

4.4.2. pH evolution

The analysis of the dependence of the induction time on both the SI and the shear rate helps to understand how these two variables affect to the earliest stages of struvite precipitation, where nucleation is considered to be the dominant mechanism. However, as precipitation in the batch test proceeds, particle enlargement becomes important. During particle enlargement, reactants are consumed from the liquid and transferred to the solid phase and, in batch tests, this phenomenon results in a pH decay until equilibrium is reached.

4.4.2.1. Effect of the SI

Figure 4.3 shows the pH evolution for selected runs of each block of Experiment A and B. Runs selected are the ones with the lowest stirrer speed (300 rpm for Experiment A and 200 rpm for Experiment B).

A higher initial SI introduces more crystal embryos into suspension (as it will be further discussed in 4.4.3. section), as a consequence of an enhanced nucleation. Therefore, runs with the highest SI have greater specific surface area upon which crystals can grow. In addition, struvite growth is proportional to the SI (Bhuiyan *et al.*, 2008b; Galbraith *et al.*, 2014; Hanhoun *et al.*, 2013; Triger *et al.*, 2012). Both effects related with a high SI accelerate the transformation of the dissolved species into struvite crystals. The consequence of both effects can be observed in Figure 4.3, where the pH decay speed aligned well with the SI, as the runs had an increasingly sharper decay as their initial SI augmented (in an ascendant order: A1, A2, B-LSI, B-MSI and B-HSI).

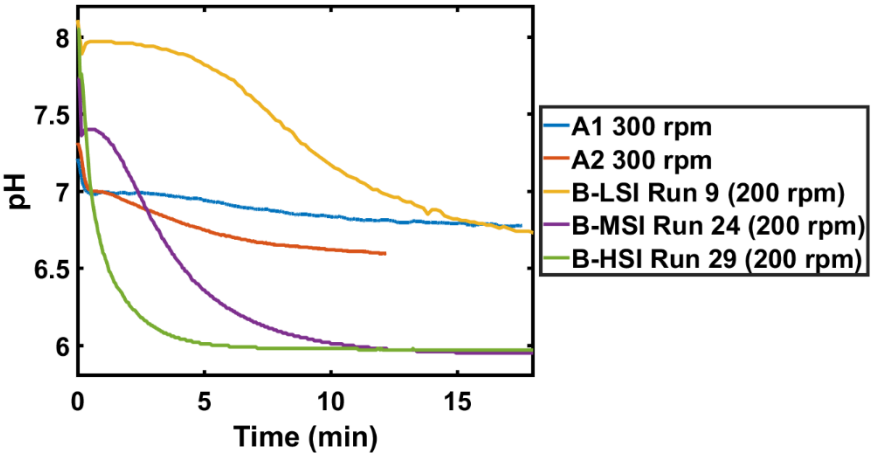

Figure 4.3: Effect of the shear rate on the induction time for the blocks of Experiment A and B.

4.4.2.2. Effect of the shear rate

Among the experimental runs with the same initial SI, higher stirrer speeds led to faster pH decay. While the initial and final pH values depended on the initial chemical conditions, as they are related to the thermodynamics of the process, how fast the equilibrium was reached depended on the stirrer speed. This trend was

especially noteworthy in the experiments with low SI (blocks A1, A2 and B-LSI), as can be seen in Figure 4.4 and Figure 4.5.

Once nucleation took place, particle enlargement (i.e. growth and/or aggregation) followed. Since an increasing growth rate for increasing shear rate has been reported in the literature (De Santis *et al*., 2016; Forsyth *et al*., 2016), this might explain the more rapid pH decay observed for the high mixing rate experiments. On the other hand, kinetic expressions where the aggregation rate is inversely proportional to the shear rate have been already proposed (Hounslow *et al*., 2013). An increasing growth rate and decreasing aggregation rate with the shear rate, combined with the enhanced nucleation suggested by the analysis of the induction times, could explain the faster decay of the pH. However, as the pH decay in the system due to growth of the particles is subject to the number of particles generated in the nucleation step, the effect of the shear rate on the growth process is still uncertain. This effect is further assessed in Chapter 5, by comparing the effects of mixing in nucleation and growth using mathematical tools.

Results from Experiment A, in Figure 4.4 (a,b), show that changing the stirrer speed has a greater effect at lower stirrer speeds, as the pH decay in the experiments with 300 and 400 rpm is significantly slower than in the rest. According to the obtained results, once a certain value is reached, the shear rate has not a clearly discernible impact. As it happened for nucleation, it is logical to expect that the increase in the shear rate favoured the diffusion of the reactants to the reacting surface of the particle, accelerating precipitation, but once a certain shear rate level is reached, increasing it has no effect or even has negative effects on crystal growth, due to attrition.

In Experiment B, increasing the stirring speed also accelerated the runs, especially the B-LSI block. In the B-HSI block, where SI is higher, the precipitation process is dominated by the SI and the effect of the shear rate is not evident (see Figure 4.5).

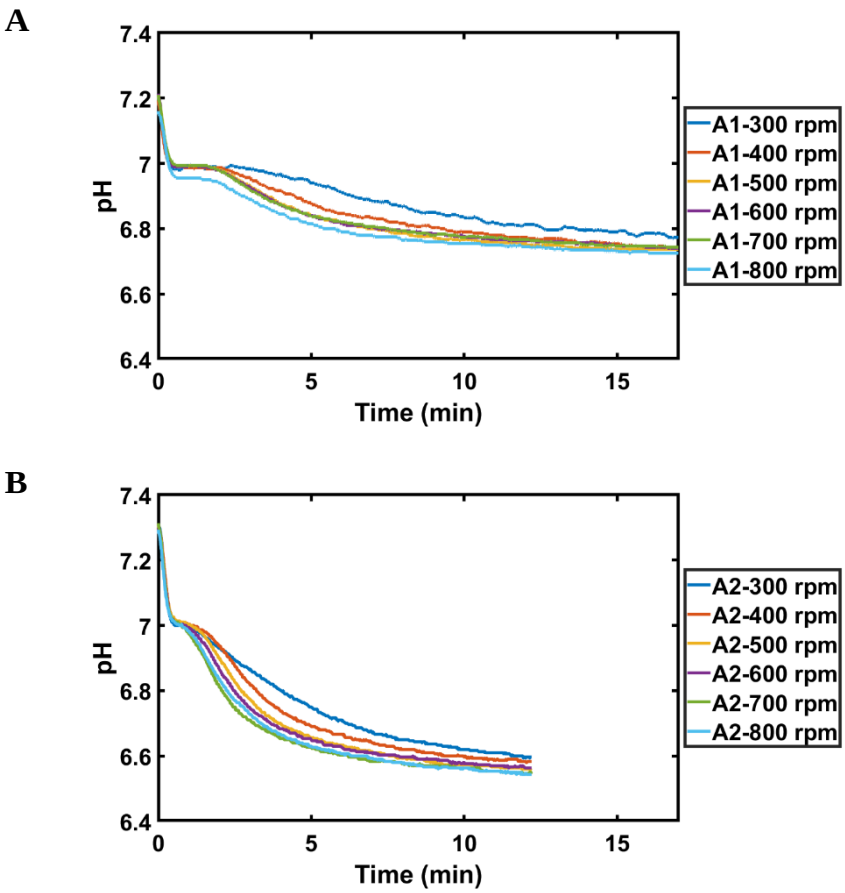

Figure 4.4: Effect of the shear rate on the pH evolution for experimental runs in Block A1 (a) and Block A2 (b).

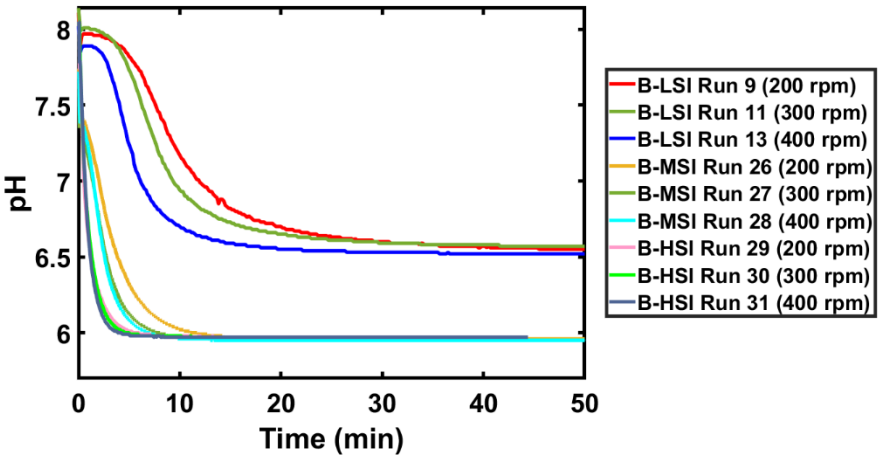

Figure 4.5: Effect of the shear rate on the pH evolution in some runs of Experiment B.

4.4.2.3. Effect of the NaOH addition

In some of the experimental runs of Experiment B, NaOH was added once equilibrium had been reached. This generated a non-equilibrium condition in a system where particles were already suspended.

In runs 17-19 of B-LSI Block, 5 mL of a 0.5 M NaOH solution were added once equilibrium was established. As it is observed in the pH evolution of Figure 4.6 (a), the induction time when the NaOH solution is added is shorter than at the beginning of the experiment for all the runs, despite the saturation being lower. This effect is a consequence of having particles in the solution and suggests that the relevant mechanisms could be secondary nucleation and/or growth, as they are related with the availability of crystals in the solution.

This effect is repeated in the runs 21-23 and 26-28 of the MSI Block. In runs 21-23, 10 mL of the 0.5 M NaOH solution were added once, while in runs 26-28, 5 mL of the 0.5 M NaOH solution were added at two different times. The pH increase was bigger in the runs where the 10 mL were added. As the supersaturation generated in runs 21-23 was bigger than in runs 26-28, the decay was also sharper (see Figure 4.6 (b)).

In every case, runs with the lower stirrer speed took longer to reach the new equilibrium. This is a combination of two effects: on one hand, higher stirrer speeds lead to enhanced diffusion of the reactants to the reacting surface, as reported in

subsection 4.4.2.2., on the other, as it is further explained in section 4.4.3., runs with lower stirring speed have fewer, larger particles. As the total mass of suspended crystals is the same for experiments with the same initial chemical conditions, this turns out as less available surface from which particles can grow, slowing the precipitation process.

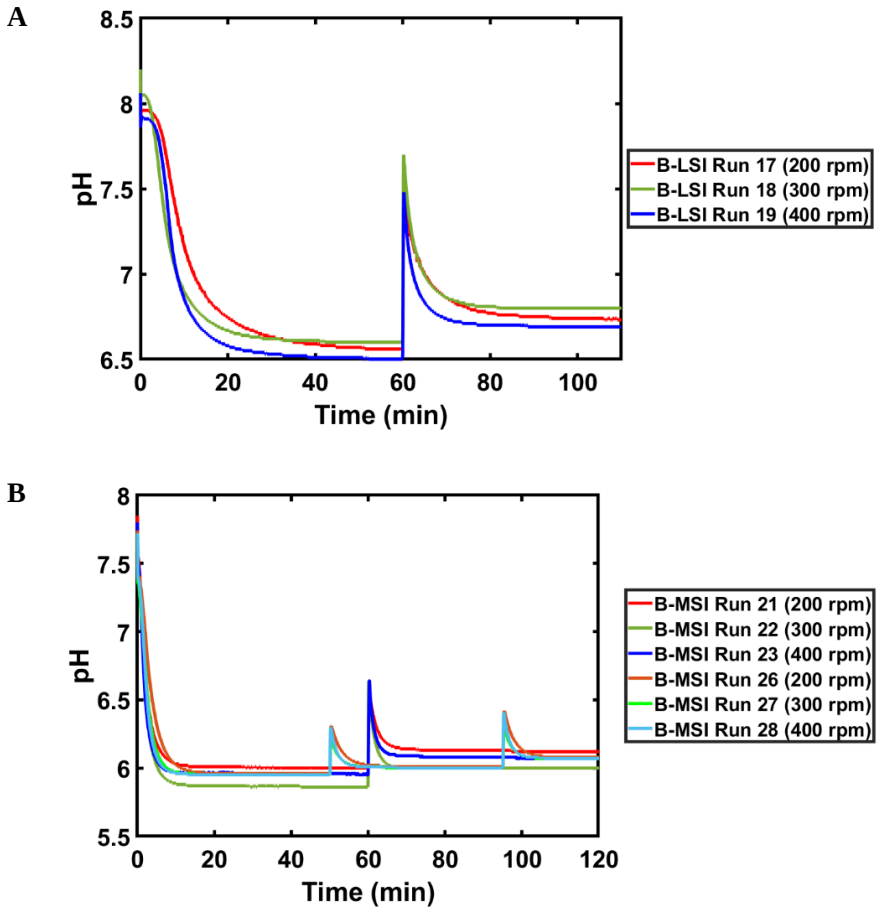

Figure 4.6: Effect of the NaOH addition in the pH evolution of selected runs of Block B-LSI (a) and Block B-MSI (b).

4.4.3. PSD measurements in Experiment B

The experiments performed in the MQ block uncovered the limitations of the PSD measurements. From these measurements, it was concluded that the reactor in Experiment B was well mixed in the macro scale and that all the changes in the PSD could be linked with a change in the measured pH. The results of the MQ block are included in Appendix B.

4.4.3.1. Particle number at equilibrium

The number of particles measured in the experiments gave a good insight about the precipitation process. In this subsection, the average particle count at equilibrium for all the experimental runs performed in Experiment B are shown. Equilibrium values were considered those measured after 25 min of experiment in the B-LSI block and after 20 min in the B-MSI and the B-HSI blocks.

4.4.3.1.1. Effect of the SI

An increasing SI in the system was related with a shorter induction time for both systems studied in this contribution in section 4.4.1.1. due to a favoured nucleation mechanism (see Figure 4.1). This relationship was confirmed in the particle number measurements. Figure 4.7 relates the induction time and the total particle count measured in the equilibrium for every run of Experiment B. Three clear blocks are distinguished, associated with the different SI in the system. The results observed confirm that the nucleation can be related with the induction time, as more particles are obtained for shorter induction times, as a consequence of a higher SI.

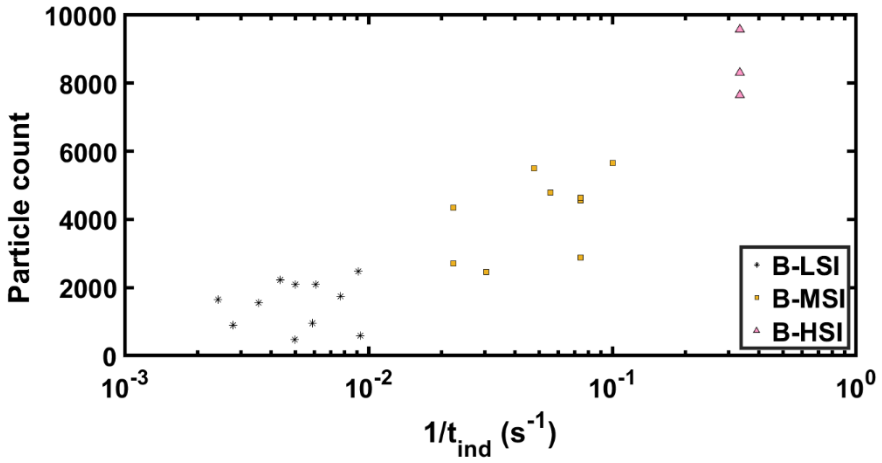

Figure 4.7: Relationship between the average particle count and the inverse of the induction time on each experimental run in Experiment B.

4.4.3.1.2.Effect of the shear rate

As it happened for the SI, an increasing shear rate was related with a shorter induction time in section 4.4.1.2 for Experiment B, due to a favoured nucleation mechanism (see Figure 4.2). Again, this relationship was confirmed in the particle number measurements. As observed in Figure 4.8, the number of counted particles increased with the shear rate when experiments with similar initial chemical conditions were compared. The only exception was the B-HSI block, where the highest shear rate had the lowest particle number average. As this experiment had the highest SI and shear rate, nucleation mechanism was very important. As it will be further discussed in section 4.4.3.2 this lead to a great number of small particles that could be under the detection limit of the equipment.

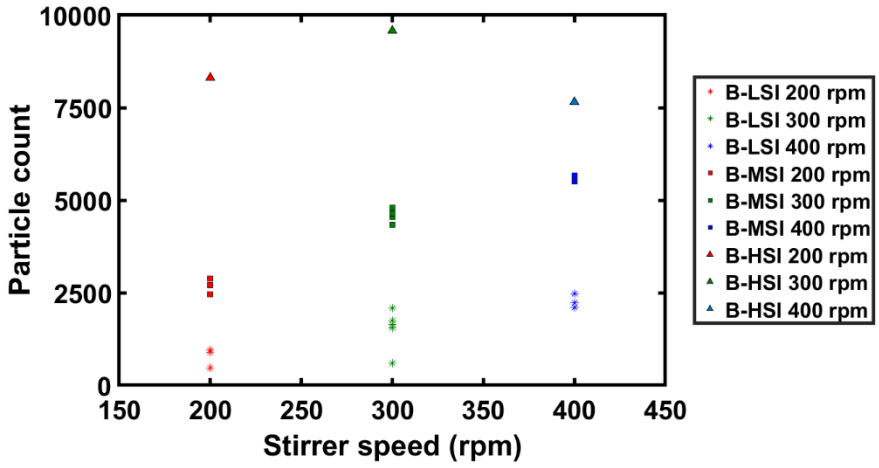

Figure 4.8: Relationship between the average particle count and shear rate for each experimental run in Experiment B.

4.4.3.2. PSD at equilibrium

Figure 4.9 shows the average of the PSD measurements at equilibrium for the B-LSI, B-MSI and B-HSI blocks. The results are presented as average values of every experimental run of each block for the d10, d50 and d90 (diameters that comprise the 10%, 50% and 90% of the particle number in the sample with a diameter less than each value, respectively).

4.4.3.2.1. Effect of the SI

The d10 values were similar for the results of the different blocks, despite the different initial SI. This was reasonable, since the detection limit of the equipment (30 µm, to avoid noise measurement near the limit of 20 µm) was near the d10 value.

Comparing B-LSI and B-MSI blocks, d50 and d90 values were higher in the B-MSI block than in the B-LSI block. A higher SI promoted nucleation, but once nuclei were generated they began to grow, a mechanism that is also favoured at high SI. The competition between both mechanisms depends on the SI, on the shear rate and on the available surface of the crystals. Despite there being more nuclei in the system, the reactants concentration was greater in the liquid for B-MSI block compared to B-LSI block, which resulted in larger particles.

When comparing the results between the B-MSI and the B-HSI block, the opposite effect was observed. In the case of the B-HSI, the higher SI promoted nucleation, which likely dominated growth. In the initial steps of the precipitation process in the experiments of the B-HSI block, more nuclei were created from which more particles grew, providing a faster reactant consumption, as it was seen in the shorter induction times and sharper pH decay that the experiments in this block had when compared with the other blocks. This, ultimately led to smaller particle populations than in B-MSI, as it was confirmed in the d90 value, which was considerably smaller in the B-HSI than in the other two blocks.

4.4.3.2.2. Effect of the shear rate

In every experimental block, for similar initial thermochemical conditions, a higher stirrer speed led to a lower mean particle size at equilibrium as it is shown in Figure 4.9.

This trend was in agreement with the results obtained in (Fang *et al.*, 2016) and was consistent with the induction times, the pH evolution measured in the experiments and the counted particles: as a higher stirrer speed favoured the formation of more nuclei, more points where crystals could start to grow were available, resulting in a shorter induction time, a faster pH decay due to the greater availability of crystal surface to grow and a smaller ultimate mean size of the particle population.

The effect of the stirrer speed on the B-HSI runs was lower than in the rest of the experiments. This effect is also in good agreement with the small differences seen in the pH decay speed for the experiments with the highest SI and the counted particles. According to the obtained results, when the SI is very high, its effect in the precipitation process is dominant over changes related with the shear rate. These results could be compared with other experimental set ups, as similar results were obtained by Zauner and Jones when compared the average size of particles in semi-batch experiments when introducing a high concentration and low concentration feed in a reactor: when increasing the dissipated energy in the reactor, the low concentration feed had a decreasing average size while in the experiments with a high concentration feed the average size was constant (Zauner and Jones, 2000b).

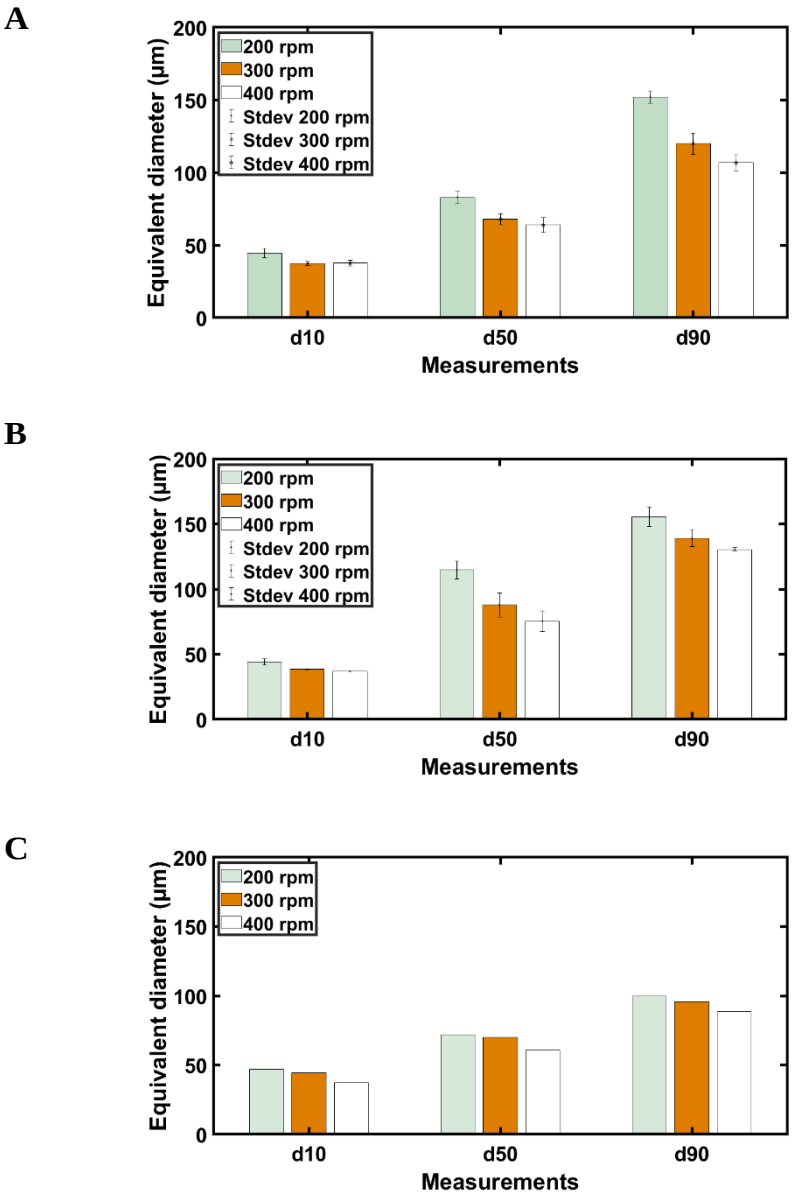

Figure 4.9: Average and standard deviation for d10, d50 and d90 in B-LSI set (a). Average and standard deviation for d10, d50 and d90 in B-MSI set (b). Average of d10, d50 and d90 in B-HSI set (c)

4.4.3.2.3.Effect of the subsequent NaOH addition

In experimental runs were NaOH was added after the onset of equilibrium, the PSD measured before and after the additions could be compared. The generation of a new supersaturation in a system where crystals were already present helped to evaluate the change in the PSD in a situation where particle enlargement mechanisms (mainly growth and secondary nucleation) should dominate.

After analysing the change in the PSD due to these additions in runs 17-19, 21-23 and 26-28, it could be concluded that the change was more significant in the processes with the lowest stirrer speed (200 rpm). According to the obtained measurements, experimental runs with the lowest stirrer speed had initially bigger and fewer particles in the reactor. Therefore, the newly generated supersaturation reaches the equilibrium by dividing its effect in less particles, making the changes more noticeable. As an example, the changes in the PSD due to the additions of NaOH in runs 26-28 are included in Figure 4.10.

In Figure 4.10, starting from the moment Mg solution was added to the system, PSD measurements at times 90 s, 25 min, 85 min and 125 min are shown. NaOH was added twice to the system: 50 min and 95 min after the experiment started (see Figure 4.6 (b)). Comparing the PSD at 90 s (equilibrium was not reached yet) for the different stirrer speeds, it is seen how the run with the highest stirrer speed (Figure 4.10 (c)) has bigger particles, due to a faster reaction. However, when the first equilibrium is reached (PSD at 25 min), the biggest particles measured are in the run with the lowest stirrer speed (Figure 4.10 (a)). PSD measurements at 85 and 125 min show the distribution at the second and third equilibriums. Again, the experiment with the lowest stirrer speed contains bigger particles.

An addition of NaOH could have also generated a localized high SI zone in the reactor, where homogeneous nucleation could be favoured. However, this was not the case for any of the runs as, the d10 was consistent and an enlargement of the particles was observed in every case.

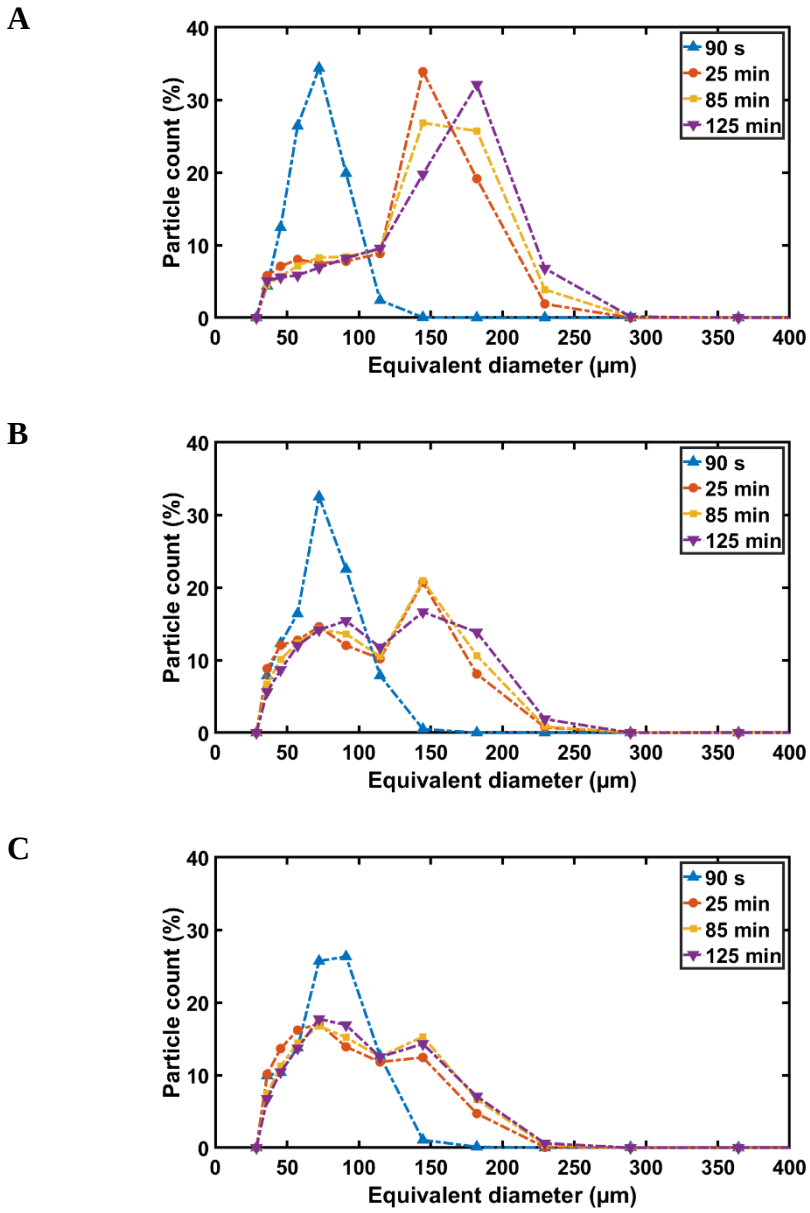

Figure 4.10: Effect of the subsequent NaOH addition in the PSD for experimental runs 26 (200 rpm) (a), 27 (300 rpm) (b) and 28 (400 rpm) (c) of the B-MSI Block.

4.4.4. Photomicrographs

Photomicrographs helped to understand the evolution of the precipitation process. In Figure 4.11 and Figure 4.12, the photomicrographs of runs performed in Experiment A and Experiment B, respectively, are included.

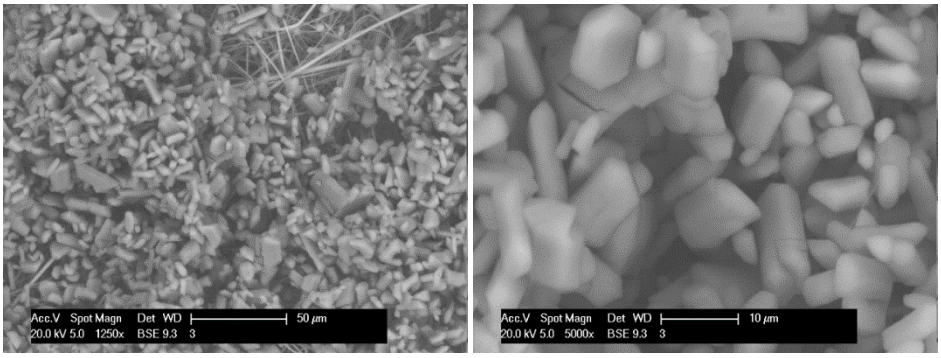

Figure 4.11: Scanning electron microscopy photomicrographs of experimental runs in Experiment A.

Shape of struvite particles has previously been related with the pH (Prywer *et al*., 2012) and the supersaturation (Shaddel *et al*., 2019). The crystal shapes observed in this contribution are consistent with those results, as particles of Experiment A were similar to the shape of particles previously observed for low pH and supersaturation and the shape of particles of Experiment B was similar to the ones obtained at high pH and supersaturation.

Regarding the size of the obtained crystals, size of the crystals in Experiment A is considerably smaller than the size of the particles of Experiment B. A probable explanation is that despite the less favoured nucleation in Experiment A, related with the long induction times, due to the low concentration of the reactants in the solution particles could not grow bigger afterwards.

Photomicrographs of Experiment B are shown in Figure 4.12. For the B-LSI block, leaf-shape dendritic crystals were obtained, in combination with contact and penetration twins (see Figure 4.12 (a) and (b)). For B-MSI block, mainly X-shaped and leaf crystals were obtained. The irregularities observed in the surface of the crystals seen in Figure 4.12 (c) and (d) could be a consequence of a secondary nucleation process generated by the new supersaturation created by the NaOH addition. Photomicrographs from HSI (Figure 4.12 (e) and (f)) block showed that

crystals nucleated and grew independently and that secondary nucleation or aggregation were not favoured, mainly obtaining X-shaped crystals. Despite the leaf-type crystals are related with the highest supersaturation and pH in the literature (Prywer *et al*., 2012; Shaddel *et al*., 2019) in the results obtained in this thesis this was not the case. In addition, not such a clear distinction could be made in the obtained particles, having them often a mixture of shapes in the same experiment.

According to the photomicrographs obtained, crystal aggregation, understanding it as the stable bonding of two already formed crystals, was not the main mechanism occurring. Most of the photomicrographs showed monocrystals, as a result of a precipitation process dominated by homogeneous nucleation, growth and/or secondary nucleation.

4.4.5. Practical application of the results

The impact of the SI and the shear rate on the particle number and the nucleation mechanism have important consequences for the design and scale-up of precipitation reactors. Under conditions of poor mixing in the reactor, localized zones of high supersaturation would likely result at the feeding points. This would enhance homogeneous nucleation, reducing the mean size of the product particles (Mersmann, 2001). An option to avoid such localized zones could be to increase the stirring speed, favouring mixing at macro scale. However, this effect, under certain conditions might lead to more particles in the system, as observed in the results of this contribution. Consequently, a compromise would be needed between good mixing in the macro scale and an excessive shear rate in order to avoid unwanted nucleation.

The pH measurements for Experiments A and B and the PSD measurements in Experiment B showed that regardless the reactor size or stirrer type, the presence of particles in the solution and changing the mixing intensity and SI in the reactor influenced the evolution of the struvite precipitation in the system. Moreover, the effect of varying these conditions was more noticeable for the lower saturation and mixing intensities, which would be closest to the conditions found in full scale reactors. Presence of particles in a zone with a high local saturation could reduce unwanted nucleation as growth mechanism would be favoured due to the available surface area of crystals. Controlling both the presence of particles in a determined zone of the reactor and the local mixing intensity and SI would help to control the

evolution of the precipitation process and the PSD in the reactor and it could be the key to reduce the presence of fine particles in the reactor.

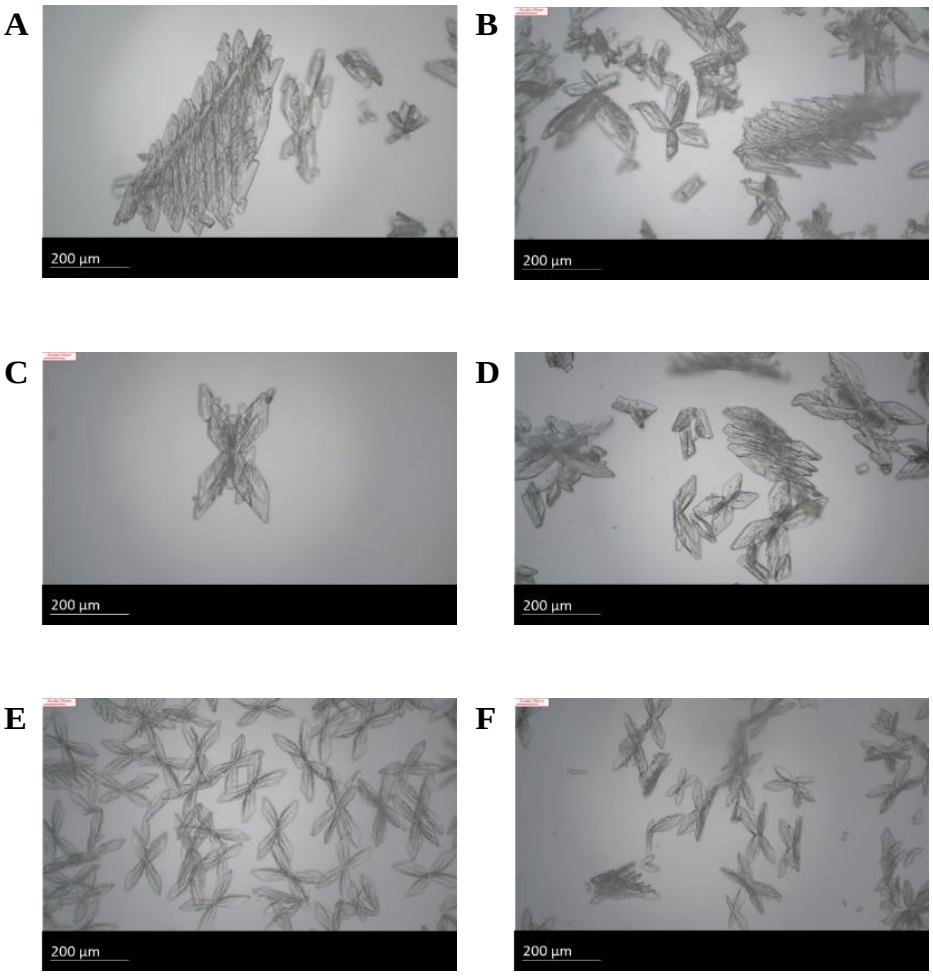

Figure 4.12: Photomicrographs of Experiment B: (a) B-LSI without NaOH addition (300 rpm), (b) B-LSI after NaOH addition (300 rpm), (c) B-MSI after 2 additions of NaOH (300 rpm), (d) B-MSI after 2 additions of NaOH (400 rpm), (e) B-HSI (200 rpm) and (f) B-HSI (400 rpm).

4.5 SUMMARY

The utility of struvite as a sustainable fertilizer and the feasibility of the recovery technology depends on its PSD. The objective of this chapter was to analyse the combined effect of the supersaturation and the shear rate on nucleation and growth mechanisms of the resultant particle populations, since the role of hydrodynamics is unclear and its influence often ignored. As a general trend, higher shear rates favoured homogeneous nucleation, measured through reduced induction times and greater particle number densities. This phenomena led to more rapid precipitation and reduced population mean particle size. Higher SI favoured nucleation and growth mechanism and was related to a faster precipitation process and a greater particle density. According to the obtained results, both variables should be considered in homogeneous nucleation and growth, when the PSD is of importance. The results obtained improve the existing knowledge on the struvite precipitation process and give the necessary data for the calibration purposes of Chapter 5.

CHAPTER 5

INCLUSION OF SHEAR RATE EFFECTS IN THE KINETICS OF A DISCRETIZED POPULATION BALANCE MODEL: APPLICATION TO STRUVITE PRECIPITATION

The content of this chapter has been sent for its revision to Water Research.

5.1 ABSTRACT

The effect of mixing in the modelling of processes based on mass transfer phenomena is commonly ignored in wastewater treatment modelling. In this chapter, the effect of the average shear rate in the nucleation and growth rates of struvite is analysed by combining experimental data from Chapter 4 with simulation results obtained with the mass-based DPBM presented in chapter 3. According to the obtained results, the effect of the average shear rate is identifiable for the selected data and mechanisms.

Therefore, it should be considered when a more detailed modelling of the process is needed. Consequently, in this chapter, the average shear rate has been decoupled from the kinetic constants and kinetic rates where it is explicitly included as a power law function have been proposed. The exponents in these power law functions for the primary homogeneous nucleation and growth are 1.3 and 0.3, respectively. Considering shear rate effects allowed to see in the simulation outputs experimentally observed effects: a faster pH decay and smaller particle distribution for increasing mixing intensities.

5.2 BACKGROUND

For decades, mathematical modelling and simulation tools have been used in the design, operation and optimization of WWTPs (Fernández-Arévalo *et al*., 2017a, 2017b; Lizarralde *et al*., 2019). To date, the main modelling and simulation approach used in WWTPs described complex biochemical and physicochemical reactions, assumed to take place in CSTR (IWA ASM-ADM models) (Batstone *et al.*, 2002; Henze *et al.*, 2000). As a result, these models are independent of the mixing intensity and, consequently, limited in their application and scope for the design and optimization of technologies dependent upon mass transfer phenomena. Unit operations based on mass transfer phenomena are especially important in the emerging conception of WWTPs as WRRFs and upgrading the classic modelling libraries is necessary for the correct description of the processes occurring within (Vaneeckhaute *et al*., 2018). Clearly, accounting for mixing effects in process model development would enhance the understanding of WRRFs' unit processes and would be an important step towards more descriptive modelling (Burns *et al.*, 2021).

Modelling the effect of mixing in wastewater treatment processes is challenging, since it occurs at different process scales: macromixing, mesomixing and micromixing (Torbacke and Rasmuson, 2004). The consideration of the mixing scale compromises the modelling approach needed to represent mixing in the reactors. Macromixing and even meso-scale mixing effects could be associated to the transport of the reactants and different discrete entities (i.e. bubbles or particles) in the system by dividing the reactor into smaller zones or elements, using different approaches such as CFD, compartmental modelling or tanks in series, depending on the required detail. On the contrary, micromixing affects those processes occurring at molecular scale, as nucleation and growth in precipitation systems. Therefore, mixing effects in

the kinetics of precipitation processes, should be studied by considering micromixing (Phillips *et al*., 1999).

In the mechanism's formulation of the discretized PBM presented in Chapter 3, the effect of supersaturation, which combines the effects of concentration of reactants, temperature and pH, is included as a power law function as it is often done in the PBMs representing struvite precipitation (Burns *et al.*, 2021, 2016; Galbraith *et al.*, 2014). Furthermore, the presence of other ions and even seed material can be systematically included in their formulation, if needed. However, the model does not consider micromixing effects, as it often happens in the literature.

Including micromixing effects in the existing PBMs is very challenging, as its effect in the reaction mechanisms is poorly understood (Mao and Yang, 2017). Despite the difficulties, some efforts have been already done. Some authors have studied the interaction between micromixing and kinetics in PBMs by describing different zones in the reactor depending on the micromixing, which is associated with the energy dissipation rate (Baldyga *et al*., 1995; Phillips *et al*., 1999; Pohorecki and Bałdyga, 1983). Other authors have considered an average shear rate in the reactor and explicitly included it in the aggregation rate expressions (Hounslow *et al*., 2013; Vaneeckhaute *et al*., 2018). This approach is also used when modelling flocculation (Nopens *et al.*, 2004). Both possibilities have in common that the precipitation model is applied in environments considered homogeneous from a mixing perspective, as it is recommended in Baldyga *et al* (1995).

In this chapter, the second approach will be used to evaluate the effect of the micromixing on the kinetic rates of the mechanisms constituting the discretized PBM presented in Chapter 3. As aforementioned, this approach has been used to simulate aggregation in PBMs. However, its use to evaluate the shear rate effects in nucleation and growth is not extended. As the shear rate has been related in the literature with the nucleation (De Santis *et al*., 2016; Forsyth *et al*., 2016; Mullin and Raven, 1962; Nappo *et al*., 2018) and growth (De Santis *et al*., 2016) it is believed that its effect in the modelling of these mechanisms should be further studied and, if necessary, included in the kinetic expressions of the PBM describing them. In addition, modelling the shear rate as a process variable may help to obtain parameter values that are independent of the local mixing intensity.

Therefore, the objectives of this chapter are twofold. First, to consider if the average shear rate should be decoupled from the kinetic constants of the mechanisms of the

previously presented PBM, based on the comparison between the experimental data obtained under different saturation and mixing conditions in Chapter 4 and simulation outputs from this chapter. Secondly, if so, to propose new dependency laws for the kinetics of the PBM where the shear rate effect is explicitly included, based on parameter values calibrated using Bayesian Inference for different mixing intensities. The methodology employed could be useful not only to improve the modelling and understanding of struvite precipitation, but also of other unit processes in a WRRF based on mass transfer phenomena, such as biofilm-based processes, granular technologies, aeration, membrane fouling, adsorption or other precipitation processes.

5.3 MATERIALS AND METHODS

This section is divided in two main sections. In the first section, the PBM described in Chapter 3 is briefly re-introduced. Despite its general description and equations have been included in Chapter 3, the model has been adapted to better represent the experimental data obtained in Chapter 4. In the second section, the experimental runs, the simulation studies and the methodology combining both to determine the effect of the shear rate in the kinetics of the PBM mechanisms is explained.

5.3.1. Population balance model

The general description and equations of the PBM are included in Chapter 3. As previously mentioned, the volume size domain was partitioned into 30 different size bins using a 2 geometric progression. Each bin corresponded to the known volume of spherical particles sized between 0.001 and 0.812 mm of radius. The kinetics in the model depend on the value of the SI at any time. This SI value was calculated using Ksp_{Stru}= 7.58x10^{-13} as it has been done throughout the thesis.

The kinetics describing the primary homogeneous nucleation and growth mechanisms were described as follows:

$$B_0 = K_B \cdot SI^{n_B} \cdot V \quad \textbf{5.1}$$

$$G = K_G \cdot SI^{n_G} \quad \textbf{5.2}$$

where B_0 is the particle birth rate due to primary homogeneous nucleation (nuclei/day), K_B (nuclei/(day·m^3)) is the kinetic constant of the homogeneous nucleation (Kr Nucleation), V is the liquid volume in the reactor (m^3), n_B (-) is the Nucleation Exponent, G is the particle linear growth rate (mm/day), K_G (mm/day) is the kinetic constant of growth and n_G (-) is the Growth Exponent.

The model presented in Chapter 3 also included the aggregation mechanism. However, this mechanism was removed from the PBM in the present chapter. As the photomicrographs included in Figure 4.12 in Chapter 4 showed that the particles precipitated in the experiments were single crystals, including this mechanism was not necessary. Moreover, including the aggregation mechanism would mean having more parameters to calibrate, which could lead to identifiability problems and compensation in the parameter values as observed in the results of Chapter 3.

Therefore, considering only the effects of primary homogeneous nucleation and growth in the system, the change in the mass of the smallest bin $\frac{\partial X_1}{\partial t}$ could be described as follows:

$$\frac{\partial X_1}{\partial t} = K_B \cdot SI^{n_B} \cdot V \cdot mesf_1 - K_G \cdot SI^n \cdot A_1 \cdot \rho_S \qquad \textbf{5.3}$$

where $mesf_1$ is the mass (g) of struvite in a single sphere of the smallest bin, A_1 (m^2) the available area of the smallest sized crystals at any time and ρ_S the density (g/m^3) of the crystals.

For the rest of the i bins, the mass change $\frac{\partial X_i}{\partial t}$ is described by the growth:

$$\frac{\partial X_i}{\partial t} = \frac{mesf_i}{mesf_{i-1}} \cdot K_G \cdot SI^n \cdot A_{i-1} \cdot \rho_S - K_G \cdot SI^n \cdot A_i \cdot \rho_S \qquad \textbf{5.4}$$

as the area was not a variable included in the model, it had to be converted to a term depending on mass:

$$A_i = \frac{Cw_i \cdot V}{\rho_S \cdot \Phi \cdot \frac{(L_i + L_{i+1})}{2}} \qquad \textbf{5.5}$$

being Cw_i (g/m^3) the concentration of i-sized particles at any time in, L_i and L_{i+1} the radius (mm) of the ith and i+1th bin, respectively, and Φ a shape factor that relates the volume, the area and the characteristic length of the crystals.

Preliminary simulations (results not included) performed with this model structure showed that the simulation could not faithfully describe the experimental data gathered from experiments in Chapter 4. Therefore, some changes were made to the growth model.

The original model formulation for crystal growth presented in Chapter 3 is valid for an isotropic growth of the crystals, regardless its shape, because in this case Φ is a constant numeric value that can be embedded in the K_G when this is calibrated (as it is done in Chapter 3). However, struvite crystal faces do not necessarily grow equally. As a result, their shapes usually are not spheres or regular polyhedrons, as it has been seen in Chapter 4 or the available literature (Prywer *et al*., 2012; Shaddel *et al*., 2019). Therefore, from the total volume of the particle, the growth rate is proportional only to a portion of its total area. This effect has been addressed in the mathematical model by considering only the effective area of the particle. This has been done elevating to an exponent α (-) the characteristic length. Therefore, the effective area of the crystal, named A_i', becomes:

$$A_i' = \frac{Cw_i \cdot V}{\rho_S \cdot \frac{(L_i + L_{i+1})}{2}^{\alpha}} \qquad \textbf{5.6}$$

If the value of α (-), known as the Area Exponent, is greater than unity, growth for bigger particles is less favoured than for the smaller ones. This change maintains the simplicity of the general PBM structure, as the 2 geometric progression for the partition of the volume size domain and the characteristic lengths associated to each bin are maintained as if the particles were spheres, but the results addressed are more realistic as the growth is only proportional to the effective area of the crystal. However, it added an extra parameter to the calibration procedure.

5.3.2. Analysis of the shear rate effect

The analysis of the effect of the shear rate in the kinetics of the PBM was performed combining experimental results with outputs from simulation case studies. Bayesian inference was used to relate the model outputs to the experimental results, with Figure 5.1 showing the general analysis procedure.

5.3.2.1. Experimental runs

Data from nine experimental runs performed in the Chapter 4 was gathered to experimentally observe the effect of the shear rate in the precipitation. The selected experiments were runs 9, 11 and 13 from the B-LSI block, 26-28 from the B-MSI block and 29-31 from the B-HSI block from the Experiment B (see Table 4.3 in Chapter 4). These nine experimental runs combined three different initial chemical conditions and three different stirring speeds.

As previously explained in Chapter 4, in all the experiments, 500 ml of a solution, prepared from NaH_2PO_4, NH_4Cl and NaOH, were charged in a 1-L vessel stirred with a 5-cm diameter 45º PBT stirrer. Afterwards, 250 ml of a $MgCl_2 \cdot 6H_2O$ solution were added over a 15-second duration. All solutions were prepared with ultrapure water. In all the experimental runs the P:N:Mg molar relation after the mixing of both solutions was 1:2:1.5 (see experimental conditions in Table 5.1).

Measured variables were pH (continuous) and PSD (periodically) with a Beckman Coulter Multisizer 4 (Multisizer 4 Coulter Counter, Beckman Coulter, USA). A 1000-µm aperture tube was employed to measure particles between 20-600 µm of spherical volume equivalent diameter. The electrolyte was prepared with ultrapure water and 0.9 wt% NaCl, which was saturated in struvite to avoid particle dissolution during the measurements. The control mode in the measurements of the Beckman Coulter Multisizer 4 was the measuring time (7 seconds). The current and gain, were 3200 µA and 1, respectively.

Table 5.1: Experimental conditions of the N-P and Mg solutions. Each experiment is a combination of low, medium or high SI (LSI, MSI and HSI, respectively) with a low, medium and high shear rate (Lγ, Mγ and Hγ, respectively).

Experiment	P (mol/l)	N (mol/l)	Initial pH N-P	Mg (mol/l)	Initial pH Mg	Stirring Speed (rpm)	Shear Rate (s^{-1})
Experiment LSI-Lγ	0.018	0.036	8.11	0.054	7.09	200	150
Experiment LSI- Mγ	0.018	0.036	8.14	0.054	7.73	300	276
Experiment LSI- Hγ	0.018	0.036	8.02	0.054	7.47	400	425
Experiment MSI- Lγ	0.045	0.09	7.74	0.135	5.48	200	150
Experiment MSI- Mγ	0.045	0.09	7.72	0.135	5.51	300	276
Experiment MSI- Hγ	0.045	0.09	7.72	0.135	5.50	400	425
Experiment HSI- Lγ	0.045	0.09	8.05	0.135	8.25	200	150
Experiment HSI- Mγ	0.045	0.09	8.05	0.135	8.21	300	276
Experiment HSI- Hγ	0.045	0.09	8.05	0.135	7.96	400	425

5.3.2.2. Simulation case studies

Three different simulation case studies were defined in WEST-DHI, based on the experimental runs shown in subsection 5.3.2.1. The shear rate was not included as a process variable in the simulations, as the original PBM did not include its effect in the kinetics. Therefore, the difference between the simulation case studies was the initial chemical condition. The simulation case studies were named S-LSI, S-MSI and S-HSI, and corresponded to the experimental conditions with low, medium and high SI, respectively (see Table 5.2).

In each of the simulation case studies defined, 500 ml of a solution with the required concentration of NaH_2PO_4 and NH_4Cl were placed in a 1-L capacity reactor. Starting at simulation time t = 0 s, 250 ml of a $MgCl_2 \cdot 6H_2O$ dissolution were added over a 15-second duration, as it was done in the experimental runs. After that, no further external perturbations were introduced. The initial pH in the solutions of each simulation case study is the average of the three experimental runs with the corresponding SI. The SI value was calculated in WEST-DHI, using the equations and guidelines from Lizarralde *et al*., (2015).

Table 5.2: Simulation Case Studies.

Simulation Case Study	P concentration (mol/l)	N concentration (mol/l)	Initial pH	Mg concentration (mol/l)	Initial pH	SI
S-LSI	0.018	0.036	8.09	0.054	7.43	2.10
S-MSI	0.045	0.09	7.73	0.135	5.50	2.57
S-HSI	0.045	0.09	8.05	0.135	8.14	2.96

5.3.2.3. Bayesian inference module

The comparison between the experimental and simulation outputs was done in Matlab using Bayesian Monte Carlo techniques. Its objective was to find a parameter set θ $(K_B, n_B, K_G, n_G, \alpha)$ that could faithfully reproduce the pH evolution and the periodically measured PSD for each mixing intensity to extract dependency laws that related the parameters to the shear rate. The parameters analysed were those included in nucleation and growth rate equations (see Table 5.3).

Table 5.3: List of parameters present in the model with the symbols, units and the kinetic expressions where they are used. $\left.\frac{\partial X_1}{\partial t}\right|_N$ corresponds to the mass change in the smallest bin due to nucleation and $\left.\frac{\partial X_i}{\partial t}\right|_{G_{i\to i+1}}$ corresponds to the mass change from the ith to the i+1th bin due to growth.

Name	Symbol	Description	Units	Kinetic Expression
Kr Nucleation	K_B	Kinetic constant of Nucleation	$\frac{\text{nuclei}}{\text{day}\cdot\text{m}^3}$	$\left.\frac{\partial X_1}{\partial t}\right\|_N = K_B \cdot SI^{n_B} \cdot V \cdot mesf_1$
Nucleation Exponent	n_B	Kinetic Exponent of Nucleation	(-)	
Kr Growth	K_G	Kinetic constant of Growth	$\frac{\text{mm}^\alpha}{\text{day}}$	$\left.\frac{\partial X_i}{\partial t}\right\|_{G_{i\to i+1}} = K_G \cdot SI^{n_G} \cdot \frac{Cw_i \cdot V}{\left(\frac{L_i + L_{i+1}}{2}\right)^\alpha}$
Growth Exponent	n_G	Kinetic Exponent of Growth	(-)	
Area Exponent	α	Area Exponent	(-)	

According to the Bayes Theorem, there is a value of the posterior probability density function associated to each parameter set. This value of the posterior probability density function depends on the prior knowledge of the parameters in the model and the observed data:

$$p(\theta|y) = \frac{p(y|\theta)\cdot p(\theta)}{p(y)} = \frac{p(y|\theta)\cdot p(\theta)}{\int_\theta p(y|\theta)\cdot p(\theta)} \propto p(y|\theta)\cdot p(\theta) \qquad \textbf{5.7}$$

Where $p(\theta|y)$ is the value of the posterior probability density function of the parameter set θ for the experimental data y, $p(\theta)$ is the prior knowledge, $p(y|\theta)$ is the likelihood function and $p(y)$ is the probability of having the observed data, which acts as a normalizing constant in order to express the theorem proportionally (Martin and Ayesa, 2010). The basic idea behind using Bayesian Monte Carlo techniques is that it is enough to have many simulations that can draw approximately the shape of the posterior probability density function $p(\theta|y)$, instead of analytically computing it (Vrugt and Bouten, 2002).

The prior knowledge about the model is defined in the prior probability density function ($p(\theta)$), where the information available about the parameters before any measurement is done is included. In this chapter, this information was the upper and lower value of the range of the parameters to be calibrated. This range was selected based on the results obtained in the sensitivity analysis in Chapter 3 and the available literature and can be seen in Table C.1 in Appendix C. As every parameter value within the range had the same probability to be chosen, the prior probability density function was non-informative.

The likelihood function ($p(y|\theta)$) quantifies the agreement between the measured data y and the answer of the model for each parameter set θ. A higher value in the likelihood function corresponds therefore to a more accurate simulation. Different likelihood functions have been used in the literature (Blasone *et al.*, 2008). Based on (Vrugt *et al.*, 2003), in this contribution the likelihood of a parameter set, θ, to describe the observed data, y, was quantified as:

$$p(y|\theta) = M(\theta)^{-N_M(1+\gamma_B)/2} \quad \textbf{5.8}$$

$$M(\theta) = \sum_{k=1}^{Nobs} |e_k(\theta)|^2 \quad \textbf{5.9}$$

Nobs is the number of observed variables and $e_k(\theta)$ the normalized difference between the measurement of each k^{th} variable and its correspondent simulation output. These differences were normalized in order to give similar weights for the pH and PSD measurements: pH differences were divided by 0.5 and PSD percentage differences by 10. N_M is an adjustable parameter that is used to establish the relative weight for each parameter set. If N_M = 0, the same likelihood is assigned to all parameter sets. When $N_M \rightarrow \infty$, the posterior probability of the mode (the parameter set with the greatest likelihood) will tend to 1, whereas the rest will tend to 0 (Blasone *et al.*, 2008). For the analysis performed here, N_M was fixed at 10. γ_B specifies the error model of the residuals, which were considered normally distributed (γ_B= 0).

The posterior distribution was calculated as follows:

$$p(\theta|y) = \frac{p(y|\theta) \cdot p(\theta)}{p(y)} = \frac{M(\theta)^{-N_M/2}}{\sum M(\theta)^{-N_M/2}} \quad \textbf{5.10}$$

As it is seen in Figure 5.1 the data gathered in the nine experimental runs was classified considering their shear rate. Therefore, the experiments were divided into:

low shear rate (Lγ), medium shear rate (Mγ) and high shear rate (Hγ). Thus, each of the groups had the data obtained from three experimental runs performed with the same shear rate and a different initial SI.

The results from Chapter 3 suggested that the PBM could have identifiability problems. Therefore, in order to reduce the number of parameters to be regressed for each shear rate, the exponents (Nucleation Exponent, Growth Exponent and Area Exponent) were presumed independent of the shear rate and fixed as the first step of the procedure. For the other two parameters (Kr Nucleation and Kr Growth) 1000 parameter values were randomly chosen using the Metropolis Hastings algorithm within previously defined parameter ranges. Each parameter set was named θ_{ij}, corresponding the subscript i to the group with the known and previously fixed exponents and the subscript j to the randomly chosen kinetic constants.

For the parameter set θ_{ij}, a simulation of each simulation case study was performed. The outputs of these simulations ($SIM_{i,j}$) were compared with the corresponding experimental data of each shear rate (Lγ, Mγ and Hγ). From this comparison, a $M(\theta_{ij})_{z\gamma}$value was assigned to each parameter set for each shear rate (being the subscript $z\gamma =$ Lγ, Mγ or Hγ, depending the case). Consequently, three different distributions of the posterior density function (one distribution for each shear rate) were obtained. The goodness of fit of the 1000 simulations from each i group was evaluated with the Total $M(\theta_i)$, understanding Total $M(\theta_i)$ as the sum of the $M(\theta_{ij})_{z\gamma}$ obtained for the best parameter set for each shear rate and θ_i the parameter group formed by the exponents of the i group ($n_{B,i}, n_{G,i}, \alpha_i$) and the three pair of kinetic constants ($K_{B,i,z\gamma}$ and $K_{G,i,z\gamma}$) that best represented the experimental data for each shear rate.

After the 1000 simulations were done and the posterior distributions calculated, new values of the exponents were selected manually and again 1000 randomly selected kinetic constant values were picked. The procedure was repeated until the value of Total $M(\theta_i)$, could not substantially decrease. This procedure was repeated for 21 different exponent value combinations, having in total 21,000 simulations of each case study.

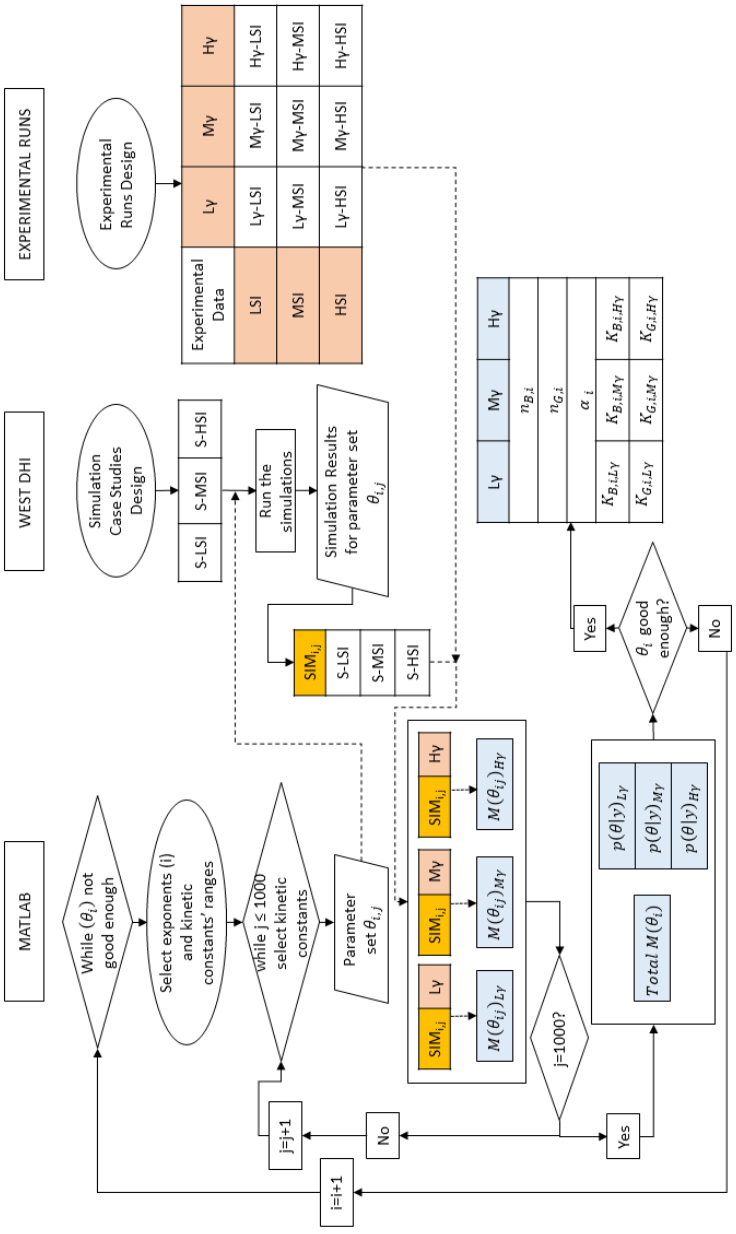

Figure 5.1: General calibration procedure.

5.4 RESULTS AND DISCUSSION

This section is divided into three subsections. In the first subsection, the results of the analysis of the effect of the shear rate in the parameters are provided. In the second a relationship between the shear rate and the kinetic rates is proposed. In the third, the experimental results and the results of the simulated case studies are compared.

5.4.1. Effect of the shear rate in the kinetic constants

Calibration results from the simulation group with exponent values: Nucleation Exponent = 13, Growth Exponent = 2 and Area Exponent = 1.8 were used to analyse the effect of the shear rate in the kinetic constants. The parameter group ($K_{B,i,L\gamma}$, $K_{B,i,M\gamma}$, $K_{B,i,H\gamma}$, $n_{B,i}$, $K_{G,i,L\gamma}$, $K_{G,i,M\gamma}$, $K_{G,i,H\gamma}$, $n_{G,i}$, α_i) calibrated from this group was the one that could overall best describe the experimental data. Best results of the kinetic constants for each shear rate for each group and the calculated Total $M(\theta_i)$ for each group are reported in Table C.2 in Appendix C.

Figure 5.2 includes the posterior density distribution for the Kr Nucleation parameter in the selected simulation group for each of the analysed shear rates. Figure 5.2 (a, c, e) shows the value of the posterior density for each sampled Kr Nucleation value, while Figure 5.2 (b, d, f) is a histogram where parameter range has been partitioned in 15 bins and the value of the posterior density for the points within each bin has been added. As it is observed, the Kr Nucleation parameter is identifiable for every shear rate condition. In addition, the mode of the Kr Nucleation parameter is different for each shear rate. Therefore, the effect of the shear rate in the Kr Nucleation parameter should be decoupled for a more detailed description of the mechanism. Moreover, the posterior density distribution showed a well-defined peak for every shear rate, which meant that the selected parameter range was adequate for the study. The smallest and the biggest values of the Kr Nucleation are related with a too slow or a too fast nucleation rate, respectively. Both possibilities led to a bad representation of the experimental data, according to the obtained results.

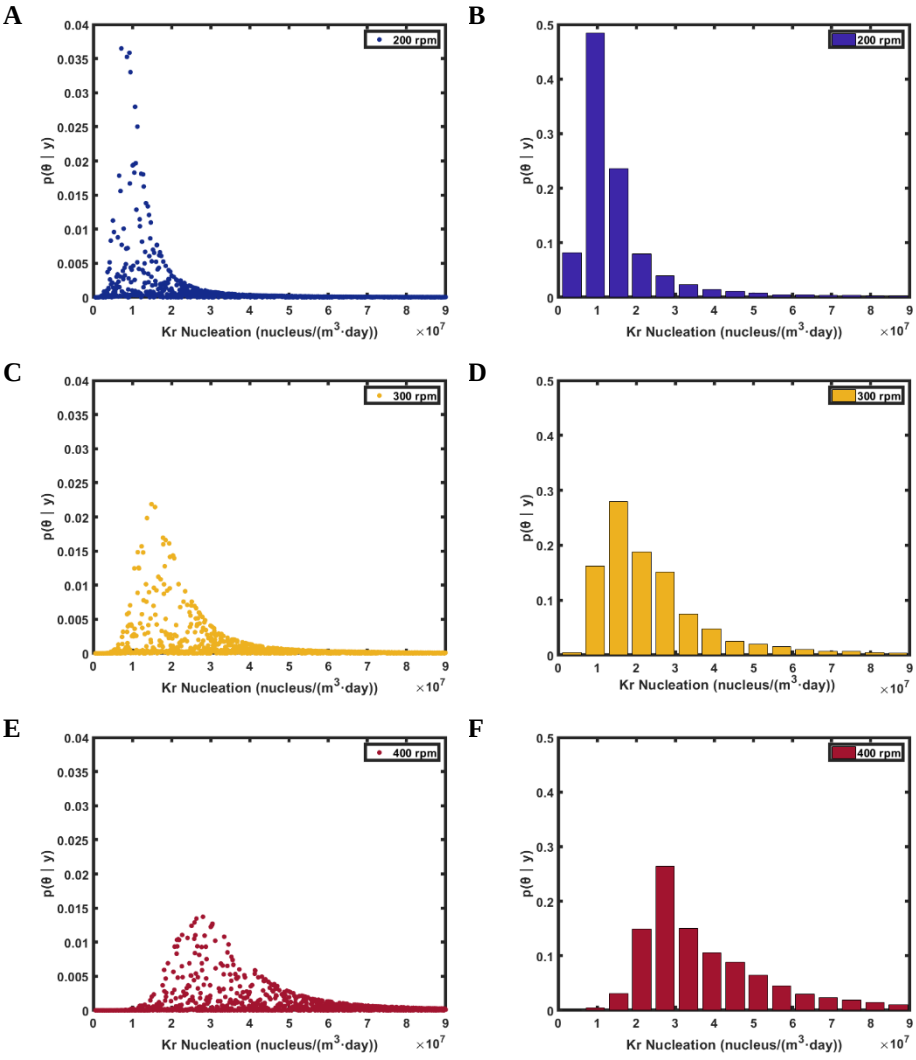

Figure 5.2: Posterior density distribution for the Kr Nucleation for each shear rate. Posterior density values for 200 rpm (a), Histogram of the posterior density for 200 rpm (b), Posterior density values for 300 rpm (c) Histogram of the posterior density for 300 rpm (d), Posterior density values for 400 rpm (e), Histogram of the posterior density for 200 rpm (b).

Analogously to the previously analysed 1000-simulation group, calibration results from each of the other 1000-simulation group (included in Table C.2) showed that the values of the Kr Nucleation that best represented the experimental data obtained with each shear rate increased with the shear rate. In addition, these best Kr Nucleation values were clearly influenced by the pre-selected Nucleation Exponent value (see Figure 5.3). Even if the effect of both parameters on the simulation output is not the same, the best values of the Kr Nucleation were smaller as the Nucleation Exponent increased. Therefore, there was a compensation effect between both parameters for the type and amount of data used.

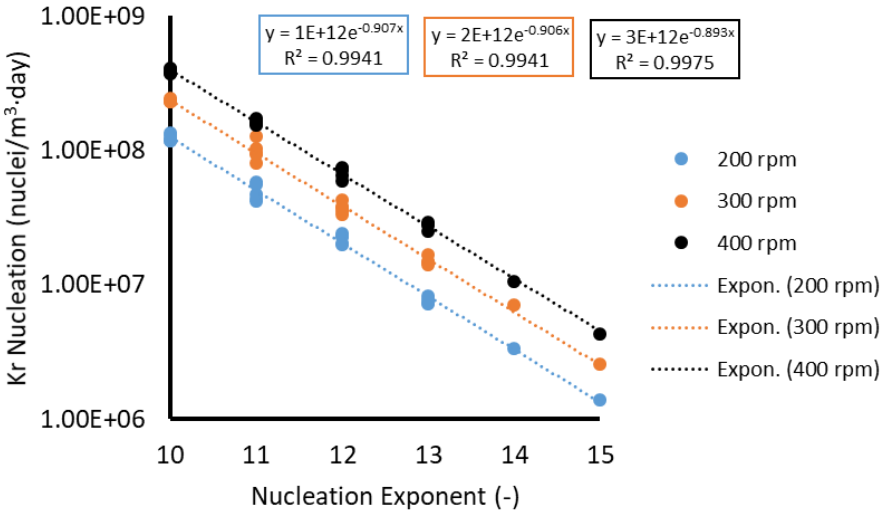

Figure 5.3: Best Kr Nucleation Values vs. Nucleation Exponent.

Observing Figure 5.3 is of special interest, since it likely explains why values of the parameters describing the nucleation mechanism differ in the literature of precipitation modelling of struvite (Burns *et al.*, 2021; Galbraith *et al.*, 2014; Hanhoun *et al.*, 2013; Triger *et al.*, 2012). On one hand, the effect of compensation is clear as the best Kr Nucleation is clearly influenced by the pre-selected value of the Nucleation Exponent. On the other hand, the best value of the Kr Nucleation increases with an increasing shear rate. Therefore, both, compensation and ignoring mixing effects could be the reasons for the shifting parameter values of the contributions found in the literature.

Regarding growth mechanism, Figure 5.4 (a, c, e) shows the value of the posterior density for each sampled Kr Growth value in the same 1000-simulation group, while Figure 5.4 (b, d, f) is a histogram where parameter range has been partitioned in 15 bins, as done in Figure 5.2.

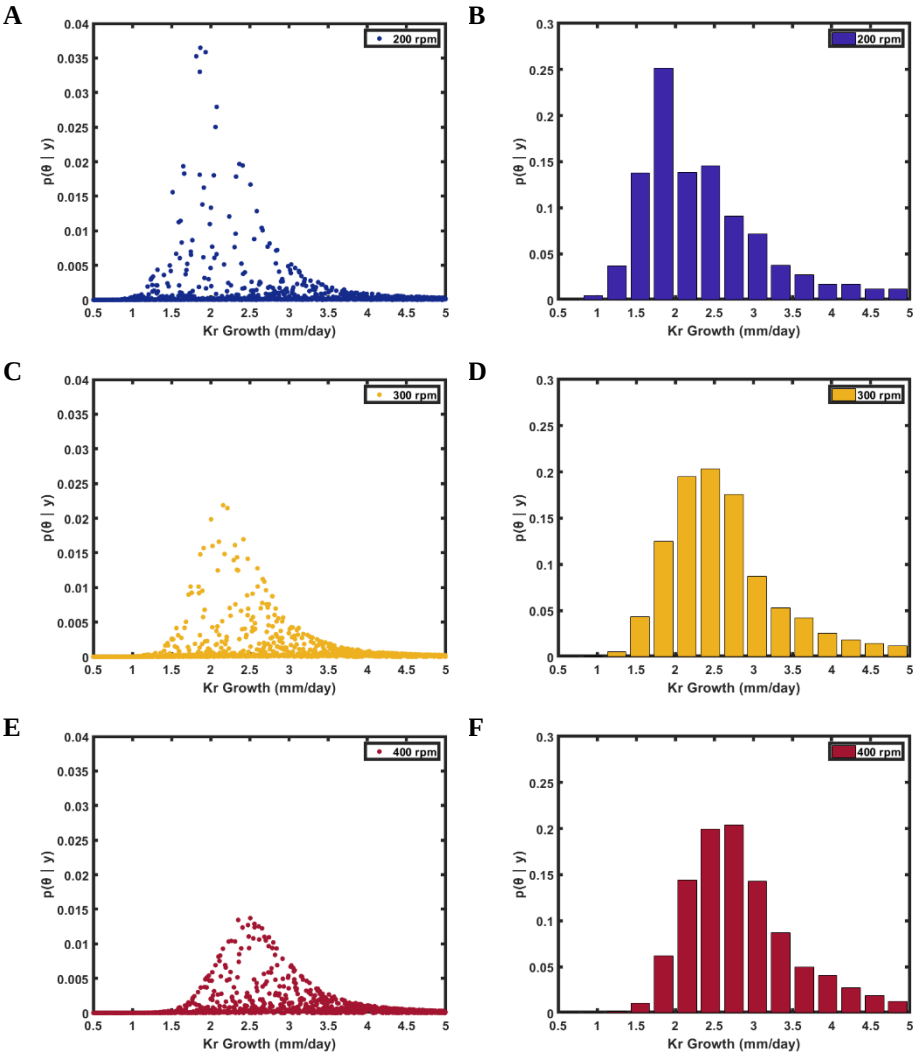

Figure 5.4: Posterior density distribution for the Kr Growth for each shear rate. Posterior density values for 200 rpm (a), Histogram of the posterior density for 200 rpm (b), Posterior density values for 300 rpm (c) Histogram of the posterior density for 300 rpm (d), Posterior density values for 400 rpm (e), Histogram of the posterior density for 200 rpm (b).

The trend is similar to the one observed for the Kr Nucleation. Again, distributions with distinctive peaks were obtained and the mode is significantly different for each shear rate, which means that the Kr Growth depends on the shear rate and its effect should also be decoupled.

Figure 5.5 shows best Kr Growth values for each shear rate in each 1000-simulation group against their corresponding value of the Growth Exponent. As it happened for the nucleation mechanism, the best values of the Kr Growth were bigger as the shear rate increased within the same 1000 simulation run.

Regarding parameter identifiability, lower Kr Growth values were obtained for an increasing Growth Exponent. In addition, Kr Growth best values were also lower for an increasing value of the Area Exponent, showing that in this case the correlation was more complex than for the nucleation mechanism, as it involved the interaction of three parameters. Therefore, even if the role of these three parameters in the equations describing growth mechanism was different (see section 5.3.1), as the Kr Growth value calibrated was not unique, it could be concluded that correlation existed among the parameters describing growth mechanism.

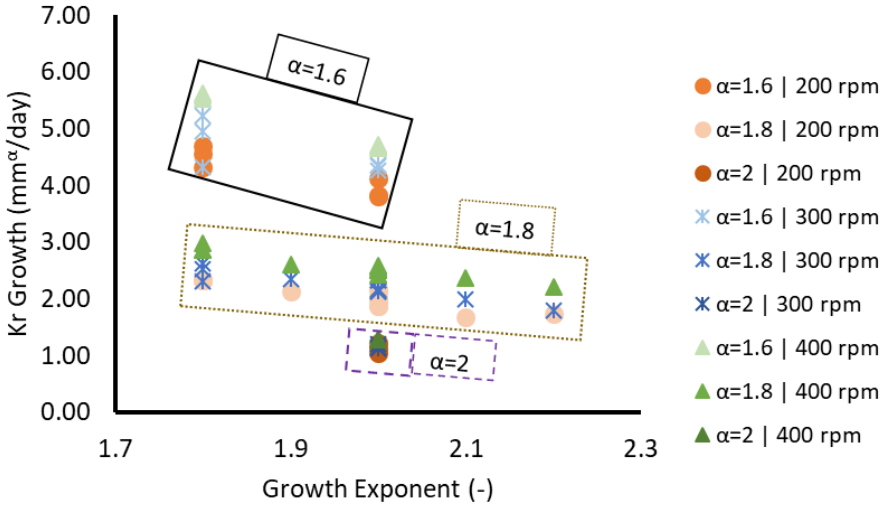

Figure 5.5: Best Kr Growth Values vs. Growth Exponent.

5.4.2. New proposed kinetic laws

Table 5.4 includes the mode of the Kr Nucleation and Kr Growth for each shear rate and the pre-selected exponent values. From the mode of the parameter values, a relationship between the kinetic constants and the shear rate is proposed (see Figure 5.6 and 5.7) for the re-definition of the kinetic rates.

Table 5.4: Mode of the kinetic constants for each stirring speed and shear rate.

Stirring speed (rpm)	Shear rate (s^{-1})	Kr Nucleation (nuclei/(m^3·day))	Kr Growth (mm^{α}/day)
200	150	7.17E+06	1.87
300	276	1.49E+07	2.16
400	425	2.80E+07	2.50

These relationships are power functions with the shape:

$$K_B = K'_B \cdot \gamma^{n_{BS}} \quad \textbf{5.11}$$

$$K_G = K'_G \cdot \gamma^{n_{GS}} \quad \textbf{5.12}$$

Where $K'_B \left(\frac{\text{nuclei}}{\text{m}^3\cdot\text{day}} \cdot s^{n_{BS}}\right)$ is the new kinetic constant independent of the average shear rate for homogeneous nucleation, n_{BS} (-) is the exponent of the shear rate dependence for homogeneous nucleation mechanism, $K'_G \left(\frac{\text{mm}^{\alpha}}{\text{day}} \cdot s^{n_{GS}}\right)$ is the new kinetic constant independent of the average shear rate for growth and n_{GS} (-) is the exponent of the shear rate dependence for growth mechanism.

Therefore, the proposed nucleation and growth rate expressions are written as follows.

$$\left.\frac{\partial X_1}{\partial t}\right|_N = K'_B \cdot \gamma^{n_{BS}} \cdot SI^{n_B} \cdot V \cdot mesf_1 \quad \textbf{5.13}$$

$$\left.\frac{\partial X_i}{\partial t}\right|_{G_{i\rightarrow i+1}} = K'_G \cdot \gamma^{n_{GS}} \cdot SI^{n_G} \cdot \frac{X_i}{\frac{(L_i + L_{i+1})}{2}^{\alpha}} \quad \textbf{5.14}$$

From the relationships included in the Figure 5.6 and 5.7, the values of the parameters were obtained and the effect of the shear rate decoupled from the K_B and K_G:

$$K_B = 10415 \cdot \gamma^{1.3004} \quad \textbf{5.15}$$

$$K_G = 0.4578 \cdot \gamma^{0.2791} \quad \textbf{5.16}$$

For the mixing conditions studied, the value of each calibrated Kr Nucleation and Kr Growth increased with the shear rate value (see Table 5.4). The proposed relationships accounted this effect. Power functions were chosen because they represented well the relationship between the shear rate and the Kr Nucleation and Kr Growth, quantified as a high value of R^2. In addition, power functions were considered a good option due to the stability they offer when included in mathematical models and because they allow quantitative comparisons of the effect of the shear rate on each mechanism. In this sense, the exponents of the power functions were approximately 1.3 for primary homogeneous nucleation mechanism and 0.3 for growth. Therefore, according to the analysis procedure followed, the effect of the shear rate in the nucleation mechanism was greater than in growth. This higher effect of the shear rate on the nucleation mechanism than in growth agrees well with previous literature findings (Tribout *et al*., 1996; Wolkowicz, 1978).

However, the proposed relationships should be considered only a starting point in the evaluation of the shear rate in the modelling of kinetics of the nucleation and growth mechanisms for struvite, as other mathematical functions could also relate the shear rate and the kinetic constants for the available data. In addition, due to the correlation between the parameters describing the same mechanism, parameter values from the proposed relationships should not be separately used to express nucleation or growth kinetics. Also, other effects accounted in the literature, such as the possible negative effect of attrition in the nucleation for high mixing intensities (Mullin and Raven, 1962), are not taken into account in the proposed power functions. Therefore, their use out of the limits of the operational values for which they have been calibrated is not recommended.

In order to have results that are more conclusive and to avoid possible compensation effects, it is wise to calibrate the model using data from different experimental configurations and with more case studies. However, changing the experimental

configuration would undoubtedly affect the shear rate average value and spatial distribution in the reactor, further complicating to obtain representative data.

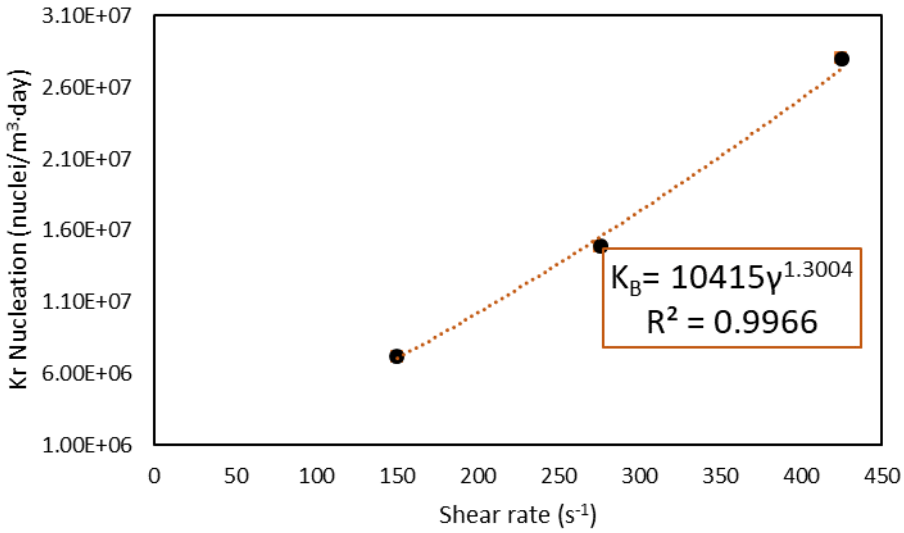

Figure 5.6: Relationship between the best points of the Kr Nucleation (see Table 5.4) and decoupling of the constant with the shear rate.

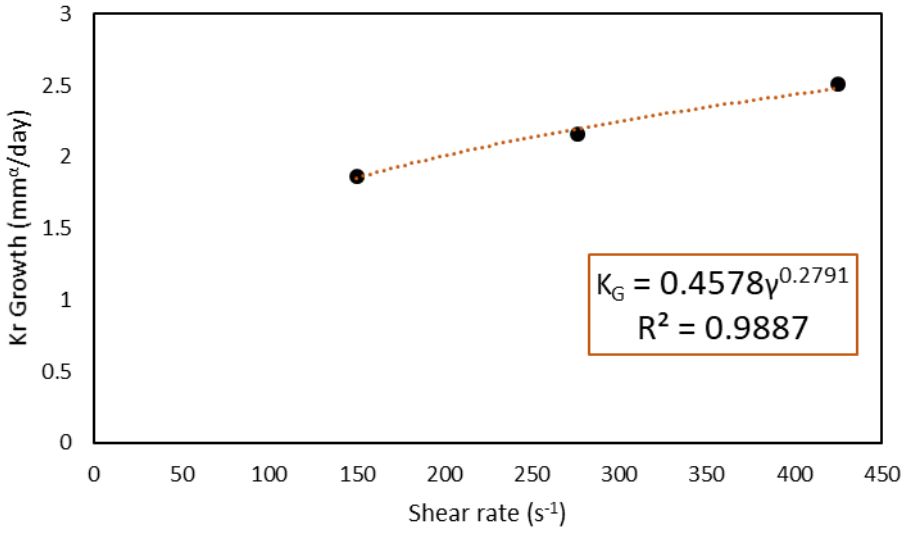

Figure 5.7: Relationship between the best points of the Kr Growth (see Table 5.4) and decoupling of the constant with the shear rate.

The main advance of substituting the original kinetic constants by these new relationships is the decoupling of the shear rate in each kinetic rate. This transformation helps to simulate the effect of experimentally changing the local mixing intensity, due to a varying stirrer speed.

This is a step forward in modelling precipitation process as this effect is very often ignored. Furthermore, the methodology followed could help to describe more in detail other unit processes based on mass transfer phenomena and improve existing IWA modelling libraries by decoupling the shear rate in their kinetic constants. In addition, explicitly including the shear rate effects in the kinetics could be useful for scaling-up of processes, if methodologies to create compartmental models are further developed. Compartmental models are a promising solution to simulate in a simplified way the SI and solid distribution in precipitation reactors (Liiri *et al*., 2010). Using CFD to create the compartmental models where the calibrated PBM would be implemented would help to have more realistic simulation results, as both the effect of macro and micro scale mixing would be included. For this issue, it is necessary to have a model where the information of the behaviour of the PSD under different mixing and SI regimes is included, as the one proposed in this chapter.

5.4.3. Comparison between the experimental and simulation results

Experimental results showed that for the same initial SI, a higher shear rate, as a consequence of a higher stirring speed, led to a faster pH decay and to smaller particle sizes. Here, these experimental results are compared with the outputs of simulations performed with the parameter values from Table 5.4. The agreement between the experimental data was good and justified the need of improving the original PBM with the Area Exponent and the shear rate dependency.

5.4.3.1. Low Saturation

The comparison between the experimental results and the simulations for the Low SI is included in Figure 5.8. These results show that the pH decay has been well addressed, especially in the 400 rpm experiment. The experimental samples of the PSD for the calibration were taken at minutes 20 and 60. As it can be observed in the pH evolution charts in Figure 5.8, at 20 minutes the experiments almost had reached the equilibrium, i.e. a constant pH value. Therefore, little change could be observed in the experimentally measured PSD. This effect was also addressed in the model,

where the simulated PSD were very similar at times 20 and 60 minutes in the three cases.

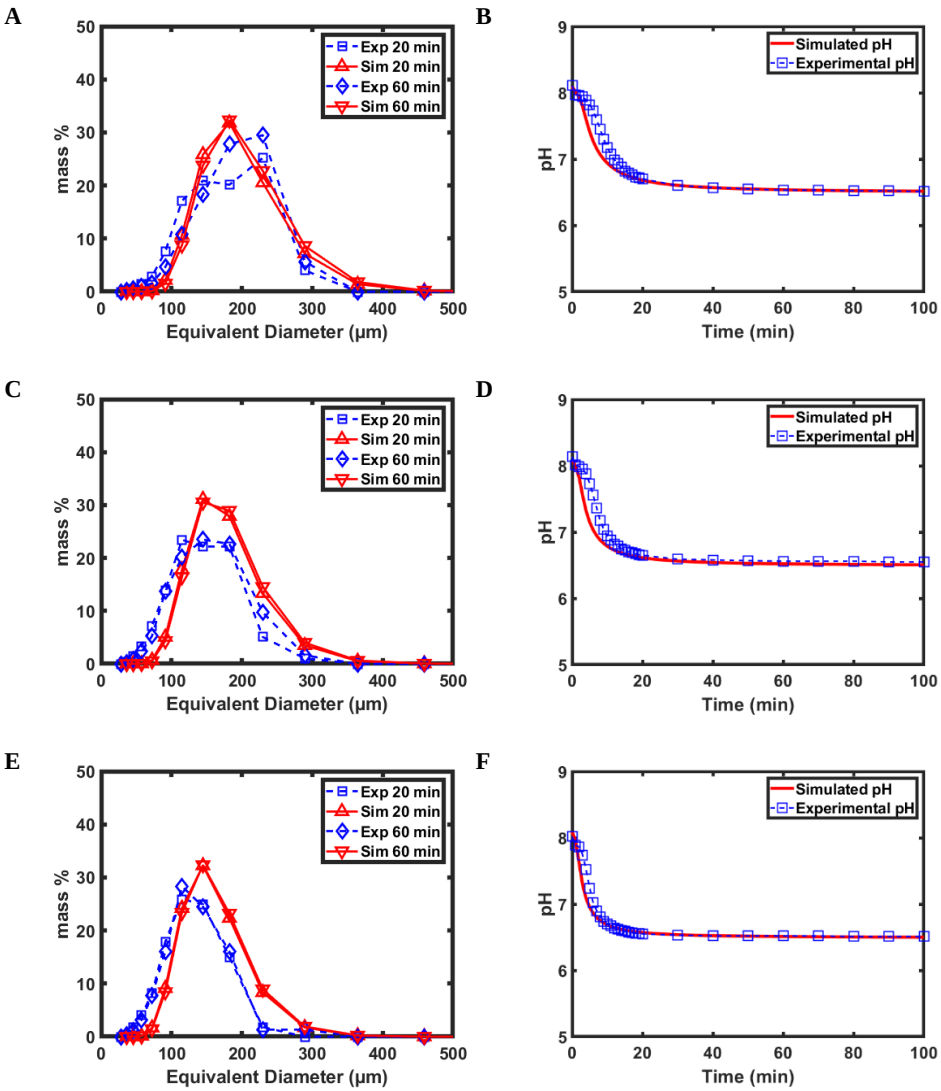

Figure 5.8: Comparison between experimental results and simulations for the PSD of Experiment LSI- Lγ (A), the pH evolution of Experiment LSI- Lγ (B), PSD of Experiment LSI- Mγ (C), the pH evolution of Experiment LSI- Mγ (D), PSD of Experiment LSI- Hγ (E) and the pH evolution of Experiment LSI- Hγ (F).

5.4.3.2. Medium Saturation

Figure 5.9 shows the comparison between the experimental results and the simulations for the Medium SI. Results of the pH decay show a very good agreement between the experimental and simulation results. The PSD were measured at 90 seconds and 50 minutes in order to have values at non-equilibrium and equilibrium conditions. Results from the simulations show how the PSD increased from the first sampling time to the second, as it happened in the experiment. However, the model underpredicts the final PSD, especially in the 400 rpm case.

5.4.3.3. High Saturation

Results from the experiments performed at High SI and the corresponding simulation results are included in Figure 5.10. These experiment showed a very sharp pH decay, associated with a fast precipitation. This fast precipitation is confirmed by the little change observed at the PSD measurements at times 45 seconds (non-equilibrium) and 20 minutes (equilibrium). The model was able to predict reasonably well the fast pH decay and the non-equilibrium and equilibrium PSD for all the shear rates.

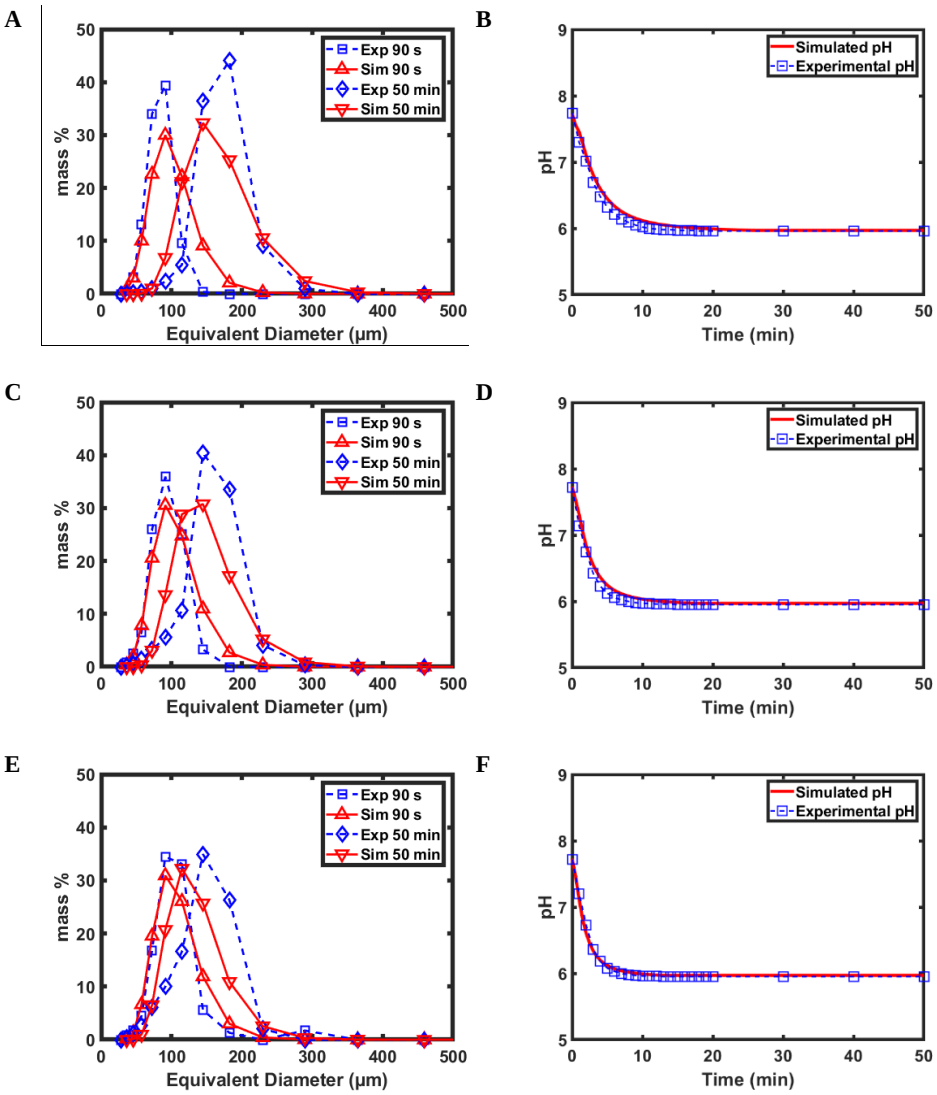

Figure 5.9: Comparison between experimental results and simulations for the PSD of Experiment MSI- Lγ (A), the pH evolution of Experiment MSI- Lγ (B), PSD of Experiment MSI- Mγ (C), the pH evolution of Experiment MSI- Mγ (D), PSD of Experiment MSI- Hγ (E) and the pH evolution of Experiment MSI- Hγ (F).

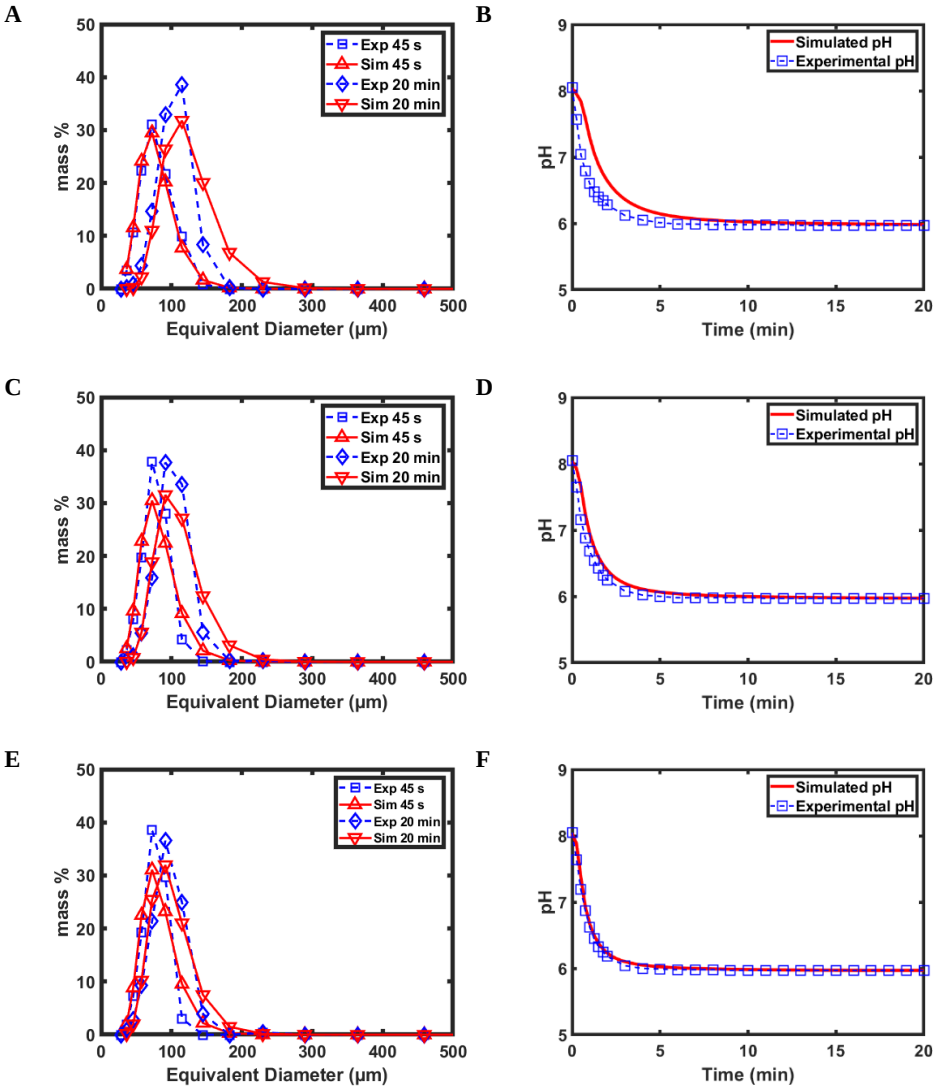

Figure 5.10: Comparison between experimental results and simulations for the PSD of Experiment HSI- Lγ (A), the pH evolution of Experiment HSI- Lγ (B), PSD of Experiment HSI- Mγ (C), the pH evolution of Experiment HSI- Mγ (D), PSD of Experiment HSI- Hγ (E) and the pH evolution of Experiment HSI- Hγ (F).

5.5 SUMMARY

The effect of mixing in the modelling of processes based on mass transfer phenomena is commonly ignored in wastewater treatment modelling. For the specific case of precipitation, the experimental evidence gathered in Chapter 4 and results from the literature showed that the shear rate affected the process. Including the shear rate in the kinetics of the mechanisms described in the model is a way to consider the effect of micromixing. However, micromixing effect is rarely included in the modelling of nucleation and growth of crystals. This should be changed if a more detailed description of the process is required, as it happens when design and optimization of the technologies is pursued. From the results obtained in this chapter it can be concluded that:

1) The comparative analysis performed between the experimental data and the simulation outputs showed that the effect of the shear rate is identifiable in nucleation and growth processes. Therefore, the decoupling of the shear rate from the kinetic constants is recommended.

2) From the considered data, the new expressions proposed for the nucleation and growth mechanisms of the mass-based discretized PBM applied to struvite precipitation are power law functions including the shear rate to an exponent. This transformation in the kinetics helped to reproduce in the simulations the effect that changing the stirrer speed had in the experimental results: a faster pH decay and a smaller PSD for an increasing stirring speed.

Explicitly including the shear rate as a process variable is a step forward in the modelling of WRRF unit processes and opens a way to improve existing IWA modelling libraries, develop methodologies to create compartmental models and improve scaling-up of such processes.

CHAPTER 6

CONCLUSIONS AND FUTURE RESEARCH LINES

6.1 CONCLUSIONS

The main outcome of the thesis is a mathematical model capable to describe in detail mechanisms occurring in a precipitation process of struvite for its recovery. This model is a mass-based PBM where hydrodynamic effects have been considered. The model, which has been calibrated for different SI and mixing intensities, showed a good agreement between the experimental data and simulated results. In addition, the research done in the thesis has allowed to reach the next main conclusions:

- A mass-based PBM including main struvite precipitation mechanisms (nucleation, growth and aggregation) was designed, constructed and successfully implemented in WEST-DHI simulation platform.
    - The mass-based model was designed according to Ceit's PWM methodology, guaranteeing mass and charge balance. This is an improvement to the previously existing contributions as the integration of the PBM in a simulation of a WRRF with other unit processes will now be systematic and straightforward.
    - An evaluation of the theoretical parameter identifiability was done. Results from this analysis showed that all the parameters describing the considered mechanisms had some weight in the outputs and that there are large zones of the parameter values where the theoretical identifiability was possible. Therefore, the structure of the model was considered valid.

- The effect that the initial SI (related with the concentration of the species participating in struvite precipitation and the initial pH) and the mixing intensity (related to the shear rate) have in struvite precipitation was experimentally analysed in two different experimental set-ups.
    - Higher shear rates favoured primary homogeneous nucleation, measured through reduced induction times and greater particle number densities. This phenomena led to more rapid precipitation and reduced population mean particle size. Higher SI favoured nucleation and growth mechanism and was related to a faster precipitation process and a greater particle density.
    - As the SI and the local mixing intensity played a role in struvite nucleation and growth mechanisms, their effect should be included in the kinetics of the process when the PSD is of importance. The data collected in the experimental campaigns was considered relevant and valid for calibration purposes.
- The effect of local mixing intensity, quantified as the shear rate was included in the kinetics defining the mechanisms of the mass-based PBM.
    - A methodology based on Bayesian Monte Carlo techniques was used to assess the effect of the shear rate in the primary homogeneous nucleation and growth mechanisms, based on experimental data and simulation outputs. According to the obtained results, the effect of the shear rate in both mechanisms was identifiable.
    - As a consequence of the identified effect of the shear rate, new kinetic laws for the PBM where the shear rate effect is explicitly included were proposed. Including the shear rate in the kinetics of the model is a way to consider the effect of mixing at local scale. This transformation in the kinetics helped to reproduce in the simulations the effect that changing the stirrer speed had in the experimental results: a faster pH decay and a smaller PSD for an increasing stirring speed.

6.2 FUTURE RESEARCH LINES

The calibrated model is capable to successfully reproduce the precipitation in a stirred tank under different average shear rate and the SI conditions. However, for its generalized use, the effect of the mixing at the macro scale should also be considered. Especially because struvite precipitation is often performed in fluidised bed reactors, which distinguish operating zones depending on a decreasing upflow velocity. The decreasing upflow velocity classifies particles by its size.

For a general application of the calibrated PBM for design and optimization purposes, it would be interesting to follow the research done in this thesis by:

- Developing a methodology where the CFD and PBM model outputs are combined. CFD could be used to simulate the hydrodynamics in the reactor and under the assumption that the precipitation does not interfere in the hydrodynamics, obtain compartments based on different chemical, shear rate and solid distribution conditions. Therefore, CFD could be used as a way to 'measure' the shear rate in any reactor type and as a data source for the compartmental modelling. The mass-based PBM could be afterwards implemented in each of the compartments, for a much more detailed simulation of the precipitation process.
- Perform more experiments to explore different experimental conditions in order to increase the trustworthiness of the parameter values and the proposed kinetic relationships with the shear rates.

CHAPTER 7

REFERENCES

Abrahamsson, P.J., Kvist, P., Reynolds, G., Yu, X., Niklasson Björn, I., Hounslow, M.J., Rasmuson, A., 2018. Analysis of mesoscale effects in high-shear granulation through a computational fluid dynamics–population balance coupled compartment model. Particuology 36, 1–12. https://doi.org/10.1016/j.partic.2017.01.008

Agrawal, S., Guest, J.S., Cusick, R.D., 2018. Elucidating the impacts of initial supersaturation and seed crystal loading on struvite precipitation kinetics, fines production, and crystal growth. Water Res. 132, 252–259. https://doi.org/10.1016/j.watres.2018.01.002

Agrawal, S.G., Paterson, A. (Tony), Jones, J.R., Mcleod, J.S., Bronlund, J., Bajpai, H., 2017. Secondary nucleation studies on alpha lactose monohydrate under stirred conditions. Int. Dairy J. 66, 61–67. https://doi.org/10.1016/j.idairyj.2016.11.004

Amann, A., Zoboli, O., Krampe, J., Rechberger, H., Zessner, M., Egle, L., 2018. Environmental impacts of phosphorus recovery from municipal wastewater. Resour. Conserv. Recycl. 130, 127–139. https://doi.org/10.1016/j.resconrec.2017.11.002

Ariyanto, E., Sen, T.K., Ang, H.M., 2014. The influence of various physico-chemical process parameters on kinetics and growth mechanism of struvite crystallisation. Adv. Powder Technol. 25, 682–694. https://doi.org/10.1016/j.apt.2013.10.014

Asiri, S., 2012. Design and Implementation of Differential Agitators to Maximize Agitating Performance. Int. J. Mech. Appl. 2, 98–112. https://doi.org/10.5923/j.mechanics.20120206.01

Ayranci, I., Kresta, S.M., 2011. Design rules for suspending concentrated mixtures of solids in stirred tanks. Chem. Eng. Res. Des. 89, 1961–1971. https://doi.org/10.1016/j.cherd.2011.01.008

Baldyga, J., Bourne, J.R., 1992. Interactions between mixing on various scales in stirred tank reactors. Chem. Eng. Sci. 47, 1839–1848. https://doi.org/10.1016/0009-2509(92)80302-S

Baldyga, J., Podgórska, W., Pohorecki, R., 1995. Mixing-precipitation model with application to double feed semibatch precipitation. Chem. Eng. Sci. 50, 1281–1300. https://doi.org/10.1016/0009-2509(95)98841-2

Barat, R., Serralta, J., Ruano, M. V., Jiménez, E., Ribes, J., Seco, A., Ferrer, J., 2013. Biological nutrient removal model no. 2 (BNRM2): A general model for wastewater treatment plants. Water Sci. Technol. 67, 1481–1489. https://doi.org/10.2166/wst.2013.004

Barnes, N.J., Bowers, A.R., 2017. A probabilistic approach to modeling struvite precipitation with uncertain equilibrium parameters. Chem. Eng. Sci. 161, 178–186. https://doi.org/10.1016/j.ces.2016.12.026

Batstone, D.J., Keller, J., Angelidaki, I., Kalyuzhny, S.V., Pavlostathis, S.G., Rozzi, A., Sanders, W.T.M., Siegrist, H., Vavilin, V.A., 2002. Anaerobic digestion model No. 1 (ADM1). London.

Bhuiyan, M.I.H., Mavinic, D.S., Beckie, R.D., 2008a. Nucleation and growth kinetics of struvite in a fluidized bed reactor. J. Cryst. Growth 310, 1187–1194. https://doi.org/10.1016/j.jcrysgro.2007.12.054

Bhuiyan, M.I.H., Mavinic, D.S., Koch, F.A., 2008b. Phosphorus recovery from wastewater through struvite formation in fluidized bed reactors: a sustainable approach. Water Sci. Technol. 57, 175–81. https://doi.org/10.2166/wst.2008.002

Blasone, R.-S., Vrugt, J.A., Madsen, H., Rosbjerg, D., Robinson, B.A., Zyvoloski, G.A., 2008. Generalized likelihood uncertainty estimation (GLUE) using adaptive Markov Chain Monte Carlo sampling. Adv. Water Resour. 31, 630–648. https://doi.org/10.1016/j.advwatres.2007.12.003

Borgerding, J., 1972. Phosphate Deposits in Digestion Systems. J. Water Pollut. Control Fed. 44, 813–819.

Bramley, A.S., Hounslow, M.J., Ryall, R.L., 1996. Aggregation during Precipitation from Solution: A Method for Extracting Rates from Experimental Data. Popul. (English Ed. 165, 155–165.

Brun, R., Kühni, M., Siegrist, H., Gujer, W., Reichert, P., 2002. Practical identifiability of ASM2d parameters - Systematic selection and tuning of parameter subsets. Water Res. 36, 4113–4127. https://doi.org/10.1016/S0043-1354(02)00104-5

Brun, R., Reichert, P., Ku, H.R., 2001. Practical identi ability analysis of large environmental simulation models. Water Resour. Res. 37, 1015–1030. https://doi.org/10.1029/2000WR900350

Buck, W. De, 2012. Struvite crystallization and separation in digested sludge. Delft

University of Technology | Waternet.

Burns, M., Natividad Marin, L., Schneider, P.A., 2016. Investigations of a continuous Poiseuille flow struvite seed crystallizer - Mixer performance and aggregate disruption by sonication. Chem. Eng. J. 295, 552–562. https://doi.org/10.1016/j.cej.2016.03.061

Burns, M., Sheehan, M., Schneider, P.A., 2021. Nucleation and crystal growth kinetic parameter optimization of a continuous Poiseuille flow struvite crystallizer using a discretized population balance and dynamic fluid model. Chem. Eng. J. 405, 126607. https://doi.org/10.1016/j.cej.2020.126607

Chen, P.C., Kou, K.L., Tai, H.K., Jin, S.L., Lye, C.L., Lin, C.Y., 2002. Removal of carbon dioxide by reactive crystallization in a scrubber - Kinetics of barium carbonate crystals. J. Cryst. Growth 237–239, 2166–2171. https://doi.org/10.1016/S0022-0248(01)02260-6

Cieślik, B., Konieczka, P., 2017. A review of phosphorus recovery methods at various steps of wastewater treatment and sewage sludge management. The concept of "no solid waste generation" and analytical methods. J. Clean. Prod. 142, 1728–1740. https://doi.org/10.1016/j.jclepro.2016.11.116

Climent, J., Martínez-Cuenca, R., Carratalà, P., González-Ortega, M.J., Abellán, M., Monrós, G., Chiva, S., 2019. A comprehensive hydrodynamic analysis of a full-scale oxidation ditch using Population Balance Modelling in CFD simulation. Chem. Eng. J. 374, 760–775. https://doi.org/10.1016/j.cej.2019.05.195

Cordell, D., White, S., 2011. Peak phosphorus: Clarifying the key issues of a vigorous debate about long-term phosphorus security. Sustainability 3, 2027–2049. https://doi.org/10.3390/su3102027

Costa, C.B.B., Maciel, M.R.W., Filho, R.M., 2007. Considerations on the crystallization modeling: Population balance solution. Comput. Chem. Eng. 31, 206–218. https://doi.org/10.1016/j.compchemeng.2006.06.005

Crutchik, D., Garrido, J.M., 2016. Kinetics of the reversible reaction of struvite crystallisation. Chemosphere 154, 567–572. https://doi.org/10.1016/j.chemosphere.2016.03.134

de Gracia, M., Grau, P., Huete, E., Gómez, J., García-Heras, J.L., Ayesa, E., 2009. New generic mathematical model for WWTP sludge digesters operating under aerobic and anaerobic conditions: Model building and experimental verification. Water Res. 43, 4626–4642. https://doi.org/10.1016/j.watres.2009.07.014

De Santis, F., Pantani, R., Titomanlio, G., 2016. Effect of shear flow on spherulitic growth and nucleation rates of polypropylene. Polym. (United Kingdom) 90, 102–110. https://doi.org/10.1016/j.polymer.2016.02.059

Desmidt, E., Ghyselbrecht, K., Zhang, Y., Pinoy, L., Van Der Bruggen, B., Verstraete, W., Rabaey, K., Meesschaert, B., 2015. Global phosphorus scarcity and full-scale

P-recovery techniques: A review. Crit. Rev. Environ. Sci. Technol. 45, 336–384. https://doi.org/10.1080/10643389.2013.866531

Doyle, J.D., Parsons, S.A., 2002. Struvite formation, control and recovery. Water Res. 36, 3925–3940.

Egle, L., Rechberger, H., Krampe, J., Zessner, M., 2016. Phosphorus recovery from municipal wastewater: An integrated comparative technological, environmental and economic assessment of P recovery technologies. Sci. Total Environ. 571, 522–542. https://doi.org/10.1016/j.scitotenv.2016.07.019

Ekama, G.A., Sötemann, S.W., Wentzel, M.C., 2006. Mass balance-based plant-wide wastewater treatment plant models - Part 3: Biodegradability of activated sludge organics under anaerobic conditions. Water SA 32, 287–296. https://doi.org/10.4314/wsa.v32i3.5273

European Commision, 2015. An EU action plan for the circular economy. Com 614, 21. https://doi.org/10.1017/CBO9781107415324.004

European Commission, 2018. Commission Staff Working Document. Report on Critical Raw Materials and the Circular Economy 1–16.

European Sustainable Phosphorus Platform, 2020. ESPP – DPP – NNP phosphorus recovery technology catalogue Sewage P-recovery : full scale plants operating or under permitting / construction Fertiliser industry – Ash2Phos.

Ewert, W., Hermanussen, O., Kabbe, C., Mêlè, C., Niewersch, C., Paillard, H., Stössel, E., Wagenbach, A., 2014. Sustainable sewage sludge management fostering phosphorus recovery and energy efficiency.

Fang, C., Zhang, T., Jiang, R., Ohtake, H., 2016. Phosphate enhance recovery from wastewater by mechanism analysis and optimization of struvite settleability in fluidized bed reactor. Sci. Rep. 6, 1–10. https://doi.org/10.1038/srep32215

Fernández-Arévalo, T., Lizarralde, I., Fdz-Polanco, F., Pérez-Elvira, S.I., Garrido, J.M., Puig, S., Poch, M., Grau, P., Ayesa, E., 2017a. Quantitative assessment of energy and resource recovery in wastewater treatment plants based on plant-wide simulations. Water Res. 118, 272–288. https://doi.org/10.1016/j.watres.2017.04.001

Fernández-Arévalo, T., Lizarralde, I., Grau, P., Ayesa, E., 2014. New systematic methodology for incorporating dynamic heat transfer modelling in multi-phase biochemical reactors. Water Res. 60, 141–155. https://doi.org/10.1016/j.watres.2014.04.034

Fernández-Arévalo, T., Lizarralde, I., Maiza, M., Beltrán, S., Grau, P., Ayesa, E., 2017b. Diagnosis and optimization of WWTPs using the PWM library: Full-scale experiences. Water Sci. Technol. 75, 518–529. https://doi.org/10.2166/wst.2016.482

Forsyth, C., Burns, I.S., Mulheran, P.A., Sefcik, J., 2016. Scaling of Glycine Nucleation Kinetics with Shear Rate and Glass-Liquid Interfacial Area. Cryst. Growth Des. 16, 136–144. https://doi.org/10.1021/acs.cgd.5b01042

Gábor, A., Villaverde, A.F., Banga, J.R., 2017. Parameter identifiability analysis and visualization in large-scale kinetic models of biosystems. BMC Syst. Biol. 11, 1–16. https://doi.org/10.1186/s12918-017-0428-y

Galbraith, S.C., Schneider, P. a, Flood, a E., 2014. Model-driven experimental evaluation of struvite nucleation, growth and aggregation kinetics. Water Res. 56, 122–32. https://doi.org/10.1016/j.watres.2014.03.002

Galbraith, S.C.S.C., 2011. A study of struvite nucleation, crystal growth and aggregation.

Gomez, J., de Gracia, M., Ayesa, E., Garcia-Heras, J.L., 2007. Mathematical modelling of autothermal thermophilic aerobic digesters. Water Res. 41, 959–968. https://doi.org/10.1016/j.watres.2006.11.042

Grau, P., de Gracia, M., Vanrolleghem, P.A., Ayesa, E., 2007. A new plant-wide modelling methodology for WWTPs. Water Res. 41, 4357–4372. https://doi.org/10.1016/j.watres.2007.06.019

Guest, J.S., Skerlos, S.J., Barnard, J.L., Beck, M.B., Daigger, G.T., Hilger, H., Jackson, S.J., Karvazy, K., Kelly, L., Macpherson, L., Mihelcic, J.R., Pramanik, A., Raskin, L., Van Loosdrecht, M.C.M., Yeh, D., Love, N.G., 2009. A new planning and design paradigm to achieve sustainable resource recovery from wastewater. Environ. Sci. Technol. 43, 6126–6130. https://doi.org/10.1021/es9010515

Günther, S., Grunert, M., Müller, S., 2018. Overview of recent advances in phosphorus recovery for fertilizer production. Eng. Life Sci. 18, 434–439. https://doi.org/10.1002/elsc.201700171

Hanhoun, M., Montastruc, L., Azzaro-Pantel, C., Biscans, B., Frèche, M., Pibouleau, L., 2013. Simultaneous determination of nucleation and crystal growth kinetics of struvite using a thermodynamic modeling approach. Chem. Eng. J. 215–216, 903–912. https://doi.org/10.1016/j.cej.2012.10.038

Hanhoun, M., Montastruc, L., Azzaro-Pantel, C., Biscans, B., Frèche, M., Pibouleau, L., 2011. Temperature impact assessment on struvite solubility product: A thermodynamic modeling approach. Chem. Eng. J. 167, 50–58. https://doi.org/10.1016/j.cej.2010.12.001

Henze, M., Gujer, W., Mino, T., van Loosdrecht, M.C.M., 2000. Activated sludge models ASM1, ASM2, ASM2d and ASM3. IWA Publishing, 2000.

Hill, P.J., Ng, K.M., 2002. Particle size distribution by design. Chem. Eng. Sci. 57, 2125 – 2138.

Hounslow, M.J., Ryall, R.L., Marshall, V.R., 1988. A discretized population balance for nucleation, growth, and aggregation. AIChE J. 34, 1821–1832.

https://doi.org/10.1002/aic.690341108

Hounslow, M.J., Wynn, E.J.W., Kubo, M., Pitt, K., 2013. Aggregation of growing crystals in suspension: I. Mumtaz revisited. Chem. Eng. Sci. 101, 731–743. https://doi.org/10.1016/j.ces.2013.06.058

Hulburt, H.M., Katz, S., 1964. Some problems in particle technology. Chem. Eng. Sci. 19, 555–574. https://doi.org/10.1016/0009-2509(64)85047-8

Huygens, D., Saveyn, H., 2018. DRAFT STRUBIAS Interim Report, DRAFT STRUBIAS Interim Report.

Ikumi, D.S., Harding, T.H., Brouckaert, C.J., Ekama, G.A., 2014a. Plant wide integrated biological, chemical and physical processes modelling of wastewater treatment plants in three phases (aqueous-gas-solid). Western Cape, South Africa.

Ikumi, D.S., Harding, T.H., Ekama, G.A., 2014b. Biodegradability of wastewater and activated sludge organics in anaerobic digestion. Water Res. 56, 267–279. https://doi.org/10.1016/j.watres.2014.02.008

Ilievski, D., Rudman, M., Metcalfe, G., 2001. The separate roles of shear rate and mixing on gibbsite precipitation. Chem. Eng. Sci. 56, 2521–2530. https://doi.org/10.1016/S0009-2509(00)00434-6

Jones, A.G., 2002. Crystallization Process Systems, First edit. ed. Butterworth-Heinemann, Oxford.

Jones, R.M., Tákacs, I., 2004. Importance of anaerobic digestion modelling on predicting the overall performance of waste-water tratment plants, in: Proceedings of the Tenth World Congress. Montréal (Canada).

Kazadi Mbamba, C., Batstone, D.J., Flores-Alsina, X., Tait, S., 2015a. A generalised chemical precipitation modelling approach in wastewater treatment applied to calcite. Water Res. 68, 342–353. https://doi.org/10.1016/j.watres.2014.10.011

Kazadi Mbamba, C., Tait, S., Flores-Alsina, X., Batstone, D.J., 2015b. A systematic study of multiple minerals precipitation modelling in wastewater treatment. Water Res. 85, 359–370. https://doi.org/10.1016/j.watres.2015.08.041

Koutsoukos, P., Amjad, Z., Tomson, B., Nancollas, G.H., 1980. Crystallization of Calcium Phosphates. A Constant Composition Study. J. Am. Chem. Soc. 102, 1553–1557. https://doi.org/10.1021/ja00525a015

Le Corre, K.S., Valsami-Jones, E., Hobbs, P., Parsons, S. a., 2009. Phosphorus Recovery from Wastewater by Struvite Crystallization: A Review, Critical Reviews in Environmental Science and Technology. https://doi.org/10.1080/10643380701640573

Li, B., Boiarkina, I., Yu, W., Huang, H.M., Munir, T., Wang, G.Q., Young, B.R., 2019. Phosphorous recovery through struvite crystallization: Challenges for future design. Sci. Total Environ. 648, 1244–1256.

https://doi.org/10.1016/j.scitotenv.2018.07.166

Li, T.S., Livk, I., Ilievski, D., 2003. Supersaturation and temperature dependency of gibbsite growth in laminar and turbulent flows. J. Cryst. Growth 258, 409–419. https://doi.org/10.1016/S0022-0248(03)01557-4

Liew, T.L., Barrick, J.P., Hounslow, M.J., 2003. A micro-mechanical model for the rate of aggregation during precipitation from solution. Chem. Eng. Technol. 26, 282–285. https://doi.org/10.1002/ceat.200390042

Liiri, M., Hatakka, H., Kallas, J., Aittamaa, J., Alopaeus, V., 2010. Modelling of crystal growth of KDP in a 100dm3 suspension crystallizer using combination of CFD and multiblock model. Chem. Eng. Res. Des. 88, 1297–1303. https://doi.org/10.1016/j.cherd.2009.12.004

Liu, J., Rasmuson, A.C., 2013. Influence of Agitation and Fluid Shear on Primary Nucleation in Solution. Cryst. Growth Des. 61, 1617–1626.

Liu, J., Svärd, M., Rasmuson, A.C., 2014. Influence of agitation and fluid shear on nucleation of m-hydroxybenzoic acid polymorphs. Cryst. Growth Des. 14, 5521–5531. https://doi.org/10.1021/cg500698v

Liu, J., Svärd, M., Rasmuson, Å.C., 2015. Influence of Agitation on Primary Nucleation in Stirred Tank Crystallizers. Cryst. Growth Des. 15, 4177–4184. https://doi.org/10.1021/cg501791q

Lizarralde, I., 2015. A new systematyc methodology for incorporating chemical and physico-chemical transformations into multiphase wastewater treatment process models. Universidad de Navarra.

Lizarralde, I., Fernández-Arévalo, T., Brouckaert, C., Vanrolleghem, P., Ikumi, D.S., Ekama, G. a., Ayesa, E., Grau, P., 2015. A new general methodology for incorporating physico-chemical transformations into multi-phase wastewater treatment process models. Water Res. 74, 239–256. https://doi.org/10.1016/j.watres.2015.01.031

Lizarralde, I., Fernández-Arévalo, T., Manas, A., Ayesa, E., Grau, P., 2019. Model-based opti mization of phosphorus management strategies in Sur WWTP, Madrid. Water Res. 153, 39–52. https://doi.org/10.1016/j.watres.2018.12.056

Manterola, G., Grau, P., Ayesa, E., Uriarte, J., Sancho, L., 2007. Mathematical modelling of sludge ozonation process for WWTP excess sludge reduction, in: IWA Specialist Conference Moving Forward, Wastewater Biosolids Sus-Tainability: Technical, Managerial, and Public Synergy. Moncton, New Brunswick, Canada, pp. 287–294.

Mao, Z., Yang, C., 2017. Micro-mixing in chemical reactors: A perspective. Chinese J. Chem. Eng. 25, 381–390. https://doi.org/10.1016/j.cjche.2016.09.012

Marcant, B., David, R., 1991. Experimental evidence for and prediction of micromixing effects in precipitation. AIChE J. 37, 1698–1710.

https://doi.org/10.1002/aic.690371113

Martin, C., Ayesa, E., 2010. An Integrated Monte Carlo Methodology for the calibration of water quality models. Ecol. Modell. 221, 2656–2667. https://doi.org/10.1016/j.ecolmodel.2010.08.008

Mehta, C.M., Batstone, D.J., 2013. Nucleation and growth kinetics of struvite crystallization. Water Res. 47, 2890–900. https://doi.org/10.1016/j.watres.2013.03.007

Mersmann, A., 2001. The Crystallization Technology Handbook, Second Edition Revised and Explained, 2nd ed. Marcel Dekker Inc., New York · Basel.

Mudragada, R., Kundral, S., Coro, E., Moncholi, M.E., Laha, S., Tansel, B., 2014. Phosphorous removal during sludge dewatering to prevent struvite formation in sludge digesters by full scale evaluation. J. Water Process Eng. 2, 37–42. https://doi.org/10.1016/j.jwpe.2014.04.006

Mullin, J.W., 2001. Crystallization, 4th editio. ed. Butterworth-Heinemann, Oxford. https://doi.org/https://doi.org/10.1016/B978-0-7506-4833-2.X5000-1

Mullin, J.W., Raven, K.D., 1962. Influence of Mechanical Agitation on the Nucleation of some Aqueous Salt Solutions. Nature 195, 35–38.

Musvoto, E. V., Wentzel, M.. C.M., Ekama, G.A.M., 2000a. Integrated chemical-physical processes modelling II Simulating aeration treatment of anaerobic digester supernatants 34, 1868–1880.

Musvoto, E. V., Wentzel, M.C., Loewenthal, R.E., Ekama, G.A., 2000b. Integrated chemical-physical processes modelling - I. Development of a kinetic-based model for mixed weak acid/base systems. Water Res. 34, 1857–1867. https://doi.org/10.1016/S0043-1354(99)00334-6

Myerson, A.S., 2001. Handbook of Industrial Crystallization, 2nd ed. Elsevier Science and Technology Books.

Nagata, S., 1975. Mixing: principles and applications. Tokyo.

Nagy, Z.K., Aamir, E., 2012. Systematic design of supersaturation controlled crystallization processes for shaping the crystal size distribution using an analytical estimator. Chem. Eng. Sci. 84, 656–670. https://doi.org/10.1016/j.ces.2012.08.048

Nagy, Z.K., Fevotte, G., Kramer, H., Simon, L.L., 2013. Recent advances in the monitoring, modelling and control of crystallization systems. Chem. Eng. Res. Des. 91, 1903–1922. https://doi.org/10.1016/j.cherd.2013.07.018

Nappo, V., Sullivan, R., Davey, R., Kuhn, S., Gavriilidis, A., Mazzei, L., 2018. Effect of shear rate on primary nucleation of para-amino benzoic acid in solution under different fluid dynamic conditions. Chem. Eng. Res. Des. 136, 48–56. https://doi.org/10.1016/j.cherd.2018.04.039

Nopens, I., Beheydt, D., Vanrolleghem, P.A., 2005. Comparison and pitfalls of different discretised solution methods for population balance models: A simulation study. Comput. Chem. Eng. 29, 367–377. https://doi.org/10.1016/j.compchemeng.2004.10.007

Nopens, I., Koegst, T., Mahieu, K., Vanrolleghem, P.A., 2004. PBM and activated sludge flocculation: From experimental data to a calibrated Model. IFAC Proc. Vol. 37, 231–236. https://doi.org/10.1016/s1474-6670(17)32588-0

Nopens, I., Torfs, E., Ducoste, J., Vanrolleghem, P. a., Gernaey, K. V., 2015. Population balance models: A useful complementary modelling framework for future WWTP modelling. Water Sci. Technol. 71, 159–167. https://doi.org/10.2166/wst.2014.500

Ohlinger, K.N., Young, T.M., Schroeder, E.D., 1999. Kinetics Effects on Preferential Struvite Accumulation in Wastewater. J. Environ. Eng. 125, 730–737.

Pastor, L., 2008. Estudio de la precipitación y recuperación del fósforo presente en las aguas residuales en forma de estruvita (MgNH4PO4·6H2O). Universidad Politécnica de Valencia.

Peng, L., Dai, H., Wu, Y., Peng, Y., Lu, X., 2018. A Comprehensive Review of the Available Media and Approaches for Phosphorus Recovery from Wastewater. Water. Air. Soil Pollut. 229. https://doi.org/10.1007/s11270-018-3706-4

Phillips, R., Rohani, S., Baldyga, J., 1999. Micromixing in a single-feed semi-batch precipitation process. AIChE J. 45, 82–92. https://doi.org/10.1002/aic.690450108

Pohorecki, R., Bałdyga, J., 1983. The use of a new model of micromixing for determination of crystal size in precipitation. Chem. Eng. Sci. 38, 79–83. https://doi.org/10.1016/0009-2509(83)80136-5

Prywer, J., Torzewska, A., Plociński, T., 2012. Unique surface and internal structure of struvite crystals formed by Proteus mirabilis. Urol. Res. 40, 699–707. https://doi.org/10.1007/s00240-012-0501-3

Rahaman, M.. S., Mavinic, D.S., Bhuiyan, M.I.. H., Koch, F.A., 2006. Exploring the determination of struvite solubility product from analytical results. Environ. Technol. 27, 951–961. https://doi.org/10.1080/09593332708618707

Robles, Á., Aguado, D., Barat, R., Borrás, L., Bouzas, A., Giménez, J.B., Martí, N., Ribes, J., Ruano, M.V., Serralta, J., Ferrer, J., Seco, A., 2020. New frontiers from removal to recycling of nitrogen and phosphorus from wastewater in the Circular Economy. Bioresour. Technol. 300, 122673. https://doi.org/10.1016/j.biortech.2019.122673

Romero-Güiza, M.S., Astals, S., Chimenos, J.M., Martínez, M., Mata-Alvarez, J., 2014. Improving anaerobic digestion of pig manure by adding in the same reactor a stabilizing agent formulated with low-grade magnesium oxide. Biomass and Bioenergy 67, 243–251. https://doi.org/10.1016/j.biombioe.2014.04.034

Romero-Güiza, M.S., Astals, S., Mata-Alvarez, J., Chimenos, J.M., 2015a. Feasibility of coupling anaerobic digestion and struvite precipitation in the same reactor: Evaluation of different magnesium sources. Chem. Eng. J. 270, 542–548. https://doi.org/10.1016/j.cej.2015.02.057

Romero-Güiza, M.S., Tait, S., Astals, S., del Valle-Zermeño, R., Martínez, M., Mata-Alvarez, J., Chimenos, J.M., 2015b. Reagent use efficiency with removal of nitrogen from pig slurry via struvite: A study on magnesium oxide and related by-products. Water Res. 84, 286–294. https://doi.org/10.1016/j.watres.2015.07.043

Ronteltap, M., Maurer, M., Hausherr, R., Gujer, W., 2010. Struvite precipitation from urine - Influencing factors on particle size. Water Res. 44, 2038–2046. https://doi.org/10.1016/j.watres.2009.12.015

Rosen, C., Vrecko, D., Gernaey, K. V., Pons, M.N., Jeppsson, U., 2006. Implementing ADM1 for plant-wide benchmark simulations in Matlab/Simulink. Water Sci. Technol. 54, 11–19. https://doi.org/10.2166/wst.2006.521

Ruan, S., Shi, L., Li, J., Gerson, A.R., 2016. Mechanism and kinetics of gibbsite-seeded sodium aluminosilicate crystallisation from synthetic spent Bayer liquor. Hydrometallurgy 163, 1–8. https://doi.org/10.1016/j.hydromet.2016.03.001

Samad, N.A.F.A., Singh, R., Sin, G., Gernaey, K. V., Gani, R., 2011. A generic multi-dimensional model-based system for batch cooling crystallization processes. Comput. Chem. Eng. 35, 828–843. https://doi.org/10.1016/j.compchemeng.2011.01.029

Sánchez Pérez, J.A., Rodríguez Porcel, E.M., Casas López, J.L., Fernández Sevilla, J.M., Chisti, Y., 2006. Shear rate in stirred tank and bubble column bioreactors. Chem. Eng. J. 124, 1–5. https://doi.org/10.1016/j.cej.2006.07.002

Sastry, K.V.S., Fuerstenau, D.W., 1970. Size Distribution of Agglomerates in Coalescing Dispersed Phase Systems. Ind. Eng. Chem. Fundam. 9, 145–149. https://doi.org/10.1021/i160033a023

Scarlett, B., 2002. Particle Populations - To balance or not to balance, that is the question! Powder Technol. 125, 1–4. https://doi.org/10.1016/S0032-5910(01)00488-0

Shaddel, S., Ucar, S., Andreassen, J.P., Sterhus, S.W., 2019. Engineering of struvite crystals by regulating supersaturation - Correlation with phosphorus recovery, crystal morphology and process efficiency. J. Environ. Chem. Eng. 7, 102918. https://doi.org/10.1016/j.jece.2019.102918

Shih, Y.J., Abarca, R.R.M., de Luna, M.D.G., Huang, Y.H., Lu, M.C., 2017. Recovery of phosphorus from synthetic wastewaters by struvite crystallization in a fluidized-bed reactor: Effects of pH, phosphate concentration and coexisting ions. Chemosphere 173, 466–473. https://doi.org/10.1016/j.chemosphere.2017.01.088

Soetaert, K., Petzoldt, T., 2010. Inverse Modelling, Sensitivity and Monte Carlo Analysis in *R* Using Package **FME**. J. Stat. Softw. 33. https://doi.org/10.18637/jss.v033.i03

Solon, K., Flores-Alsina, X., Kazadi Mbamba, C., Ikumi, D., Volcke, E.I.P., Vaneeckhaute, C., Ekama, G., Vanrolleghem, P.A., Batstone, D.J., Gernaey, K. V., Jeppsson, U., 2017. Plant-wide modelling of phosphorus transformations in wastewater treatment systems: Impacts of control and operational strategies. Water Res. 113, 97–110. https://doi.org/10.1016/j.watres.2017.02.007

Solon, K., Flores-Alsina, X., Mbamba, C.K., Volcke, E.I.P., Tait, S., Batstone, D., Gernaey, K. V., Jeppsson, U., 2015. Effects of ionic strength and ion pairing on (plant-wide) modelling of anaerobic digestion. Water Res. 70, 235–245. https://doi.org/10.1016/j.watres.2014.11.035

Steendam, R.R.E., Keshavarz, L., Blijlevens, M.A.R., De Souza, B., Croker, D.M., Frawley, P.J., 2018. Effects of Scale-Up on the Mechanism and Kinetics of Crystal Nucleation. Cryst. Growth Des. 18, 5547–5555. https://doi.org/10.1021/acs.cgd.8b00857

Stolzenburg, P., Capdevielle, A., Teychené, S., Biscans, B., 2014. Struvite precipitation with MgO as a precursor: Application to wastewater treatment. Chem. Eng. Sci. 133, 9–15. https://doi.org/10.1016/j.ces.2015.03.008

Sverdrup, H.U., Ragnarsdottir, K.V., 2011. Challenging the planetary boundaries II: Assessing the sustainable global population and phosphate supply, using a systems dynamics assessment model. Appl. Geochemistry 26, S307–S310. https://doi.org/10.1016/j.apgeochem.2011.03.089

Tarragó, E., Puig, S., Ruscalleda, M., Balaguer, M.D., Colprim, J., 2016. Controlling struvite particles' size using the up-flow velocity. Chem. Eng. J. 302, 819–827. https://doi.org/10.1016/j.cej.2016.06.036

The Ellen MacArthur Foundation, 2020. The Ellen MacArthur Foundation [WWW Document]. URL https://www.ellenmacarthurfoundation.org/ (accessed 10.12.20).

Torbacke, M., Rasmuson, Å.C., 2004. Mesomixing in semi-batch reaction crystallization and influence of reactor size. AIChE J. 50, 3107–3119. https://doi.org/10.1002/aic.10213

Torbacke, M., Rasmuson, Å.C., 2001. Influence of different scales of mixing in reaction crystallization. Chem. Eng. Sci. 56, 2459–2473. https://doi.org/10.1016/S0009-2509(00)00452-8

Tribout, C., Monasse, B., Haudin, J.M., 1996. Experimental study of shear-induced crystallization of an impact polypropylene copolymer. Colloid Polym. Sci. 274, 197–208. https://doi.org/10.1007/BF00665636

Triger, A., Pic, J.S., Cabassud, C., 2012. Determination of struvite crystallization mechanisms in urine using turbidity measurement. Water Res. 46, 6084–6094. https://doi.org/10.1016/j.watres.2012.08.030

van Dijk, K.C., Lesschen, J.P., Oenema, O., 2016. Phosphorus flows and balances of the European Union Member States. Sci. Total Environ. 542, 1078–1093.

https://doi.org/10.1016/j.scitotenv.2015.08.048

van Griensven, a., Meixner, T., Grunwald, S., Bishop, T., Diluzio, M., Srinivasan, R., 2006. A global sensitivity analysis tool for the parameters of multi-variable catchment models. J. Hydrol. 324, 10–23. https://doi.org/10.1016/j.jhydrol.2005.09.008

Vaneeckhaute, C., Claeys, F.H.A., Tack, F.M.G., Meers, E., Belia, E., Vanrolleghem, P.A., 2018. Development, implementation, and validation of a generic nutrient recovery model (NRM) library. Environ. Model. Softw. 99, 170–209. https://doi.org/10.1016/j.envsoft.2017.09.002

Verkoeijen, D., A. Pouw, G., M. H. Meesters, G., Scarlett, B., 2002. Population balances for particulate processes - A volume approach. Chem. Eng. Sci. 57, 2287–2303. https://doi.org/10.1016/S0009-2509(02)00118-5

Vrugt, J. a., Gupta, H. V., Bouten, W., Sorooshian, S., 2003. A Shuffled Complex Evolution Metropolis algorithm for optimization and uncertainty assessment of hydrologic model parameters. Water Resour. Res. 39, 1201. https://doi.org/10.1029/2002WR001642

Vrugt, J., Bouten, W., 2002. Validity of First-Order Approximations to Describe Parameter Uncertainty in Soil Hydrologic Models. Soil Sci. Soc. Am. J. 66, 1740–1751. https://doi.org/10.2136/sssaj2002.1740

Wilsenach, J.A., Schuurbiers, C.A.H., van Loosdrecht, M.C.M., 2007. Phosphate and potassium recovery from source separated urine through struvite precipitation. Water Res. 41, 458–466. https://doi.org/10.1016/j.watres.2006.10.014

Wodołażski, A., 2017. CFD-population balance modelling of catalyst particles in solid-liquid Rushton turbine-agitated tank reactor in scale-up study. Powder Technol. 313, 312–322. https://doi.org/10.1016/j.powtec.2017.03.032

Wójcik, J., Jones, A.G., 1997. Experimental Investigation into Dynamics and Stability of Continuous MSMPR Agglomerative Precipitation of CaCO3 Crystals. Trans IChemE 75, 113–118.

Wolkowicz, M.D., 1978. Nucleation and crystal growth in sheared poly(1-butene) melts. J. Polym. Sci. Polym. Symp. 63, 365–382. https://doi.org/10.1002/polc.5070630129

Ye, X., Gao, Y., Cheng, J., Chu, D., Ye, Z.-L., Chen, S., 2018. Numerical simulation of struvite crystallization in fluidized bed reactor. Chem. Eng. Sci. 176, 242–253. https://doi.org/10.1016/j.ces.2017.10.048

Ye, X., Ye, Z.L., Lou, Y., Pan, S., Wang, X., Wang, M.K., Chen, S., 2016. A comprehensive understanding of saturation index and upflow velocity in a pilot-scale fluidized bed reactor for struvite recovery from swine wastewater. Powder Technol. 295, 16–26. https://doi.org/10.1016/j.powtec.2016.03.022

Yetilmezsoy, K., Ilhan, F., Kocak, E., Akbin, H.M., 2017. Feasibility of struvite recovery process for fertilizer industry: A study of financial and economic analysis. J. Clean. Prod. 152, 88–102. https://doi.org/10.1016/j.jclepro.2017.03.106

Zauner, R., Jones, A.G., 2000a. Determination of nucleation, growth, agglomeration and disruption kinetics from experimental precipitation data: The calcium oxalate system. Chem. Eng. Sci. 55, 4219–4232. https://doi.org/10.1016/S0009-2509(00)00059-2

Zauner, R., Jones, A.G., 2000b. Mixing effects on product particle characteristics from semi-batch crystal precipitation. Trans IChemE 78, 894–902. https://doi.org/10.1205/026387600527969

Zhang, C., Xu, K., Zheng, M., Li, J., Wang, C., 2018. Factors Affecting the Crystal Size of Struvite-K Formed in Synthetic Urine Using a Stirred Reactor. Ind. Eng. Chem. Res. 57, 17301–17309. https://doi.org/10.1021/acs.iecr.8b03328

APPENDIX A

TABLEAU METHOD

The Tableau method is used to represent chemical equilibrium relationships. In this method mass balances and equilibrium relationships are systematically represented using a matrix structure, as explained in Lizarralde (2015).

The chemical system is represented using a set of components and a set of species. Species are every chemical entities to be considered. Each species can be written as the product of a reaction only involving components, while components cannot be written as the product of a reaction involving other components.

The cells in the matrix are written in order to express the species present in the system as lineal combinations of the components. The definition of mass balances is done as the sum of all species written as lineal combination of the component in each column. The equilibrium relationships are defined as products in each line of the matrix.

The Tableau method will be applied to a simple example with the next four acid-base chemical reactors.

- $H_2O \leftrightarrow H^+ + OH^-$
- $NH_4^+ \leftrightarrow H^+ + NH_3$
- $H_2PO_4^- \leftrightarrow H^+ + HPO_4^=$

- $HPO_4^{=} \leftrightarrow H^+ + PO_4^{3-}$

The first step of the Tableau method is the definition of the components and species from the chemical system. This is done in Table A.1.

Table A.1: Components and species from the example

Components	Species	
H_2O	H_2O	OH^-
H^+	H^+	NH_3
NH_4^+	NH_4^+	HPO_4^{2-}
$H_2PO_4^-$	$H_2PO_4^-$	PO_4^{3-}

The second step of the Tableau method is the construction of the Tableau matrix (see Table A.2).

Table A.2: Tableau Matrix.

Species	Components				
	H_2O	H^+	NH_4^+	$H_2PO_4^-$	Log K
H_2O	1				
H^+		1			
NH_4^+			1		
$H_2PO_4^-$				1	
OH^-	1	-1			-13.997
NH_3		-1	1		9.244
HPO_4^{2-}		-1		1	7.198
PO_4^{3-}		-2		1	19.573

The third step of the Tableau method is to define the mass action law for each defined species. This is done in Table A.3.

Table A.3: Mass action equation for each species.

Species	
H_2O	$[H_2O] = [H_2O]$
H^+	$[H^+] = [H^+]$
NH_4^+	$[NH_4^+] = [NH_4^+]$
$H_2PO_4^-$	$[H_2PO_4^-] = [H_2PO_4^-]$
OH^-	$[OH^-] = [H_2O] \cdot [H^+]^{-1} \cdot 10^{-13.997}$
NH_3	$[NH_3] = [NH_4^+] \cdot [H^+]^{-1} \cdot 10^{9.244}$
HPO_4^{2-}	$[HPO_4^{2-}] = [H_2PO_4^-] \cdot [H^+]^{-1} \cdot 10^{7.198}$
PO_4^{3-}	$[PO_4^{3-}] = [H_2PO_4^-] \cdot [H^+]^{-2} \cdot 10^{19.573}$

The fourth step is to write the mass balance equations for each component:

$$Y_j = \sum_i a_{ij} \cdot C_i - T_j$$

where, Y_j is the difference between the calculated total dissolved concentration of the j^{th} component and the known analytical total dissolved concentration of component j, a_{ij} is the stoichiometric coefficient of component j in species i, C_i is the concentration of the i^{th} species and T_j is the concentration of the j^{th} component.

Table A.4: Mass balance equation for each component.

Components	
H_2O	Mass balance is neglected on H2O because it is presumed to be present in constant activity
H^+	$Y_{H^+} = (C_{H^+} - C_{OH^-} - C_{NH_3} - C_{HPO_4^-} - C_{PO_4^{2-}}) - T_{H^+}$
NH_4^+	$Y_{NH_4^+} = C_{NH_4^+} + C_{NH_3} - T_{NH_4^+}$
$H_2PO_4^-$	$Y_{H_2PO_4^-} = C_{H_2PO_4^-} + C_{PO_4^{2-}} + C_{PO_4^{3-}} - T_{H_2PO_4^-}$

From the combination of the equilibrium relationships (Table A.3) and mass balance equations (Table A.4) a set of three equations with three unknown values needs to be solved. The mathematical solution reached will give the value of 0 to Y_{H^+}, $Y_{NH_4^+}$ and $Y_{H_2PO_4^-}$ or, more practically a value smaller than some acceptable convergence error.

APPENDIX B

SUPPLEMENTARY EXPERIMENTAL DATA

This appendix includes the supplementary data obtained in the experiments performed for the completion of Chapter 4.

B.1. SUPPLEMENTARY DATA FOR EXPERIMENT A

In Figures B.1-B.12 the average pH evolution, the average + standard deviation (stdev) pH evolution and the average – stdev pH evolution of the runs of Blocks A1 and A2 from Experiment A are shown.

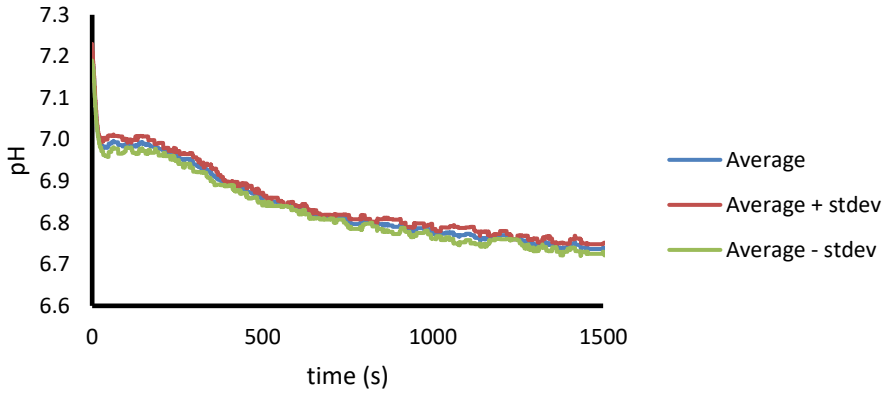

Figure B.1: Average pH evolution, Average + stdev pH evolution and Average – stdev pH evolution for A1-300 rpm

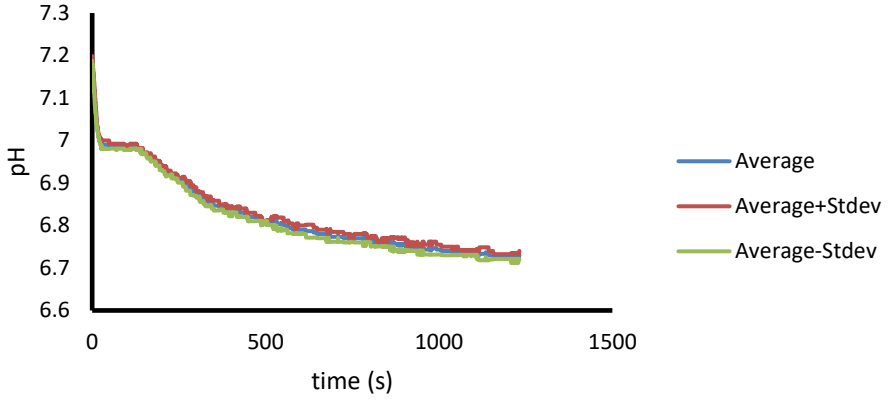

Figure B.2: Average pH evolution, Average + stdev pH evolution and Average – stdev pH evolution for A1-400 rpm

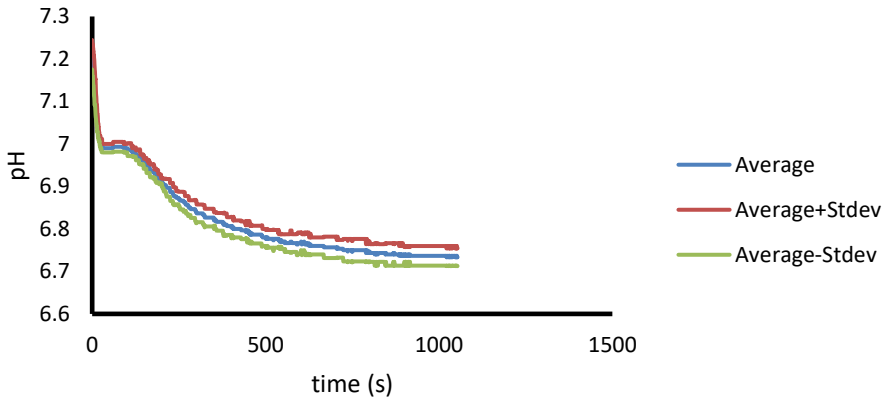

Figure B.3: Average pH evolution, Average + stdev pH evolution and Average – stdev pH evolution for A1-500 rpm

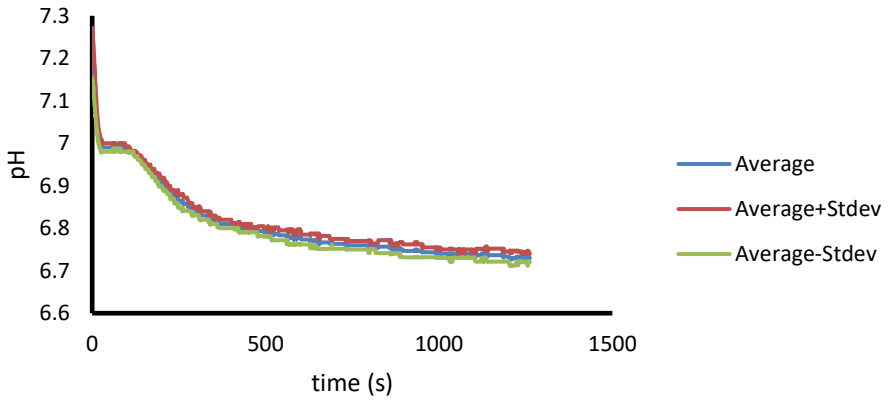

Figure B.4: Average pH evolution, Average + stdev pH evolution and Average – stdev pH evolution for A1-600 rpm

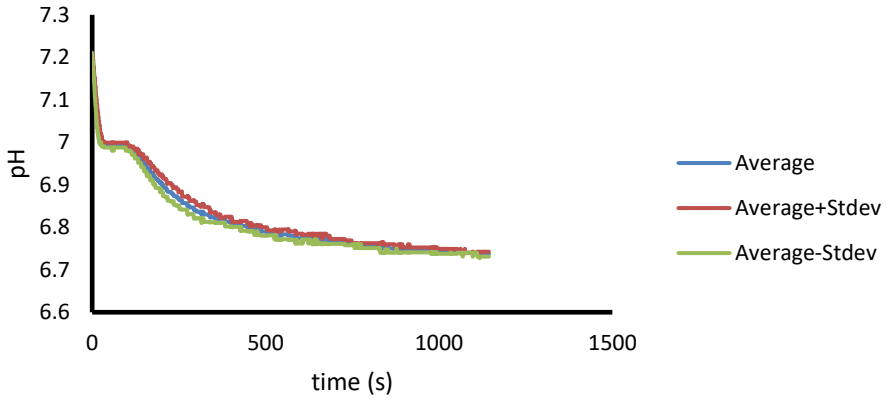

Figure B.5: Average pH evolution, Average + stdev pH evolution and Average – stdev pH evolution for A1-700 rpm

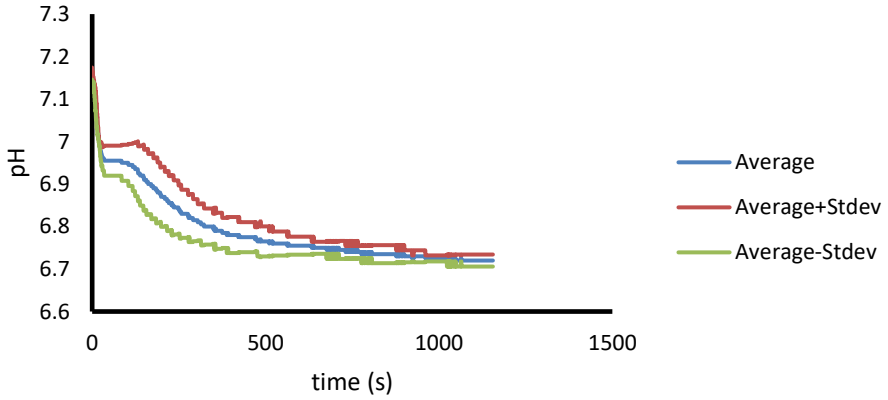

Figure B.6: Average pH evolution, Average + stdev pH evolution and Average – stdev pH evolution for A1-800 rpm

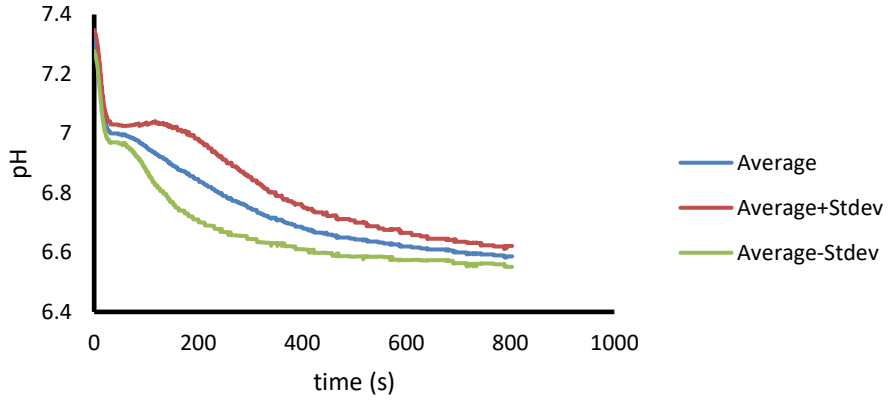

Figure B.7: Average pH evolution, Average + stdev pH evolution and Average – stdev pH evolution for A2-300 rpm

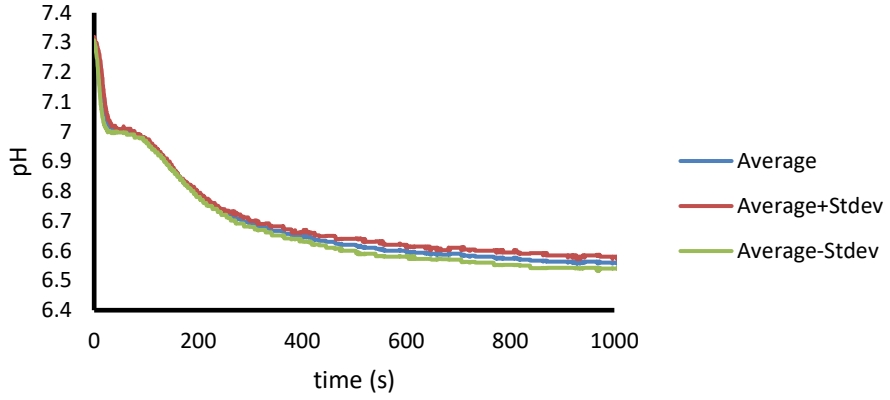

Figure B.8: Average pH evolution, Average + stdev pH evolution and Average – stdev pH evolution for A2-400 rpm

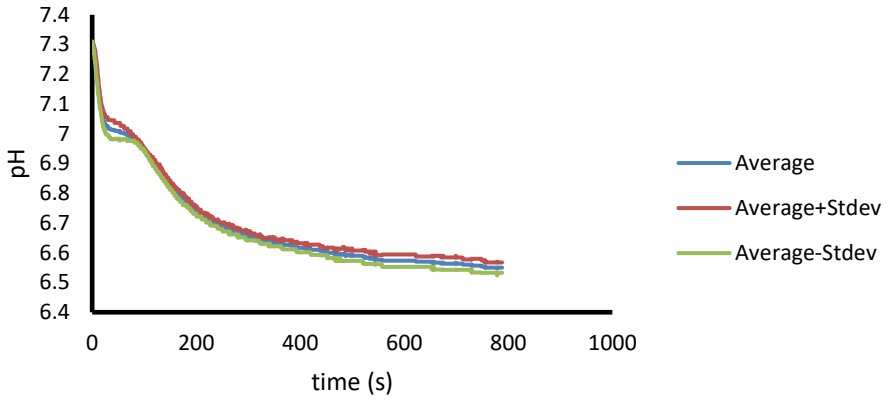

Figure B.9: Average pH evolution, Average + stdev pH evolution and Average – stdev pH evolution for A2-500 rpm

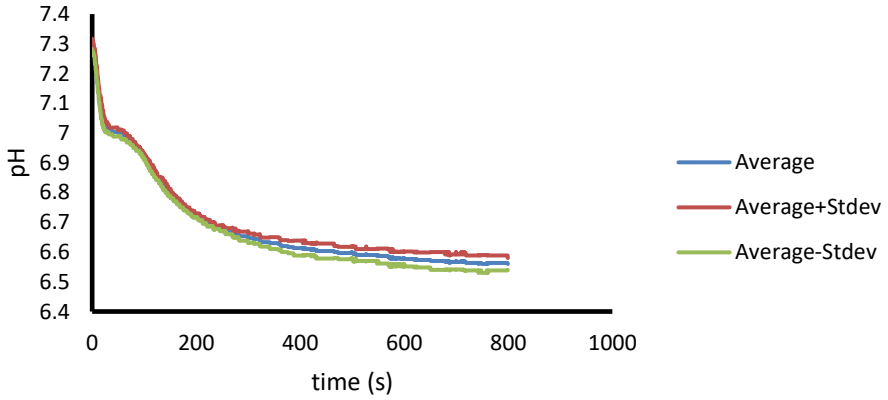

Figure B.10: Average pH evolution, Average + stdev pH evolution and Average – stdev pH evolution for A2-600 rpm

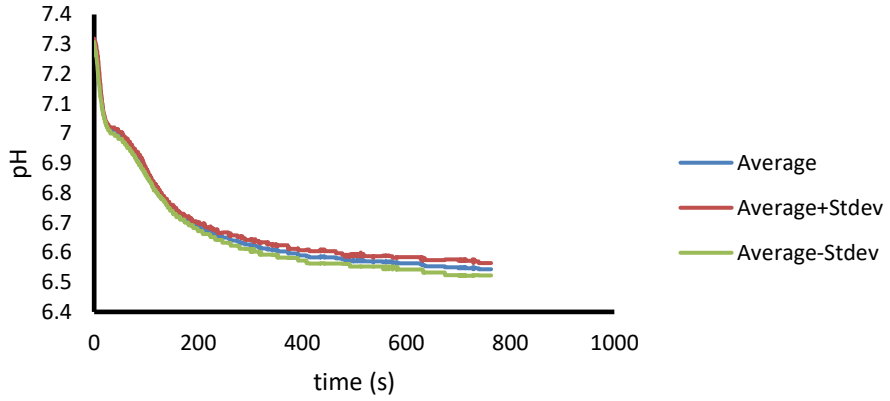

Figure B.11: Average pH evolution, Average + stdev pH evolution and Average – stdev pH evolution for A2-700 rpm

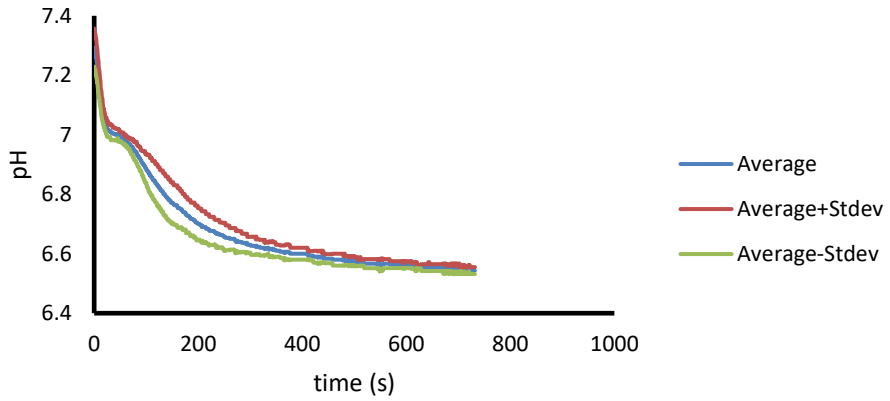

Figure B.12: Average pH evolution, Average + stdev pH evolution and Average – stdev pH evolution for A2-800 rpm

B.2. SUPPLEMENTARY DATA FOR EXPERIMENT B – PSD QUALITY ANALYSIS

In order to relate the change in the PSD with the effect of local mixing and the SI and not to another possible physico-chemical effect, a number of preliminary issues were considered for the PSD measurements in Experiment B:

1. Repeatability of the measurements.
2. Particle settling at the bottom of the reactor.
3. Homogeneity of the particle distribution within the reactor.
4. Particle behavior under SI = 0 condition.

Experimental runs performed for this analysis are included in Table 4.1 (in Chapter 4) as Block MQ (Measurements Quality) and the results are given here.

B.2.1. Repeatability of the measurements

An experiment was executed three times to determine the repeatability of the measurements in Experiment B (runs 1-3). For these experiments, the space between the bottom of the reactor and the stirrer was 2.5 cm and the stirrer speed 90 rpm. Molar ratio was 1:1.5:2 in P:Mg:N and initial pH 8.00. Initial concentration of P was 0.03 M. Tracked variables were the pH evolution and PSD at two different times of the experiment (1 minute and 20 minutes).

Table B.1: PSD repeatability for runs 1-3

	Repeatability test run 1-3									
	Run 1		Run 2		Run 3		1 min		20 min	
	1 min	20 min	1 min	20 min	1 min	20 min	Avg 1	Stdev 1	Avg 20	Stdev 20
D10 (μm)	33.50	56.31	32.82	58.49	32.97	72.84	33.10	0.29	62.55	7.33
D50 (μm)	45.70	111.15	44.59	108.20	45.27	117.90	45.19	0.46	112.42	4.06
D90 (μm)	63.58	149.86	64.64	147.02	57.52	158.90	61.91	3.14	151.93	5.07

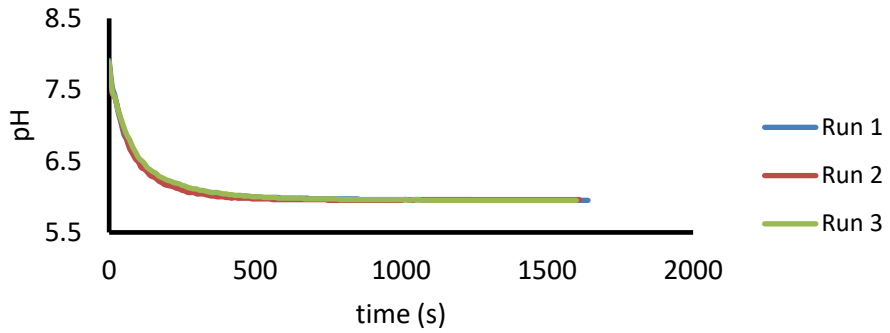

Figure B.13: pH evolution for runs 1-3 in MQ block

B.2.2. Particle settling at the bottom of the reactor

The stirrer speeds were selected in order to:

1. Maintain suspension of precipitant solids.
2. Avoid vortex formation.

Accordingly, stirrer speeds between 200 and 400 rpm were chosen.

The minimum speed to prevent settling, N_{js} (rpm), was chosen based on the Zwietering's equation (eq B.1):

$$N_{js} = S\left(\frac{g(\rho_s - \rho_L)}{\rho_L}\right)^{0.45} \frac{X^{0.13} d_p{}^{0.2} \nu^{0.1}}{D^{0.85}} \qquad \textbf{B.1}$$

Where S (-) is a constant, g is the gravitational constant (m/s^2), ρ_s is the solid density (kg/m^3), X is the solids loading mass (100·mass of solid/mass of liquid), $d_p$is particle diameter (m) and ν is the kinematic viscosity (m^2/s). Runs 4-6 were used to measure particle concentration in the system under stirrer speeds lower than 200 rpm and experimentally observe possible settling effects in the system.

Particle settling could also have occurred in the measuring vessel of the Multisizer 4 Coulter Counter. To avoid potential settling, batch experiments were carried out in close proximity to the measuring device. In addition, the suspension formed by the

sample and the electrolyte solution was stirred for 15 seconds in the Multisizer 4 Coulter Counter before measurements were taken.

Table B.2: Results for the Zwietering's equation used for the particle settling analysis.

	N_{js} (rpm)		
Mass (g)	dp = 100 (µm)	dp = 300 (µm)	dp = 600 (µm)
1	83	104	119
2.5	94	117	134
10	112	140	161

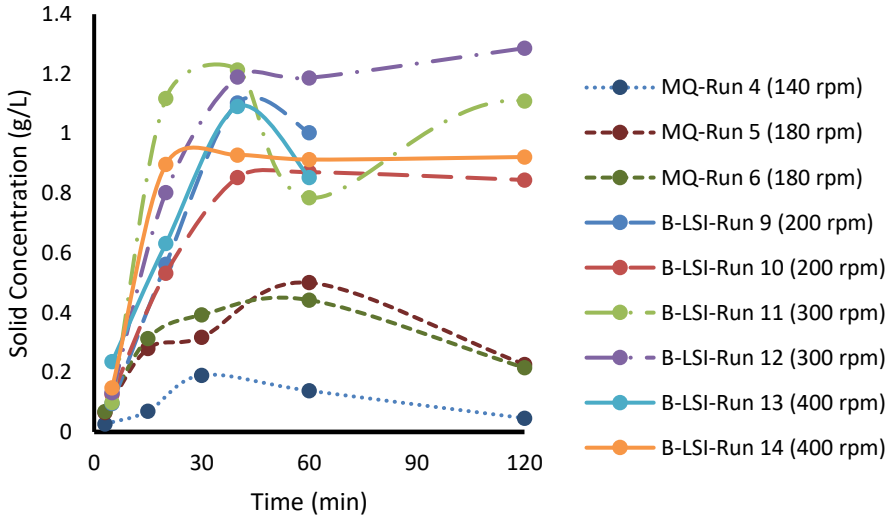

Figure B.14: Solid concentration measurement for different the same concentration of reactants and different stirrer speeds in experimental runs in MQ and B-LSI block.

B.2.3. Homogeneity in the reactor

For runs 9, 11 and 13 on the LSI Block (see Table 1), measurements were taken at 3 different depths in the reactor at the conclusion of the precipitation. Measurements

were done to ensure that the PSD and particle concentration were therefore uniform in the reactor. Samples were taken after equilibrium was achieved, after the precipitation took place in the reactor and added to a Schott Bottle previously filled with 100 ml of struvite-saturated electrolyte before measuring.

Table B.3: Homogeneity in the Reactor in PSD and particle number.

Run and Stirrer Speed (rpm)	Sampling Point	d10 (µm)	d50 (µm)	d90 (µm)	Particle Count
Run 9 (200 rpm)	Upper	42.81	76.98	157.22	939
	Lower	40.03	78.47	158.52	1109
	Middle	40.85	71.65	152.41	1116
	Average	41.23	75.7	156.05	1054
	Stdev	2.84	4.35	3.68	105
Run 11 (300 rpm)	Upper	42.31	72.78	124.32	1839
	Lower	41.25	77.51	135.64	1492
	Middle	40.43	71.9	128.76	2382
	Average	41.33	74.06	129.57	1808
	Stdev	1.82	4.25	8.02	582
Run 13 (400 rpm)	Upper	37.71	63.09	108.56	2236
	Lower	38.16	65.59	108.72	2704
	Middle	40.02	67.85	112.45	2077
	Average	38.63	65.51	109.91	2339
	Stdev	1.12	2.18	3.08	419

B.2.4. Particle behaviour under SI = 0 condition

Possible changes in the PSD in the equilibrium (as indicated by the solution pH) were also considered. Aggregation and/or breakage could change the PSD once SI was zero (i.e. equilibrium), decoupling PSD evolution from the SI variation, measured as a pH change.

To ensure that all the changes in the PSD were related only to changes in the evolution of the SI in the reactor, 2 experiments were performed (runs 7-8 in Block MQ). Both experiments had a SI=0, which was obtained by letting 750 ml of a seeded dissolution of 0.012 M P and 1:1.5:2 in P:Mg:N react until a stable pH was obtained. The quantities of seed added and the rpm in the experiments were 2 g and 300 rpm

for run 7, and 15.18 g and 250 rpm for run 8. PSD was periodically measured in these experiments.

Table B.4: PSD monitoring in saturated solution to evaluate the impact of agglomeration and/or breakage.

	time	d10 (µm)	d50 (µm)	d90 (µm)
Run 7	20 min	42.21	91.65	145
	45 min	41.6	88.25	143.8
	2h	45.44	94.07	144.72
	5 h	42.75	91.31	144.88
	Avg	43	91.32	144.6
	Stdev	1.46	2.07	0.47
Run 8	3 min	51.9	110.1	158.85
	15 min	53.22	118.9	174.1
	30 min	48.49	110	170.28
	60 min	52.18	114.8	165.7
	120 min	52.52	113.75	165.4
	240 min	51.44	111.2	164
	Avg	51.63	113.13	166.39
	Stdev	1.5	3.14	4.81

APPENDIX C

SUPPLEMENTARY DATA FOR CHAPTER 5

In this appendix, extra information of the simulations performed in the Chapter 5 and the results obtained is included. Table C.1 includes the minimum and maximum values of the Kr Nucleation and Kr Growth in each of the 1000-simulation group. Table C.2 includes the best values of the Kr Nucleation and Kr Growth for each group and shear rate, the M value obtained for each parameter pair and the Total M for each 1000-simulation group.

Table C.1: Selected parameter ranges for Kr Nucleation and Kr Growth

Simulation	Growth Exponent	Area Exponent	Nucleation Exponent	Kr Nucleation		Kr Growth	
				Min	Max	Min	Max
1	2	1.6	10	$1 \cdot 10^6$	$5 \cdot 10^8$	1	15
2	2	1.6	11	$1 \cdot 10^6$	$5 \cdot 10^8$	1	15
3	2	1.6	12	$1 \cdot 10^6$	$5 \cdot 10^8$	1	15
4	1.8	1.6	10	$1 \cdot 10^6$	$5 \cdot 10^8$	1	15
5	1.8	1.6	11	$1 \cdot 10^6$	$5 \cdot 10^8$	1	15
6	1.8	1.6	12	$1 \cdot 10^6$	$5 \cdot 10^8$	1	15
7	1.8	1.8	10	$1 \cdot 10^6$	$5 \cdot 10^8$	1	15
8	1.8	1.8	11	$1 \cdot 10^6$	$5 \cdot 10^8$	1	15
9	1.8	1.8	12	$1 \cdot 10^6$	$5 \cdot 10^8$	1	15
10	2	1.8	10	$1 \cdot 10^6$	$5 \cdot 10^8$	1	15
11	2	1.8	11	$1 \cdot 10^6$	$5 \cdot 10^8$	1	15
12	2	1.8	12	$1 \cdot 10^6$	$5 \cdot 10^8$	1	15
13	2	2	10	$1 \cdot 10^6$	$5 \cdot 10^8$	1	15
14	2	2	11	$1 \cdot 10^6$	$5 \cdot 10^8$	1	15
15	2	2	12	$1 \cdot 10^6$	$5 \cdot 10^8$	1	15
16	2	1.8	13	$5 \cdot 10^5$	$9 \cdot 10^7$	0.5	5
17	2	1.8	14	$5 \cdot 10^5$	$9 \cdot 10^7$	0.5	5
18	2	1.8	15	$5 \cdot 10^5$	$9 \cdot 10^7$	0.5	5
19	1.9	1.8	13	$5 \cdot 10^5$	$9 \cdot 10^7$	0.5	5
20	2.1	1.8	13	$5 \cdot 10^5$	$9 \cdot 10^7$	0.5	5
21	2.2	1.8	13	$5 \cdot 10^5$	$9 \cdot 10^7$	0.5	5

Table C.2: Best values of Kr Nucleation (K_B) and Kr Growth (K_G) for each exponent group and the associated M values and Total M.

				200 rpm			300 rpm			400 rpm			
Sim	n_G	α	n_B	K_B	K_G	M	K_B	K_G	M	K_B	K_G	M	Total M
1	2	1.6	10	1.35E+08	3.83	53.60	2.35E+08	4.25	34.39	4.10E+08	4.72	19.22	107.22
2	2	1.6	11	4.74E+07	3.80	47.31	9.44E+07	4.36	31.96	1.59E+08	4.66	18.56	97.83
3	2	1.6	12	2.35E+07	4.11	43.20	3.76E+07	4.35	30.47	7.51E+07	4.70	19.64	93.30
4	1.8	1.6	10	1.18E+08	4.57	54.73	2.37E+08	5.24	36.41	3.74E+08	5.62	20.20	111.34
5	1.8	1.6	11	4.40E+07	4.33	48.80	9.58E+07	4.96	33.97	1.53E+08	5.59	19.80	102.57
6	1.8	1.6	12	2.02E+07	4.69	43.66	3.33E+07	4.31	34.38	5.93E+07	5.53	20.44	98.48
7	1.8	1.8	10	1.22E+08	2.33	53.34	2.30E+08	2.53	34.12	3.78E+08	2.86	18.90	106.35
8	1.8	1.8	11	5.62E+07	2.32	47.41	8.11E+07	2.31	32.21	1.68E+08	2.85	18.50	98.13
9	1.8	1.8	12	2.40E+07	2.32	42.43	3.79E+07	2.62	29.83	7.37E+07	2.97	19.46	91.72
10	2	1.8	10	1.19E+08	1.96	53.07	2.30E+08	2.15	33.05	3.80E+08	2.51	18.48	104.59
11	2	1.8	11	5.85E+07	2.16	47.61	1.03E+08	2.13	30.56	1.59E+08	2.52	17.65	95.81
12	2	1.8	12	2.27E+07	1.86	41.44	3.52E+07	2.12	28.45	6.56E+07	2.42	17.82	87.72
13	2	2	10	1.30E+08	1.05	54.21	2.45E+08	1.19	33.20	4.05E+08	1.28	18.67	106.08
14	2	2	11	4.22E+07	1.22	51.98	1.27E+08	1.13	32.15	1.72E+08	1.27	17.71	101.84
15	2	2	12	2.01E+07	1.11	42.08	4.29E+07	1.13	28.08	7.20E+07	1.28	17.85	88.02
16	2	1.8	13	7.17E+06	1.87	36.40	1.49E+07	2.16	27.55	2.80E+07	2.51	19.22	83.17
17	2	1.8	14	3.39E+06	2.03	32.68	7.10E+06	2.33	28.77	1.06E+07	2.57	21.85	83.29
18	2	1.8	15	1.39E+06	2.16	31.41	2.59E+06	2.33	29.65	4.32E+06	2.58	25.24	86.31
19	1.9	1.8	13	7.41E+06	2.13	36.09	1.42E+07	2.35	28.14	2.53E+07	2.60	19.69	83.92
20	2.1	1.8	13	7.84E+06	1.68	36.64	1.46E+07	1.98	27.25	2.80E+07	2.37	18.93	82.81
21	2.2	1.8	13	8.19E+06	1.73	36.81	1.67E+07	1.80	27.27	2.93E+07	2.21	18.72	82.80

APPENDIX D

PROJECTS GENERATED FROM THE THESIS

The topic of the thesis has been (Birziphos) and is going to be (Magnyfos) further developed in two projects funded by regional and national authorities.

- **Magnyfos- Utilización de subproductos de magnesio para la recuperación del fósforo en estaciones depuradoras de aguas residuales mediante precipitación de estruvita**

  The project aims to design, develop and validate in a real environment a technological solution that will allow to recover P from urban wastewater. This will be made by using industrial by-products with a high concentration in MgO as a Mg source in the process. The research will be done by combining experimental work at laboratory, pilot and real scale with mathematical simulation tools as the PWM, PBM and/or CFD.

  - Funding Organism: Proyectos de I+D+i «Retos-Colaboración» del Programa Estatal de Investigación, Desarrollo e Innovación Orientada a los Retos de la Sociedad, en el marco del Plan Estatal de Investigación Científica y Técnica y de Innovación 2017-2020

- Partners: Magnesitas Navarras S.L., NILSA, Universidad de Barcelona, Ceit
- Period: 01/07/2020-31/12/2023

- **Birziphos - Recuperación de Fósforo a partir de Residuos Sólidos Urbanos: Avanzando hacia una Economía Circular**

  The project aimed to experimentally validate a technological solution to recover P salts from anaerobic digestion leachate and to develop the use of modelling techniques to represent precipitation processes. Experimental work carried out in a fluidised bed reactor showed the feasibility of the process. Multiphase simulations in CFD were used as a support tool in the operation of the fluidised bed reactor.

  - Funding Organism: Diputación Foral de Gipuzkoa, Subvenciones para actuaciones en materia de prevención, reutilización y reciclaje de residuos domésticos. Economía circular (2018-PREV-000028-01)
  - Partners: Tecnun, Ceit
  - Period: 01/01/2018-31/10/2018

APPENDIX E

PUBLICATIONS GENERATED FROM THE THESIS

The scientific publications derived from the present thesis are listed below:

INTERNATIONAL JOURNALS

Published papers

1. Elduayen-Echave B., Lizarralde I., Larraona G. S., Ayesa E., Grau P., 2019. A new mass-based discretized Population Balance Model for precipitation processes: application to struvite precipitation. Water Research, 155, 26-41.
2. B. Elduayen-Echave, M. Azcona, P. Grau, P.A. Schneider, Effect of the shear rate and supersaturation on the nucleation and growth of struvite in batch stirred tank reactors, J. Water Process Eng. 38 (2020) 10. doi:10.1016/j.jwpe.2020.101657.

Submitted papers

1. Chapter 5 has been re-drafted from an article submitted to Water Research.

BOOK CHAPTERS

1. B. Elduayen-Echave, A. Ochoa de Eribe, I. Lizarralde, G. Sánchez, P. Grau, Frontiers in Wastewater Treatment and Modelling, 1st ed., Springer International Publishing, Cham, 2017. doi:10.1007/978-3-319-58421-8. ISBN: 978-3-319-58420-1.

INTERNATIONAL CONFERENCE PROCEEDINGS

Elduayen-Echave, B, Lizarralde, I., Schneider, P.A., Larraona, G. S. and Grau, P.
Title: **Calibration of a Population Balance Model including the Shear Rate as a variable in the Kinetics of the Process**
Conference: 10th IWA Symposium on System Analysis and Integrated Assessment, Watermatex 2019
Date: 1-4 September, Copenhagen (Denmark)

Lizarralde, I., Elduayen-Echave B., Larraona, G.S. and Grau, P.
Title: **Advanced Modelling Tools for the Description of Struvite Recovery Technologies**
Conference: The 16th IWA Leading Edge Conference on Water and Wastewater Technologies
Date: 10-14 June 2019, Edinburgh (United Kingdom)

Elduayen-Echave, B., Lizarralde, I., Schenider, P.A., Sánchez-Larraona, G. and Grau P.
Title: **Advanced modelling tools for the description of struvite recovery in WRRF**
Conference: WRRmod 2018.
Date: 10-14 March 2018, Lac Beauport, Quebec (Canada)

Elduayen-Echave, B., Ochoa de Eribe, A., Lizarralde, I., Sánchez-Larraona, G., Ayesa, E. and Grau P.

Title: **Sensitivity Analysis and Calibration with Bayesian Inference of a Mass-based Discretized Population Balance Model for Struvite Precipitation**

Conference: Frontiers International Conference on Wastewater Treatment, FICWTM2017 Date: 21-24 May 2017, Palermo (Italy) Best Paper Award in Anaerobic digestion category.